NANO-SELECTIVE-AREA GROWTH OF GROUP III-NITRIDES ON SILICON AND CONVENTIONAL SUBSTRATES

A Dissertation
Presented to
The Academic Faculty

by

Peter L Bonanno

In Partial Fulfillment
of the Requirements for the Degree
Doctor of Philosophy in the
School of Electrical and Computer Engineering

Georgia Institute of Technology
August 2016

Copyright © by P.L Bonanno 2016

NANO-SELECTIVE-AREA GROWTH OF GROUP III-NITRIDES ON SILICON AND CONVENTIONAL SUBSTRATES

Approved by:

Prof. Abdallah Ougazzaden, Advisor
School of Electrical and Computer Engineering
Georgia Institute of Technology

Dr. Shyh-Chiang Shen
School of Electrical and Computer Engineering
Georgia Institute of Technology

Dr. Jean Paul Salvestrini
Georgia Tech Lorraine

Date Approved: March 2016

ACKNOWLEDGEMENTS

I wish to thank Tatianna Mathews, Thesis Office Coordinator for updating the original template. Without her, I probably would have written the entire thing in Comic Sans. I'm also grateful to Josyane Roschitz, Katia Menard, and Nicolas Jacquet for their tireless help keeping my head above water with French administrative matters, and of course my advisor, Prof. Abdallah Ougazzaden for again and again (and again) finding the means to keep me supported. I'm also indebted to Prof. Onofrio Russo for inciting in me a passion for Physics and Prof. Andrei Sirenko for his mentorship as a researcher.

TABLE OF CONTENTS

ACKNOWLEDGEMENTS iii

LIST OF ABBREVIATIONS vi

SUMMARY vii

INTRODUCTION 1

1.1 Group III-Nitrides 2

1.2 2D Heteroepitaxy of GaN 5

1.3 Selective Area Growth 8

TOOLS AND TECHNIQUES 11

2.1 NSAG under MOVPE 12

2.2 Scanning Electron Microscopy 15

2.3 Nanocathodoluminescence 16

2.4 Atomic Force Microscopy 17

2.5 Synchrotron-Based Submicron-Beam X-Ray Diffraction 18

2.6 Transmission Electron Microscopy 26

SELECTIVE AREA GROWTH ON TRADITIONAL SUBSTRATES 29

3.1 MicroSAG 29

3.2 GaN NSAG 36

3.3 InGaN/GaN NSAG 44

3.4 AlGaN NSAG 52

3.5 Coalesced NSAG microtemplates 54

SELECTIVE AREA GROWTH ON SILICON 56

4.1 Early work on bare Silicon 56

4.2 The AlN-buffered Silicon (111) template 59

4.2.1 GaN NSAG 60

4.2.2 InGaN grown on NSAG GaN nanodots 63

4.2.3 Mask geometry study of InGaN on NSAG GaN nanodots 70

4.2.4 InGaN grown on coalesced NSAG microtemplates 74

4.2.5 NSAG BGaN 78

CONCLUSIONS AND FUTURE WORK 87

5.1 Summary of Completed Work. 87

5.2 Future Work 89

REFERENCES 101

LIST OF ABBREVIATIONS

a, c parameter	Parameters of the crystal lattice
AFM	Atomic force microscopy
CCD	Charge-coupled device
CL	Cathodoluminescence
EDX	Energy-dispersive X-ray spectroscopy
ELO	Epitaxial lateral overgrowth
FWHM	Full-width at half-maximum
HAADF	High-angle annular dark field
LED	Light emitting diode
MBE	Molecular beam epitaxy
MOVPE	Metalorganic vapor phase epitaxy
MQW	Multi-quantum well
NBE	Near band edge
NSAG	Nano-selective area growth(/grown)
SAG	Selective area growth(/grown)
SEM	Scanning electron microscopy
Si(111)	The (111) plane of silicon
STEM	Scanning transmission electron microscopy
UV	Ultraviolet
XRD	X-ray diffraction

SUMMARY

We developed and evaluated NSAG techniques for Group III-Nitrides as a way to mitigate the various difficulties with this material system (high defect density, threading dislocations, phase separation and graining, etc.), to bring these material systems to the nanoscale, and to allow the use of inexpensive silicon substrates.

To that end, we used optimized NSAG of GaN, InGaN, AlGaN, and BGaN grown on GaN/Sapphire and AlN/Si(111) templates, evaluating the effectiveness of our NSAG techniques on each template by comparing our results to those obtained from planar (non-NSAG) growth. We also investigated the engineering of microtemplates by coalescing NSAG GaN structures and comparing surface properties and subsequent epilayer growth to that of normal planarly grown GaN.

Across the board, NSAG was selective and, when compared to planar growth, consistently resulted in higher quality material with fewer dislocations. NSAG of GaN on AlN/Si(111) resulted in defect-free nanopyramids, 90% of which were single crystal. By coalescing nanostructures into a microtemplate, we produced an InGaN top layer with 7 times the optical emission intensity as InGaN grown simultaneously on non-NSAG planar GaN.

NSAG InGaN nanopyramids grown on GaN/Sapphire templates were used to make PIN-based solar cells that produced current 3 orders of magnitude greater than their planar counterparts, and which had 20 times greater IV ratios at ±1 V. We then leveraged this newly-won know-how with our previous success growing NSAG GaN on AlN/Si(111) to produce InGaN nanopyramids on AlN/Si(111) with no defect band and

50% stronger luminescence than in 2D growth. These nanopyramids were highly uniform, single-crystal, dislocation-free, and free from phase clustering effects and other nonuniformities found in planar growth. With additional effort, we achieved a maximum InN composition of 33%, with NSAG material showing four times better emission characteristics than planar material on the same substrate. Additionally, we found that mask margin affected InN composition and therefore emission wavelength of our nanopyramids, and that by using different mask geometries on the same template, we can create single-growth-step multi-color micropixels. In our most current iteration, we produced both green and red-emitting material in one growth step.

Lastly, we achieved NSAG BGaN nanopyramids on both AlN/Si(111) and GaN/Sapphire. As expected, we found unmasked field growth of BGaN to be of a much lower quality on AlN/Si(111) than on GaN, but also found that the former benefitted much more from NSAG, owing to its low BGaN nucleation rate. As with NSAG of GaN, BGaN nanopyramids on AlN/Si(111) were single crystal to the extent that nucleation occurred once per aperture, which happened in more than 90% of the apertures. On AlN/Si(111), XRD and CL showed BN composition to be between 1.3 and 2.0%, and the nanopyramids on both substrates exhibited smooth sidewalls.

CHAPTER 1

INTRODUCTION

Group III-Nitride semiconductive materials, which include GaN, InN, AlN, BN, their ternaries, and their quaterneries, have generated an intense interest due to their potential in light generation, communications, radiation detection, power generation and power storage. Controlling the ternary composition allows for a fully engineerable bandgap, allowing optical devices to operate at any frequency from 0.7 to 6.2 eV, which covers the entire visible spectrum and near ultra-violet frequencies. These materials are also more robust than traditional GaAs and Silicon-based systems, and overcome device parameter limitations such as power density, maximum frequency and breakdown voltage. Additionally, their low intrinsic carrier concentration translates to low leakage and dark currents in devices. These properties make the material system extremely useful for light generation and lasing, and well as for detection and communications applications. These applications have been proven and commercialized, but cost remains a major limitation on commercial growth. The high cost owes predominantly to the lack of native substrates. Expensive hetero-substrates are traditionally used, and there has been a great deal of work done on developing low-cost solutions that result in high-quality Nitride layers and device structures.

With the prohibitive cost of hereto low-quality bulk GaN making native substrates unfeasible, the most suitable bulk substrates for Nitride growth are Sapphire and Silicon Carbide (SiC). These materials are themselves quite expensive, and using them to obtain high-quality Nitride layers is not a straightforward task- the mismatched lattice parameters and thermal expansion coefficients tend to cause high defect density and rough surface morphology in the Nitride layer, which leads to poor transport properties and bad device quality. Still, there has been considerable success in achieving device-

quality Nitride layers on these substrates using techniques such as epitaxial lateral overgrowth (ELO) and nano-selective-area growth (NSAG), which block the propagation of threading dislocations from the heterointerface and benefit from 3D stress relief mechanisms, resulting in device-quality Nitride material.

Until now, these techniques have enjoyed success on Sapphire and SiC, which is fantastic progress. However, even these substrates are costly when compared with Silicon. Not only that, but many devices have components that are well served by current Silicon-based technology, so integrating into such a device a Nitride-based component that is largely Sapphire or SiC presents another challenge. The ideal situation would be to grow Nitrides directly on Silicon substrates. This is the focus of this work.

This introductory chapter will describe the Nitride material system, giving its applications and relevant parameters and characteristics. It will also introduce the mechanisms, challenges and progress of Nitride heteroepitaxy by metalorganic vapor phase epitaxy (MOVPE) and finally the technologies of selective area growth and ELO.

Chapter 2 will cover the tools and techniques used in this work. Chapter 3 will cover preliminary NSAG work on traditional substrates, leading up to results on Silicon(111) and Silicon(100) in chapters 4 and 5, respectively.

1.1 Group III-Nitrides

Group III-Nitrides are semiconductor crystals comprised of equal parts (by mol) of Nitrogen and elements from Group III of the periodic table, namely, B, Al, Ga and/or In. These crystals can be in both hexagonal (wurtzite) and cubic (zinc blend) arrangements, but this work is concerned purely with the former, which is thermodynamically the lowest energy configuration. The hexagonal wurtzite structure along with some relevant lattice parameters and crystallography is shown in Figure 1. In hexagonal systems, crystallographic planes are denoted by the 4-part Bravais-Miller index (h k i l), where h, k, i and l correspond to intersections with the a_1, a_2, a_3 and c

vectors, respectively. Since a_3 is the negative bisect of a_1 and a_2, h and k determine i ($i = -(h + k)$), so a plane is often specified with only 3 indices (h k . l) or simply (h k l). The same convention of course applies to directions.

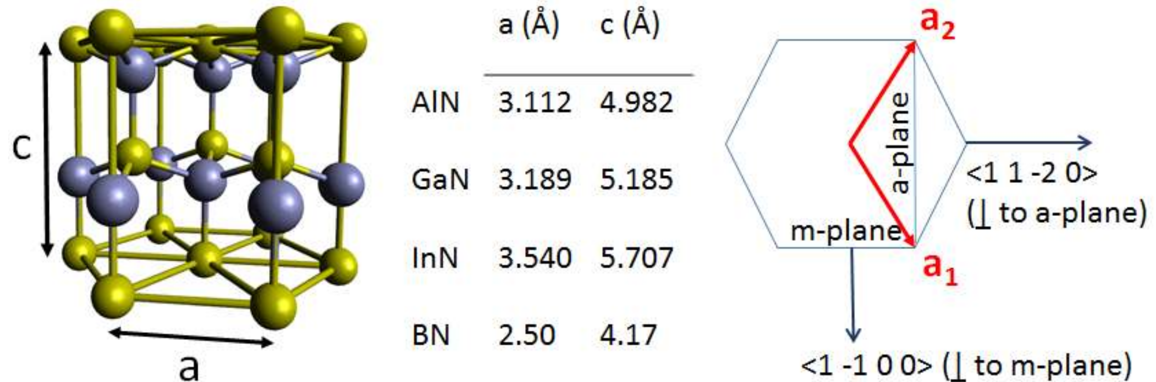

	a (Å)	c (Å)
AlN	3.112	4.982
GaN	3.189	5.185
InN	3.540	5.707
BN	2.50	4.17

Figure 1. (left) The wurtzite hexagonal crystal lattice. The two different colors of the spheres represent the two different chemical elements in the lattice. The a and c parameters are denoted, and their (300K) values for the 4 III-Nitride binaries (center). To the (right) is a projection of the hexagonal base of the lattice, with the m-plane and a-plane indicated as well as their corresponding crystallographic directions.

Figure 2 expresses the bandgap and other properties of Nitrides in comparison with SiC, Si, and GaAs. It's clear that the Group III-Nitride material system has a direct bandgap engineerable over the entire visible spectrum as well as the near infrared and UV spectrums. A particular bandgap can be selected for by incorporating the right proportions of e.g., Ga and In in an InGaN alloy, which would place the system somewhere on the dotted line between GaN and InN on the left part of the figure. These relations roughly follow Vegard's Law, with e.g., $In_{0.3}Ga_{0.7}N$ having a bandgap and in-plane lattice parameter roughly 30% down the dotted line between GaN and InN. These are bulk (fully relaxed) values, and in practice there is not only a bowing parameter, but other strain-induced effects such as band deformation, piezoelectricity, spin-orbit splitting, etc. These effects make characterization crucially important, and the figure should be taken as an expression of the bandgaps available rather than as a roadmap to achieving a particular bandgap.

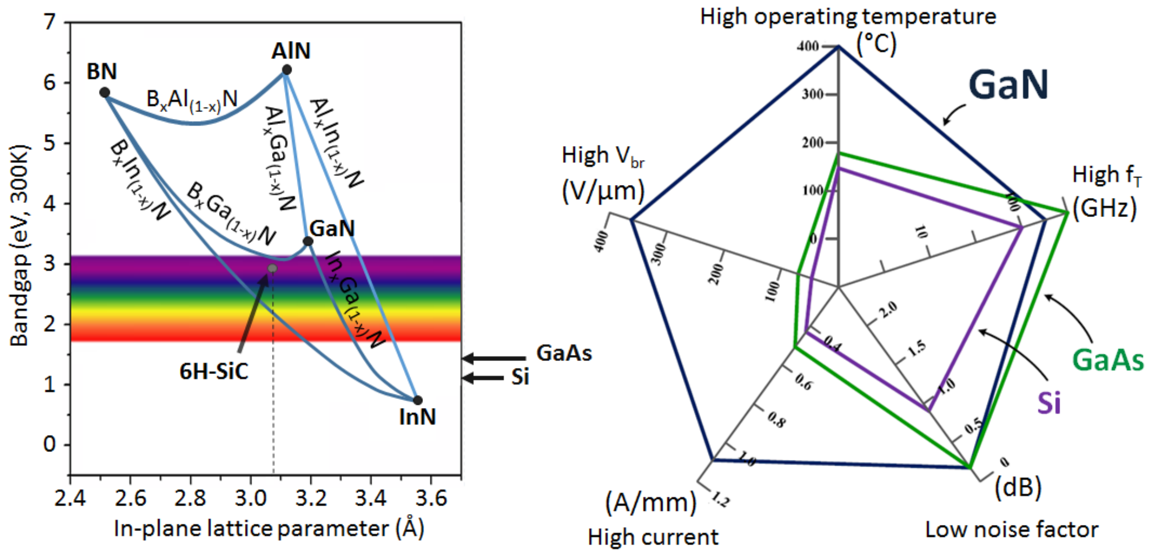

Figure 2. (left) the illustration of (300 K, fully relaxed) bandgaps available to trinaries and quaternaries of (B,Al,Ga,In)N, covering the entire visible spectrum and well into the UV. The dotted lines are to be interpreted as ternaries between the binaries at either side. The bandgaps of Si, GaAs and SiC are denoted for reference. (right) a graphical representation of device-relevant material properties of GaN versus GaAs and Si. While GaAs has a slight advantage in maximum switching frequency, GaN matches or betters the other two in all other categories. Other Group III-Nitrides have similar properties.

The right part of Figure 2 shows the device-relevant material properties of GaN compared to Si and GaAs. For each of the 5 axes, the sense is such that further from the origin is better, even if that means inverting some axes. GaAs has a slight advantage in maximum switching speed, and it matches GaN for noise factor. However, GaN operates at a much higher temperature (more than twice that of GaAs) and is similarly ahead in current density. The most notable difference is in breakdown voltage, where GaN can support fields 5x as strong as can GaAs. These properties extend as well to other Group III-Nitrides.

In addition to these electronic and optoelectronic-relevant properties, Group III-Nitrides also have interesting peizoelectric properties, which vary based on composition and material quality. These properties make it interesting for electromechanical applications, and AlN is used extensively as an RF filter in mobile phones. More importantly is the spontaneous polarization induced by strained layers, which allows the creation of a 2D electron gas (2DEG) at the interface of GaN and a compressively

straining layer. This same effect has also been used by the author to induce a pseudo p-type region by compressive metallization [1].

1.2 2D Heteroepitaxy of GaN

This section will cover the basic physics and consequences of 2D heteroeptixy of GaN, i.e., the growth of GaN epilayers on large surfaces of non-lattice-matched substrates such as SiC, Sapphire and Silicon using techniques such as MOVPE, halide vapor phase epitaxy, and molecular beam epitaxy (MBE). The present work is only concerned with MOVPE, but the contents of this section are relevant to all 3 epitaxial regimes. Also, while we will call by name exclusively GaN, these principles do apply to all Group III-Nitrides.

1.2.1 Relevant substrates

As previously mentioned, heteroepitaxy is necessary because bulk GaN cannot be feasibly grown by conventional ingoting methods. This is because of GaN's extremely high melting point and vapor pressure. We are left then with a small selection of bulk substrates with hexagonal structures and similar-enough in-plane lattice parameters upon which GaN gas precursors can seed crystals. The table below lists the materials who best meet these criteria.

Table 1. in-plane lattice parameters and coefficients of thermal expansion for GaN, AlN, and some bulk substrates.

	Sapphire	6H-SiC	Si(111)	AlN	GaN
Lattice parameter (Å, 300 K)	4.76	3.08	5.43	3.11	3.19
Coef. of thermal expansion ($\times 10^{-6}$ K^{-1})	4.3	10.3	2.5	1.58	3.17

Each of the bulk materials (Sapphire, 6H-SiC and Si(111)) has an associated problem when growing epitaxial GaN. Sapphire and 6H-SiC are both expensive, and Sapphire's

in-plane lattice parameter is 50% larger than GaN's, forcing any GaN crystals that form to either suffer an immense tensile strain or create line and other defects in order to relax. The latter is far more thermodynamically favored, and creates non-radiative recombination centers. SiC, while having a very favorable room-temperature in-plane lattice constant, suffers from a coefficient of thermal expansion which is very different from that of GaN. Since GaN is typically grown at around 1000 ˚C, the different shrinking rate of the substrate from the epilayer during post-growth cooling creates its own defects, including cracks. The defect density in GaN epilayers grown on these substrates tends to be in the range of $10^8 – 10^{10}$ cm^{-2} [2].

Silicon is a very cheap bulk substrate available in extremely high quality. Si(111) is silicon which has been cut such that the (111) plane is exposed for epilayer growth. These planes have the same honeycomb structure as the (00.1) plane of a hexagonal lattice, and so provides a somewhat suitable growth surface. Besides the difference in thermal coefficient, a problem shared with Sapphire and SiC, Silicon also suffers the most mismatched lattice, which is 70% larger than GaN! As if these problems weren't enough, Silicon also has a low melting point, which causes it to degrade under the high temperatures necessary for GaN growth. Clearly, this is the most challenging bulk substrate of the trio.

AlN is not a bulk substrate, but it is included in the table because it is often used as a thin buffer layer atop one of the bulk substrates. Aluminum reacts far more readily with these substrates, which allows us to grow thin (~100 nm) 2D layers of AlN quickly and cheaply, while GaN growth directly on bulk will be slow and tend to form islands. The growth surface provided by the AlN is almost lattice matched to the GaN, and the majority of dislocations present are threading dislocations that have propagated from the interface with bulk. These comprise roughly 10% of the total defect count, so we can see epilayer defect densities in the range of $10^7 – 10^9$ cm^{-2}, a significant improvement.

1.2.2 Defects

Defect density is an important measure of material quality and can be determined using scanning cross-sectional scanning transmission electron microscopy (STEM) and x-ray diffraction (XRD). As far as the importance to device function, defects essentially create non-radiative recombination centers that not only eat carriers, but create localized energy levels inside the forbidden zone of the bandgap. The result is excessive resistivity and heat generation and reduced carrier lifetime, resulting in low device efficiency and lifetime.

As explained in the previous section, the majority of defects occur within the first 100 nm of the epilayer. These defects do not affect devices with active regions more than 100 nm from the interface, and so we don't worry about them. The defects which concern us are those which propagate as the epilayer grows, making themselves felt even in the device region of the material. These defects are called threading dislocations, and they arise principally from the GaN lattice attempting to accommodate the mismatched lattice of the bulk substrate [3]. Figure 3 illustrates this phenomenon. In the left image (credit to Ref. [3]), an STEM of the interface between GaN and Sapphire shows how the GaN lattice breaks its periodicity every 6 or 7 lattice points in order to accommodate the bulk lattice. It does so by twisting or tilting its unit cells near these points to change the spacing of the atoms, as explained in the right image. Dislocations such as these can become threading dislocations, which will propagate upward (in the c direction) by dislocating the unit cell(s) that subsequently grow atop them. These dislocations propagate into the active region of the device and hurt device efficiency.

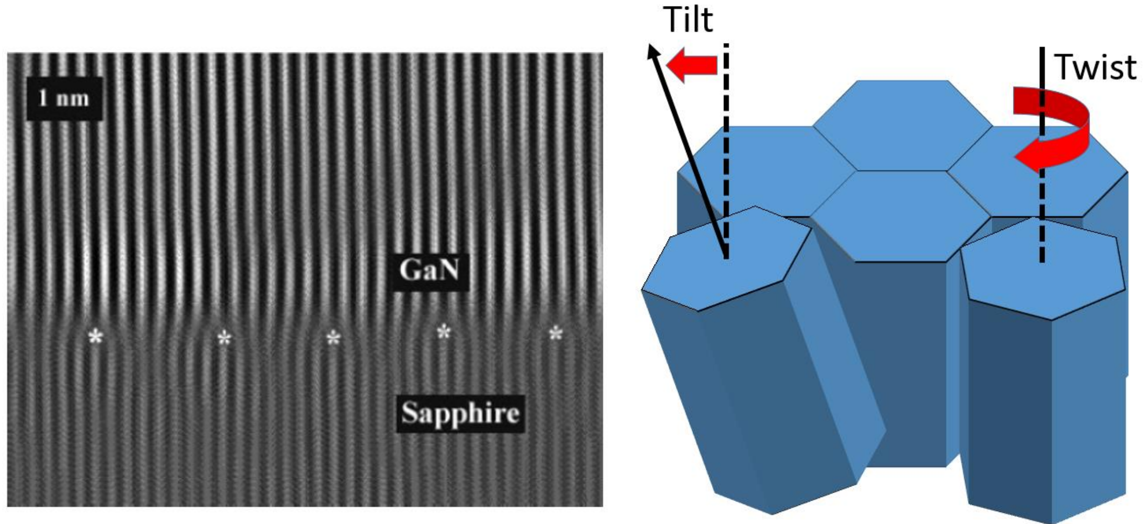

Figure 3. (left) Along the <1 1 . 0> direction (x-axis), the GaN lattice cannot fully bear the tensile strain necessary to accomodate the Sapphire lattice, and every 6 or 7 atoms is forced to skip an atom in the Sapphire lattice [3]. It does so by tilting and twisting its unit cells at these locations (demarked with an asterix) to vary the spacing in its in-plane footprint. These deformations disrupt the periodicity of the lattice, and therefore the band structure, creating band defects. The (right) figure illustrates these two axes of twist and tilt, though it should be understood that any particular dislocation can be a combination of the two.

1.3 Selective Area Growth

1.3.1 Epitaxial lateral overgrowth

In selective area growth, only selected parts of the substrate are exposed to the precursor gases during growth, allowing crystals of layer material to grow on a small area of exposed substrate [4]. This growth suffers normally from propagated threading dislocations. However, if we continue to grow until the horizontal growth of the epilayer overgrows the mask, this portion over the mask is defect free. Figure 4 illustrates this concept. The first step (left) is to mask some of the substrate (which in the case of Group III-Nitride growth can be a bulk substrate, a buffer layer or a poor-quality 2D Nitride epilayer) such that the substrate interface is only partially exposed. The mask is non-reactive with the gas species of our epilayer, so when we proceed to grow the epilayer, it will grow only in the area where the substrate is exposed, as shown in the center image. We fully expect threading dislocations to propagate into this material, but if we continue

to grow our epilayer, we find that growth continues not only vertically, but laterally over the mask, and threading dislocations cannot move laterally. Thus, we create defect-free material over the mask, and this material can be used as the active region in a device.

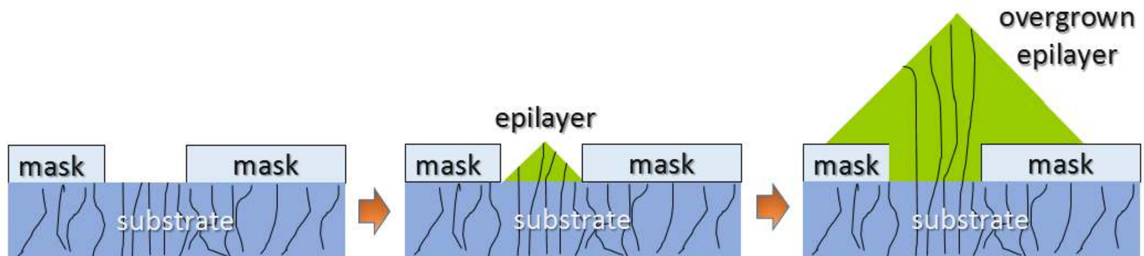

Figure 4. The 3 steps of ELO. From left to right, we first lay a mask on the substrate such that only a partial area of the surface is exposed. A mask is any material that is nonreactive with the epilayer species. In the second step, we begin growing the epilayer, which will only grow in the unmasked area. Threading dislocations will propagate into the epilayer as normal. In the third and final step, we continue growing the epilayer until overgrows the mask. Threading dislocations only propagate vertically, so the overgrown portion of the epilayer is defect free.

It's important to understand at this point that the epilayer material has not grown on the mask. It is not at all attached or bonded to the mask. What has happened was that lateral growth from the epilayer in the unmasked region has overgrown the masked region. Also important to understand is that the material directly over the unmasked substrate is poor quality as in 2D growth, so this material is not useful for devices. We can only use the defect-free portion of the epilayer that has overgrown the mask.

When utilizing the ELO technique by MOVPE, it's possible to adjust growth conditions to favor lateral growth over vertical. This has been extensively studied for the nitride material system in by Hiramatsu *et al* [5].

1.3.2 Nano Selective Area Growth

When our unmasked regions are reduced to the nano-scale (< 100 nm), we find that epilayer growth takes place in a 3D regime which allows fully elastic relaxation of the strained lattice into its lowest energy, stress-free shape [6]. The result is a thin, defect-free, single-crystal nanostructure of epilayer material. Figure 5 illustrates the

geometry of this phenomenon. Both 2D epitaxy and NSAG aim to fit a lattice onto a different lattice. The difference is that NSAG allows the epilayer lattice to relax elastically, while the 2D epitaxy seeks to force the epilayer lattice to maintain its stress, forcing it to dislocate.

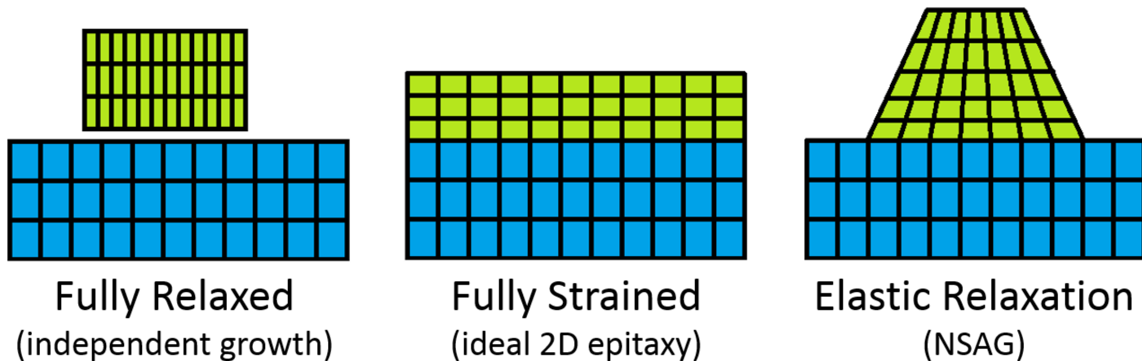

Figure 5. The concept of Nano Selective Area Growth. (left) the blue substrate lattice and green layer lattice are shown in their fully relaxed states. (right) ideal 2D heteroepitaxy, in which the epilayer strains its lattice to accomodate that of its substrate. In practice, this is impossible for large lattice mismatches and will result in threading dislocations in the epilayer as shown in Figure 3. (left) NSAG allows the lattice to elastically relax with each subsequent monolayer of growth, resulting in high quality nanostructures.

In practice, NSAG comes with its own challenges. Since the exposed substrate is so lattice mismatched with the would-be epilayer, the gas species are not much more inclined to seed in the unmasked area than they are on the mask itself, even if this mask is comparatively nonreactive. The result is that different growth conditions need to be explored for different substrates and species to ensure selectivity. Once these ranges are discovered, we often find ourselves very limited in adapting growth conditions to, e.g., engineer our ternary composition to achieve particular bandgaps. Additionally, in the case of Silicon substrates, selective growth conditions tend to be high temperature (to maximize migration lifetime), which begins to degrade the substrate, causing it to become even less reactive with our species. NSAG is the growth technique used for this work, and so these challenges must be addressed.

CHAPTER 2

TOOLS AND TECHNIQUES

In this work we grow Group III-Nitrides using NSAG under MOVPE. These samples are then characterized on the nanoscale to understand the results of our growth conditions and techniques, and this data is used to inform subsequent iterations and/or future growths. Our research cycle and a brief summary of our characterization tools is shown in Figure 6. After undergoing MOVPE, the sample is directly analyzed with SEM to check for selectivity, i.e., whether epilayer growth is limited to the unmasked nanoregions. Depending on our other goals, SEM can of course give other useful information, such as our surface morphology and interface quality for a subsequent growth. Optoelectronic samples that meet our requirements can then be measured by nanocathodoluminescence to study its optical/bandgap properties. Depending on the needs of the project, samples that have proven themselves exceptionally interesting may be taken to the synchrotron for submicron-beam XRD to study the lattices of individual nanostructures. Finally, interesting samples that we are sure we're finished characterizing can undergo cross-sectional STEM/EDX, which can map the lattice, dislocations, and chemistry. This chapter will present these tools and techniques.

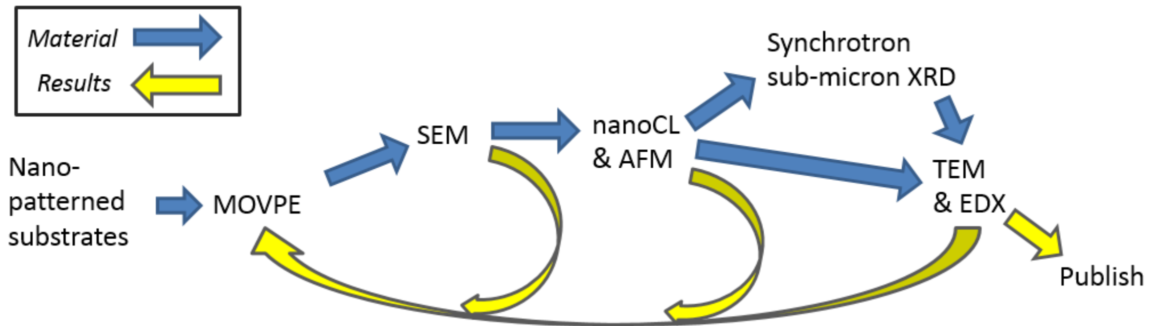

Figure 6. Our research cycle applies nano-characterization techniques to provide results that inform future growth. Less costly techniques serve as a first filter, saving more involved techniques for samples found to be interesting. (SEM) Scanning electron microscopy is used to confirm NSAG selectivity and evaluate geometry and surface morphology. (nanoCL) Nanocathodoluminescence is used to study the bandgap and emission quality and to estimate the chemistry. (AFM) Atomic force microscopy is sometimes used to map the height of our nanostructures. (sub-micron XRD) Synchrotron-based submicron-beam x-ray diffraction can give the complete lattice and strain information. (TEM&EDX) Cross-sectional transmission electron microscopy and energy-dispersive X-ray spectroscopy are used simultaneously to study the interiors of the structure and map the dislocations and chemistry. This process destroys the sample, so it is saved for very last.

2.1 NSAG under MOVPE

2.1.1 Mask patterning

The first step of NSAG growth is to create the mask pattern on a substrate, either a bulk substrate or some buffer-layered template. The finished mask pattern should be an unreactive covering with a collection of nanoscale apertures through which the underlying substrate is exposed. The NSAG 3D growth effect can be observed when the aperture is less than 100 nm wide and there are no more than several tens of microns of nonreactive mask between apertures. The reason for the second criterion is that 'nonreactive' is a relative term which means that the epilayer species have a relatively long migration lifetime on the mask before reacting. To achieve selectivity, we must be sure the masked area is small enough that the species will migrate onto some exposed substrate before it reacts with the mask. We've determined this maximum mask area to be around 50 μm between two regions of exposed substrate.

For our early work (before 2014), mask patterning was accomplished by e-beam lithography of photoresist, followed by reactive ion etching. A 100 nm SiO_2 dielectric

mask is deposited on the substrate by chemical vapor deposition, followed by a spin coating of negative photoresist. Then, the area to be covered by mask is subjected to e-beam lithography, followed by development to remove the unwanted (unilluminated) photoresist, exposing the dielectric SiO_2 where we intend to put our apertures. Then reactive ion etching is applied to these exposed areas to remove the dielectric mask beneath. Finally, the remaining photoresist is stripped, leaving a SiO_2 mask with nanoapertures for NSAG. Figure 7 illustrates this process and shows examples of patterned masks created for early work.

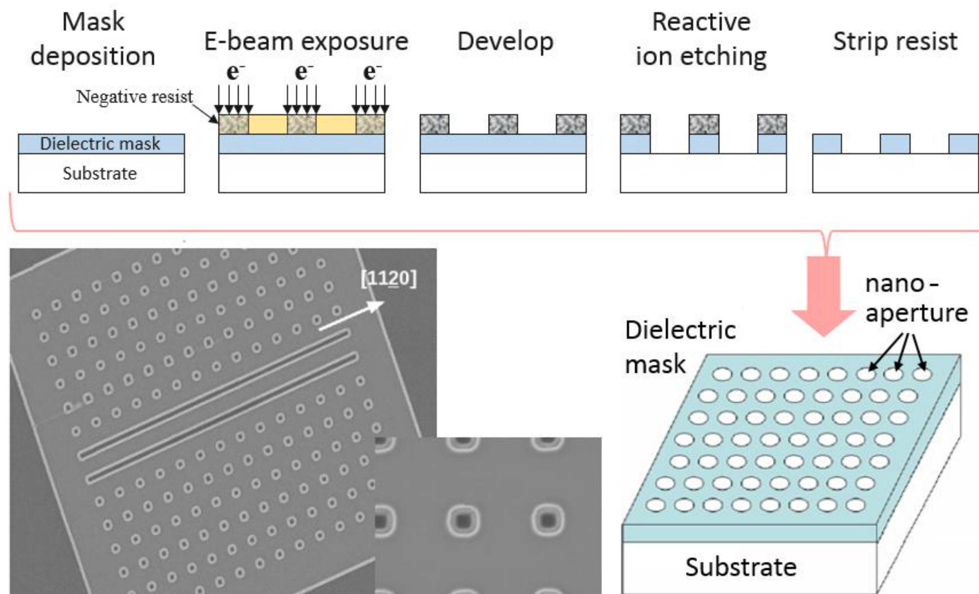

Figure 7. The early masking process for NSAG. (top) from left to right, the steps to making a patterned mask. We begin with a substrate (white) and deposit a dielectric mask (blue). Then we spin coat a negative photoresist (yellow) and illuminate with e-beam lithography the areas we wish to keep masked (textured). Once developed, the unilluminated regions dissolve. Then we perform reactive ion etching to remove the dielectric mask exposed by those dissolved regions and then strip the mask. An example of the resulting structure is shown at the bottom right. The bottom left shows some SEM images of actual mask patterns. The circles are 80 nm apertures, and the darker grey towards the image edges are unmasked regions (where 2D epilayer growth would occur).

The shortcoming of this method is the number of steps and the need to carefully control the etching step so as to completely open the aperture without over-etching into the substrate. Since 2014 [7], we've begun using a different technique wherein hydrogen

silsesquioxan is spincoated directly onto the substrate, and then a 4 nm FWHM electron beam (100 kV accelerating voltage under a 1.9 nA current) is used to illuminate the areas we wish to mask. These areas will cross-link to form SiO_2, and the unilluminated area is wet-etched away in a 25% tetramethyl ammonium hydroxide solution, leaving apertures and unmasked area. Figure 8 illustrates the procedure.

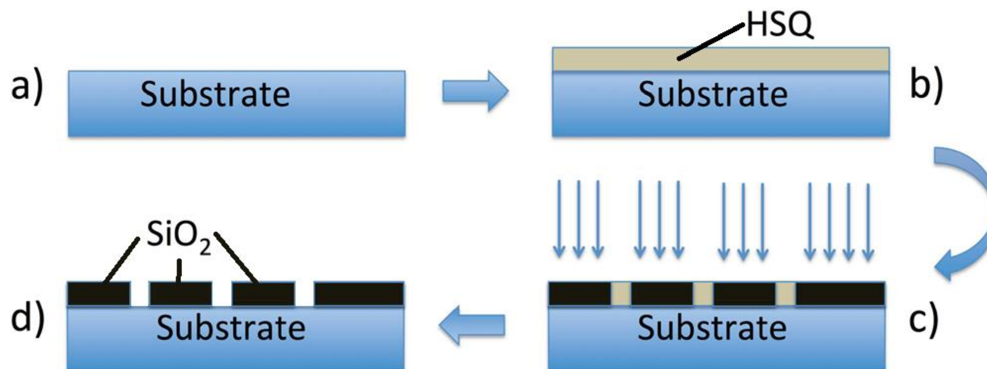

Figure 8. The new mask patterning method. a) The bare substrate is b) spin-coated with HSQ, and is then c) selectively illuminated by e-beam lithography, causing illuminated areas of HSQ to cross-link into SiO_2. A wet etch then produces a mask pattern as in d), with apertures in the areas which were not illuminated. http://dx.doi.org/10.1063/1.4900531

2.1.2 MOVPE

Metal organic vapor phase epitaxy is a growth technology wherein the elemental components of the material we wish to grow are delivered into a growth chamber as metalorganic vapors carried by Nitrogen or Hydrogen. The metalorganic vapor is a gaseous compound of a Group III metal and an alkyl group, and the Nitrogen is delivered via ammonia. The carrier gases are used to create pressure and control flow. In this work, the metalorganic vapors used are trimethlygallium (TMGa), trimethylalimunum (TMAl) and trimethylindium (TMIn).

Once introduced into the growth chamber, the temperature and pressure cause pyrolysis into constituent gas species, which then diffuse and adsorb into the substrate. Species that find each other near a suitable nucleation site react to become part of the lattice of the forming epilayer. The free methyl groups and hydrogen formed during

pyrolysis combine to create methane, which can be pumped out of the growth chamber to make room for new precursor gases.

All growths in this work were performed in our homemade T-shaped reactor [8], which is a reactor where the precursor vapors pass over the sample horizontally rather than rain down from above. During growth, the sample spins at up to 60 rpm to maintain uniformity. A built-in reflectometer (not discussed in this dissertation) can monitor *in situ* the growth progress and surface roughness. Figure 9 illustrates the form and function of our T-shaped reactor.

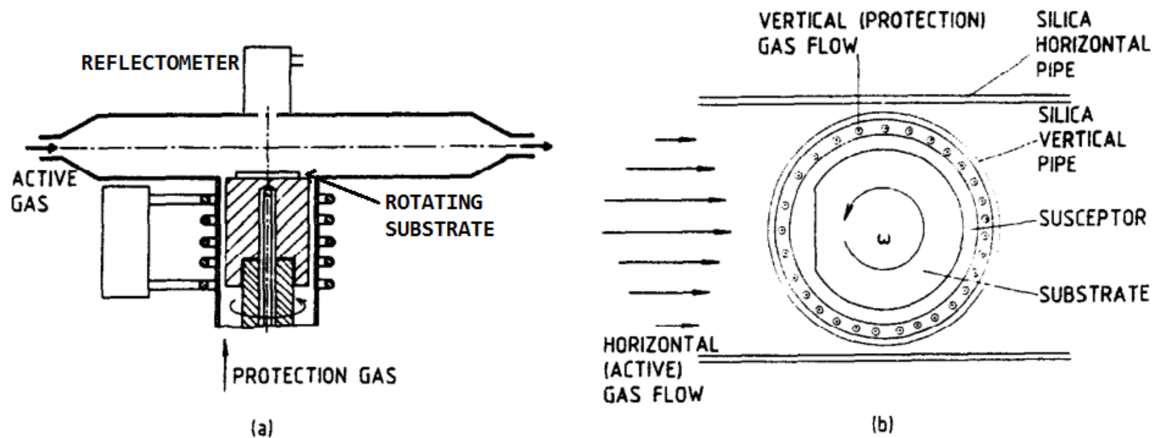

Figure 9. The side (left) and top (right) views of the homemade T-shaped reactor. Precursor gases arrive from the left and gaseous products and nonreacted gases are exhausted to the right. A reflectometer is mounted above the substrate. The substrate is on a rotating stage to assure uniformity, and a protective ambiant flow of Nitrogen or Hydrogen from the bottom prevents reactive gases from collecting in the vertical part of the reactor.

2.2 Scanning Electron Microscopy

SEM uses high-momentum electrons to excite surface atoms of the sample and interpret the transmitted electrons, backscattered electrons, secondary electrons, and characteristic photons that result in order to create a topographical image of the sample surface. With proper focusing, it can see details at the sub-nanometer scale. Our use case relies on collecting secondary electrons, the intensity of which can be related to the angle at which the high-momentum exciting electrons strike the surface, i.e., more

inclined surfaces emit more secondary electrons upon ionizing excitation. By scanning our excitation beam across the sample, we can thusly map the inclination of the sample surface, which gives us a highly accurate topology. Figure 10 illustrates the basic workings of our scanning electron microscope and shows some example images obtained in the course of this work.

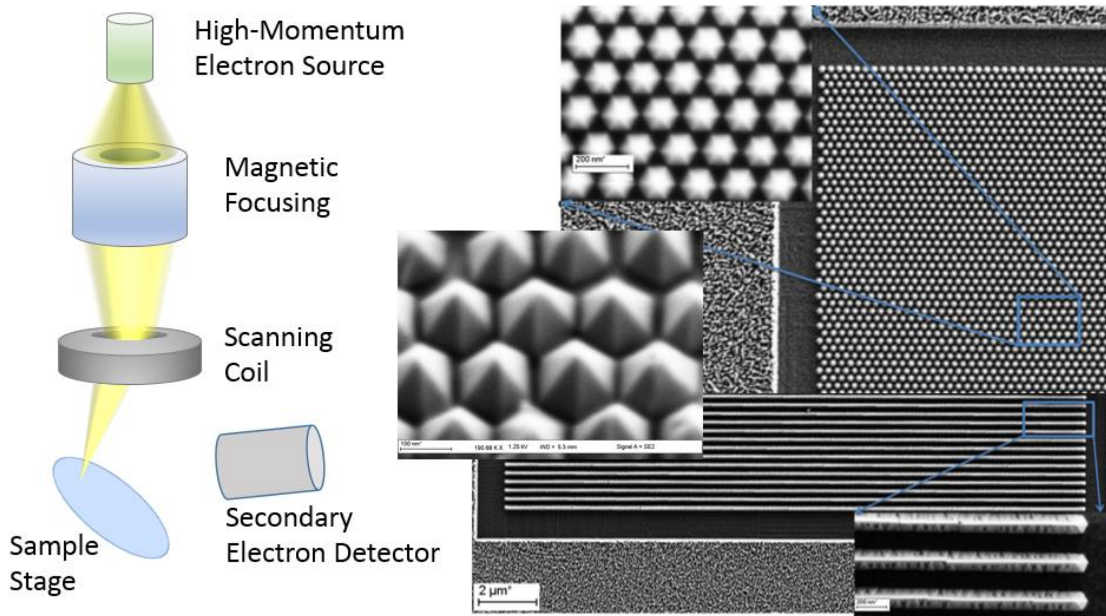

Figure 10. Scanning Electron Microscopy apparatus and example images. (left) Our scanning electron microscope is comprised of a high-momentum electron source, which emits electrons toward magnetic focusing optics, creating an electron beam focal point that is then displaced across the sample surface by a scanning coil. Secondary electrons are detected, allowing us to map the inclination of the sample surface. To the (right) are some example SEM images taken of GaN nanostructures grown using our NSAG technique on a GaN-buffered Sapphire substrate.

2.3 Nanocathodoluminescence

The same high-momentum electron beam focusing apparatus that makes SEM possible also provides the necessary precision and excitation to perform nanocathodoluminescence. When the material is excited by the electron beam, electron-hole pairs are created. They recombine a few nanoseconds later, emitting photons, which are then collected and analyzed by spectrometer. The wavelengths of the emitted photons tells us what energy level transitions exist in the band structure of the material ($\Delta E = \frac{hc}{\lambda}$).

This gives us information not only about the bandgap, but also about the defect bands inside it, telling us about the types and densities of defects in the sample. Additionally, increasing the electron momentum increases penetration depth into the sample, which allows us to perform depth-sensitive measurements. Our setup allows electron energies up to 30 keV, which in GaN allows penetration around 500 nm beneath the surface.

2.4 Atomic Force Microscopy

SEM provides beautiful, publish-worthy images, but when we need to precisely know the height of features, e.g., for determining root-mean-square surface roughness, AFM is the preferred tool. For this work, the atomic force microscope is used in tapping mode. The principle of operation is an extremely sharp-tipped (several tens of atoms) tooth on the end of a vibrating cantilever. The cantilever oscillates at its natural frequency with a constant amplitude until it is brought close enough to the sample that the tooth begins to feel forces originating from the sample surface. This reduces the amplitude of oscillation by Hooke's law, and by scanning the tooth across the sample surface, we can create a force map which can be interpreted as a highly precise topology map. The amplitude of the cantilever oscillation is tracked both by piezoelectric mechanisms at the base of the cantilever and by displacement of a laser reflection off its oscillating tip. Figure 11 illustrates the function of the tapping mode.

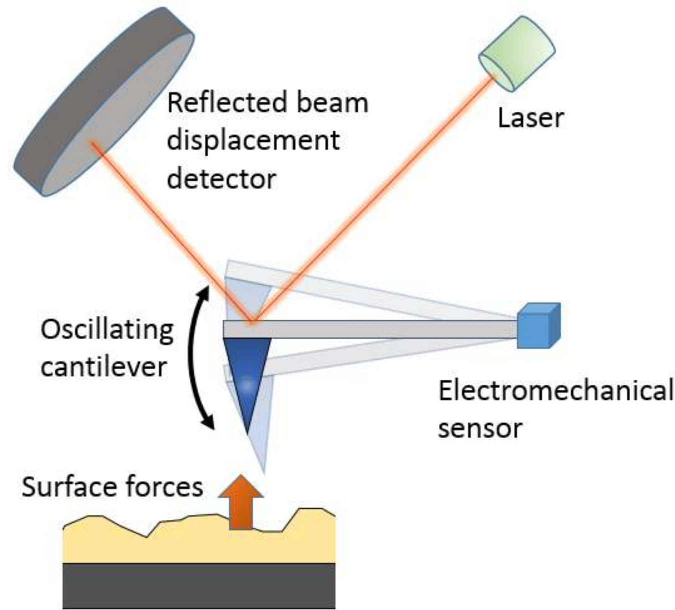

Figure 11. Atomic force microscope in tapping mode. The cantilever oscillates at its natural frequency near the sample, and surface forces reduce its amplitude. Simultaneous monitoring of the cantilever oscillations by an electromechanical sensor and laser reflection displacement provide a highly precise measurement of these forces, which can be used with scanning to map the sample surface.

2.5 Synchrotron-Based Submicron-Beam X-Ray Diffraction

XRD gives information about chemical composition, how stress is released and what sorts of dislocations (if any) are forming as a result [9-11]. This type of information is of key importance to the research cycle when growing on mismatched substrates, and yet, applying XRD measurements to nano-scale group III-Nitrides is not trivial. Focusing the beam results in massive momentum spread, which correspondingly reduces the accuracy of lattice determination, and yet using a large beam illuminates many nanostructures at once, making it impossible to distinguish orientation differences not only between nanostructures, but between regions of the same nanostructure [12, 13]. The nano-scale group III-Nitride system also creates many unexpected and nontrivial problems with sample alignment, strain calibration, and locating individual nanostructures [14]. This section will describe achieving submicron-beam XRD of nanostructures on highly mismatched substrates, which was a key challenge in completing this work.

2.5.1 XRD Basics

XRD is an immense subject, so our discussion will be limited to what is relevant to the current work. Constructive interference of diffracted x-rays in crystals is described by Bragg's Law [15], $n\lambda = 2dsin\theta$, where n is an integer indicating the order (higher orders have less intensity), λ being the wavelength of the x-rays, d being the spacing between the crystallographic planes normal to the bisect of the incident and diffracted x-ray beams, and θ being the angle between the incident and the crystallographic planes normal to the bisect. Figure 12 illustrates Bragg's Law.

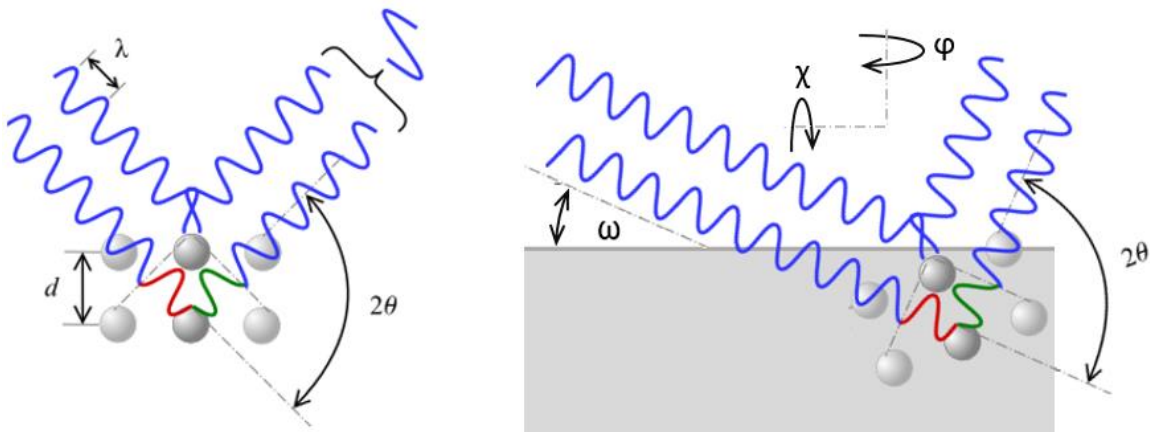

Figure 12. (left) Bragg's Law illustrated. Two coherent photons are elastically scattered by two atoms. When the difference in length between the path of the first photon and the second photon (2dsinθ) is exactly an integer times the wavelength (nλ), the two emitted wavelengths constructively interfere, creating a strong diffracted signal at a detector placed at the appropriate angle. The (right) image describes the angles ω,φ and χ, which describe the twist and tilt of the sample surface with respect the crystallographic planes being targeted. These angles are nonzero when the crystallographic planes being studied are not parallel to the sample surface.

Often, we wish to study crystallographic planes (called *reflections* in XRD) which are not parallel to the sample surface. In this case, in order to achieve the Bragg conditions, we need to tilt and/or twist the sample such that these planes are normal to the bisect of our incident and diffracted beams. This tilting/twisting has three degrees of freedom, denoted in a 4-circle goniometer setup (our setup) by ω, χ, and φ, which are the angle between the sample surface and our incident beam, the angle between the sample surface normal and the plane created by our diffracted and incident beams, and the angle

of twisting around the surface normal, respectively. ω is shown in the right image of Figure 12. χ can be understood to be the angle around the horizontal axis, and φ can be understood to be the angle around the vertical axis. These angles were left off the figure to reduce clutter, but they can be understood to be perpendicular to each other, together creating a complete 3D rotation space for the sample.

The most basic application of XRD is determining the lattice parameters *a* and *c*. To do this, we use Bragg's law to find the *d* spacing for two reflections defined by nonparallel Miller index sets. The most commonly used for Group III-Nitrides are (0 0 . 4) and (1 0 . 5), because they have a good balance of high-θ (small beam footprint) and high intensity (small order *n*). The formula for *d* at miller indices (*h k* . *l*) of a hexagonal lattice is:

$$d = \frac{1}{\sqrt{\frac{4}{3a^2}(h^2 + k^2 + hk) + \frac{l^2}{c^2})}}$$

If we find *d* for two different *hkl* sets, we have two equations with which to solve for two unknowns.

We can obtain information about defects using the full-width-at-half-maximum (FWHM) of the diffraction signal. If, for example, we try several values of ω around the Bragg conditions for a reflection and find the FWHM of our *a* parameter, we have some indication of mosaic spread, i.e., variations in the lateral dimension of the unit cell. This is a good general indicator of defect density. Determining more specifically what sort of defects are contributing to this spread requires looking at the FWHM of signal around our other angles as well. For example, the FWHM of a χ scan around a reflection with nonzero *h* and *k* will tell us about tilt dislocations. Of course, all these FWHMs must be

decoupled from the momentum spread of the incident x-ray beam and deconvoluted from the acceptance range of the detector before any solid numbers can be obtained.

2.5.2 Submicron-beam XRD

X-rays mostly pass through the sample without scattering, so the diffracted intensity from very thin layers is only a tiny fraction of the incident intensity. Additionally, focusing x-rays requires the use of monochromation, Fresnel zone plate optics and an order-sorting aperture, depletes incident intensity through wavelength selection, imperfect focusing efficiency and order selection, respectively. As a result, submicron-beam XRD of nanostructures uses only a fraction of the original intensity to illuminate a tiny lattice, which means that if we hope to have a workable diffracted intensity, we need a really powerful x-ray source to begin with.

For this, we rely on synchrotron-based light sources. X-ray diffraction in the present work has been carried at the Advanced Photon Source at Argonne National Labs (IL, USA) and Cornel High Energy Synchrotron Source at Cornell University (NY, USA). Our submicron-beam XRD setup is described in Figure 13, which shows both the focusing/selection optics and the detectors for both fluorescence and diffracted x-rays. Fluorescence detection is critical for submicron-beam work, because it allows us to understand where on the sample surface we are illuminating. This will be discussed more thoroughly in the next section.

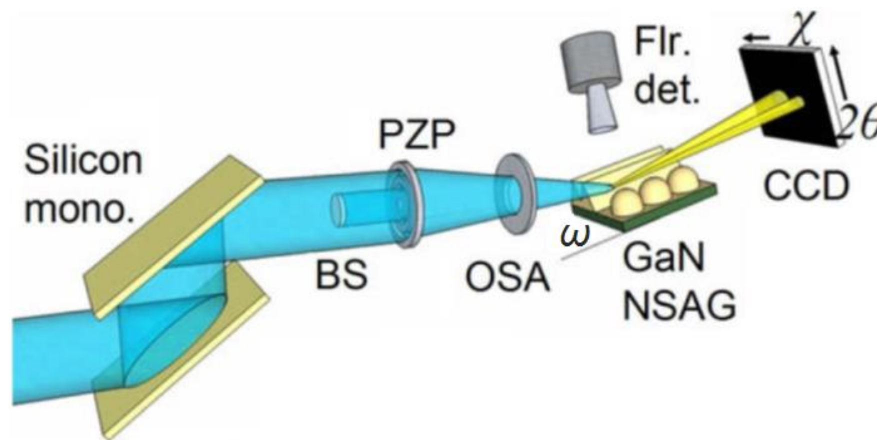

Figure 13. Our submicron-beam XRD setup at Advanced Photon Source (IL, USA). Relativistic electrons accelerated by the synchrotron are injected into the storage ring, where they emit x-rays. A portion of these x-rays are shined at a Silicon monochrometer (Silicon mono.), which select only a very narrow energy range of around 10.5 keV. This monochromatic beam is then foccused through a Fresnel phase zone plate (PZP) with a beam stop (BS) in the center, assuring the focal point at the sample (GaN NSAG) contains only focused x-rays. An order sorting aperture (OSA) assures that only the circular first order focal point reaches the sample. A fluorescence detector (Flr. det.) collects x-ray-excited fluorescence, which gives a crude chemical and thickness map of the sample, helping us to understand where on the sample our x-ray beam footprint is illuminating. Diffracted intensity is collected by a CCD detector, which allows a range of χ and 2θ angles to be collected at once. The sample stage can move in XYZ and can rotate in φ, giving us full 3D control of our sample in angle and cartesian space. http://dx.doi.org/10.1016/j.nimb.2009.09.016

2.5.3 Submicron Beam XRD of Nanostructures on Highly Mismatched Substrates

Characterizing heteroepitaxially grown nanostructures is often a matter of using a smaller probe/spot size. For submicron-beam XRD, it's not so simple. Finding the individual nanostructures is not trivial, since for a scan of reasonable speed, the rms roughness of the unmasked part of the sample is of the same order as the size of the entire mask, which itself is often around 10 μm across and contains nanostructures every 150 nm or so. Also, when the structures of interest are very small (and the spatial resolution requirements very high), slight misalignment between the sample surface and axis of θ rotation cannot be ignored. If the misalignment is not properly corrected, the focused beam footprint will wander across the sample surface during sample rocking measurements, which are essential for determining not only FWHMs, but even seeking the diffraction maxima for accurately determining *d* spacing. Lastly, calculating strain without a nearby reference signal of a known lattice is not straightforward. The only

reference signal available is the mismatched lattice, which is 10 deg away for the (0 0 . 4) reflection. At this distance, slight misalignments between the sample space, the goniometer angle space, and the CCD detector become significant. This section describes novel XRD techniques specifically adapted to characterization of particular nanostructures grown on highly mismatched substrates.

Finding the Nanostructures

In order to achieve selectivity, masked regions must be as small as possible, surrounded by immense unmasked regions to collect all the migrating species that do not find an aperture. In our samples, typical mask size was on the order of 10 μm, surrounded by at least 100 μm of unmasked "field." Growth in the field is therefore 2D, and of very low quality, full of pits and v-defects and other thickness nonuniformities. These masks contained apertures, often spaced quite densely, which after epitaxy created a situation in which only about a 1 μm margin of contiguous mask is left exposed. If we wanted these margins to be distinguishable from the field, we would need a submicron step size, which means that even if we could narrow down our search to a 1 mm^2 region of the sample surface, we would need to take over 106 points of data, which would take around 24 hours!

Our solution to this is a grid of easy-to-find markers, which allow us to quickly understand where we are on the sample relative to our structures of interest. An example of a good marker would be a strip of Fe, which would fluoresce at 6.4 keV (Fe-K), and be very easy to find using the fluorescence detector. Another example which we used is a series of masked stripes around 50 μm wide and 100 μm long. Scanning for these is much faster, since we only need a few width-wise low-resolution scans to distinguish such large masks from field topology. We can then refer to a map of the sample and offset our beam footprint such that we're sure to be within around 100 μm^2 of our nanostructures, wherein a fine-toothed scan is reasonable.

Keeping the nanostructures under the beam footprint

When the θ axis is not exactly aligned with the sample surface, the beam footprint wanders across the sample surface during rocking. Many researchers mistakenly ascribe this to microvibrations in the goniometer. However Figure 14 explains the geometry of this phenomenon. This effect is significant for nanostructures, because moving the beam footprint even a few 10s of nanometers can lose the nanostructure entirely. In order to be able to perform such measurements on nanostructures, we must perform an alignment. A scan of Ga-K fluorescence will show us the general shape and exact position of the GaN nanostructure. Alignment can be achieved by adjusting the elevation of the sample surface (Z axis) until this fluorescence profile doesn't change under rocking.

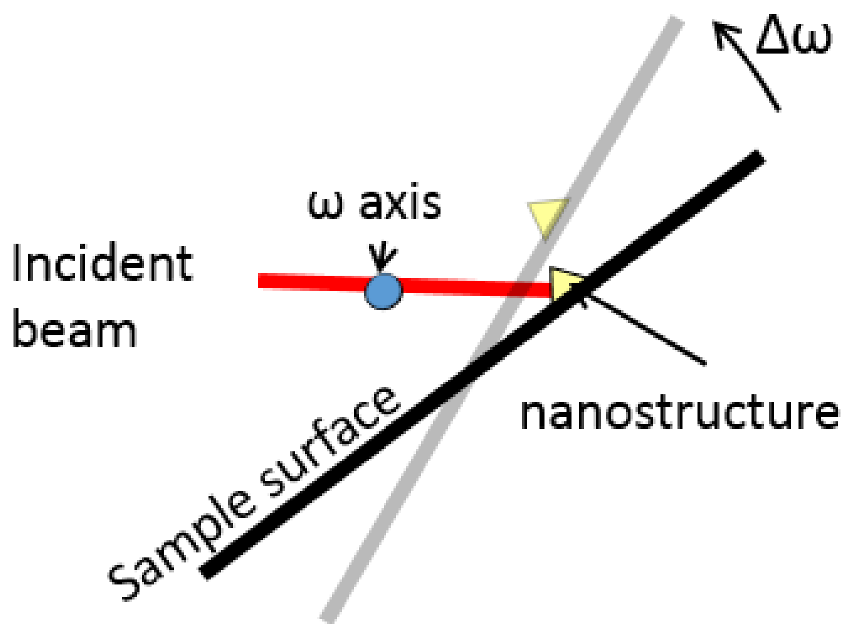

Figure 14. Illustration of the effect of imperfect sample surface alignment with the θ axis of rotation. When the axis is not on the sample surface, rotation causes the beam footprint to move along the surface. A misalignment of only a few microns can be enough to lose illumination of the nanostructure during a 1 deg rocking measurement. http://dx.doi.org/10.1016/j.nimb.2009.09.016

Calibrating for goniometer misalignment

In most XRD use cases, calibration amounts to shifting the angle space such that a nearby reference signal aligns with theoretical values. This doesn't apply to the case of

highly mismatched substrates, where the nearest reference signal can be 10 deg or more away. For calibration in this case, we need to find at least two reference signals and use their locations to determine the misalignment between the actual sample space and the goniometer. Figure 15 shows the relationship between example reference signals, (00.4) and (00.6), and sample-goniometer misalignment, ψ.

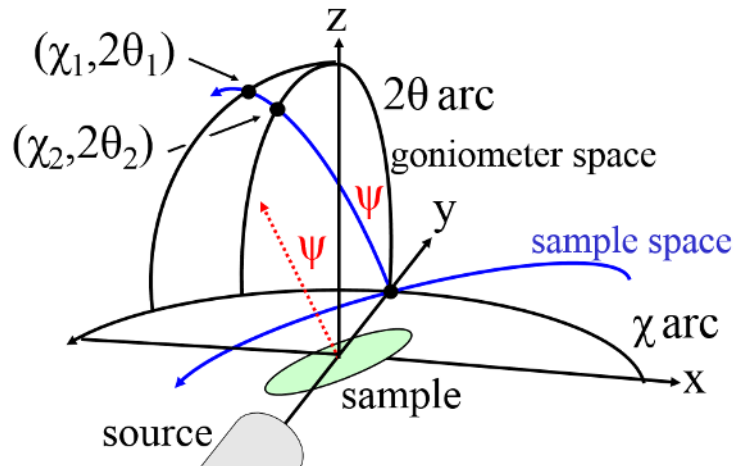

Figure 15. Qualitative effect of sample tilting around the straight beam axis on actual χ and 2θ arcs in the reciprocal space of the sample (blue) relative to goniometer arcs (black). z direction is the sample stage elevation; y direction is the direction of the straight, undiffracted beam. (χ1, 2θ1) and (χ2, 2θ2) represent the angular positions of two different reflections of the substrate. Tilting of the sample mounting by ψ around the straight beam direction causes the same tilt in reciprocal space relative to the goniometer space. Finding in the goniometer system the position of two reference signals whose theoretical positions in reciprocal space are known allows us to calculate and correct for ψ, determining the reciprocal space. http://dx.doi.org/10.1016/j.nimb.2009.09.016

By knowing the theoretical Bragg conditions of two substrate reflections, ($\chi_{Bragg,1}$, $2\theta_{Bragg,1}$) and ($\chi_{Bragg,2}$, $2\theta_{Bragg,2}$), and noting the measured positions of these reflections in the goniometer coordinate system, (χ_1, $2\theta_1$) and (χ_2, $2\theta_2$), we can determine the degree of tilting and map the $(\chi, 2\theta)_{gonio}$ values reported by the goniometer into corresponding actual (χ, 2θ) values in the reciprocal space of the sample. It can be shown that:

$$\psi = \sin^{-1}\frac{\cos 2\theta_1 \cdot \cos 2\theta_2 \cdot \sin(\chi_1 - \chi_2)}{\sin(2\theta_{Bragg,1} - 2\theta_{Bragg,2})}$$

Then, the goniometer coordinate system $(\chi, 2\theta)_{gonio}$ can be mapped to the actual reciprocal space coordinate system by:

$$\begin{pmatrix} \chi \\ 2\theta \\ 1 \end{pmatrix} = R_y(-\psi) \begin{pmatrix} \chi_{gonio} \\ 2\theta_{gonio} \\ 1 \end{pmatrix}$$

where R_y represents a rotation around the y (straight, undiffracted beam) axis in Cartesian space.

If precision is especially important, then we need very accurate $(\chi_1, 2\theta_1)$ and $(\chi_2, 2\theta_2)$ values. Point detectors lend themselves well to this, but CCD detectors are far more useful for taking 3D crystallographic data quickly. If a CCD detector is the detector being used, then its misalignments must be accurately deduced before the goniometer misalignment can be identified and corrected for.

CCD Calibration is complicated to describe and is only really important when the experimenter does not have a point detector available for goniometer calibration, and even then only so much as the mounting is imperfect. The interested reader is referred to Ref [14].

2.6 Transmission Electron Microscopy

STEM operates much like optical microscopy, only with electrons instead of photons being passed through a sample thin enough to be partially electron transparent. The higher (De Broglie) wavelength of electrons compared to optical photons gives STEM Angstrom-scale resolutions. Using focused ion beam etching, we can prepare cross-sections which show atomic-level detail of our sample from any perspective we choose. This is a time consuming and destructive process, so is only performed on

particularly interesting samples that have already been extensively studied by other characterization methods.

An STEM setup is essentially an SEM setup (see Figure 10) with different detection apparati. In the current work, we use the “high-angle annular dark field” detection setup, which means we use a ring-shaped detector that ignores directly transmitted electrons and only collects electrons that have scattered while passing through the sample. By looking only at scattered electrons, our collected energy is almost purely a function of atomic number, Z, of the atoms at each point in the scan. Barring thickness nonuniformity, the resulting intensity map reveals individual atoms, the intensity of which is directly related to their Z. Thus, we can distinguish individual atoms and look directly at our crystalline structure. An example of this, along with the HAADF STEM setup is shown in Figure 16. A “bright field” operation mode can be performed simultaneously by collecting only the electrons that pass through the inner ring of the HAADF detector. Some features are more obvious in the bright field mode, but this mode is subject to artifacts due to diffraction effects,

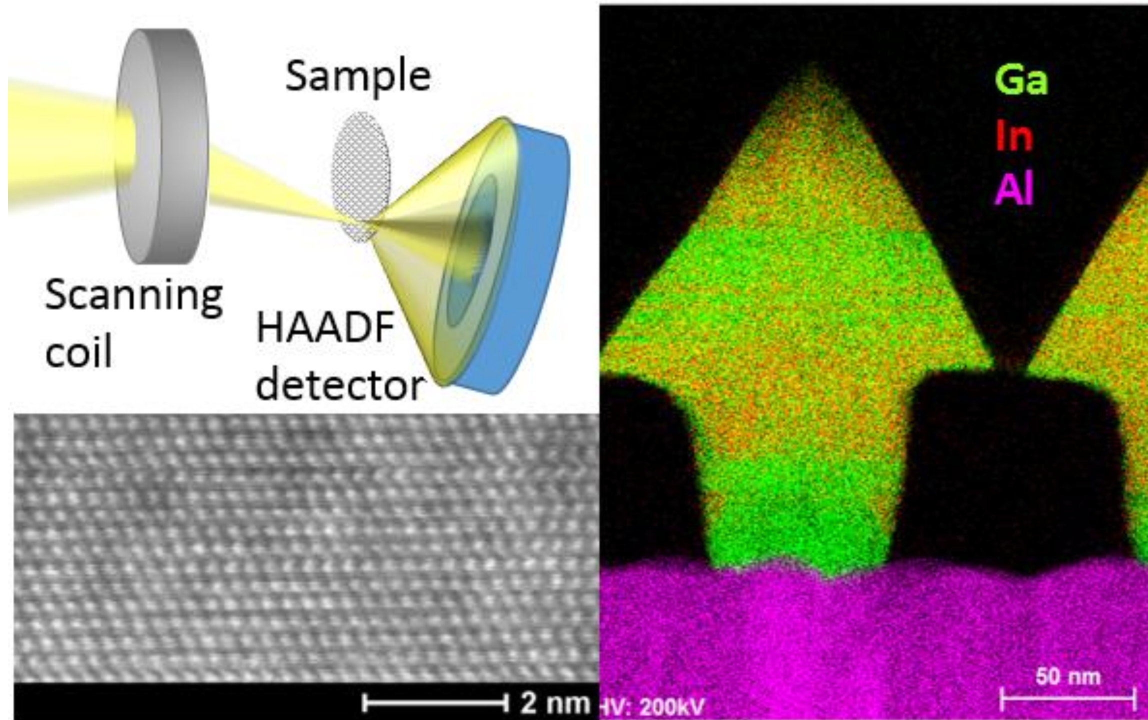

Figure 16. (top left) HAADF STEM setup. The ring-shaped HAADF detector does not collect directly transmitted electrons, only those that have been scattered. (bottom left) high-resolution HAADF STEM image of InGaN showing individual atoms. (right) superimposition of 3 EDX maps of Ga (green), In (red) and Al (purple) of an InGaN-on-GaN nanostructure grown on AlN.

We often simultaneously collect x-rays emitted by the sample cross-section as it absorbs electron energy. The x-rays emitted are characteristic of the band structure of each atom, which allows us to map the chemical composition of our cross-section, even without using atomic resolution. This is called energy dispersive x-ray spectroscopy, and example image is shown in Figure 16.

CHAPTER 3

SELECTIVE AREA GROWTH ON TRADITIONAL SUBSTRATES

This chapter details work on traditional (expensive, no Silicon) substrates. Some of this is preliminary work from before the proposal, and much of it is new work as we continue to master more aspects of NSAG on GaN templates before applying these techniques to Silicon. The first section is on micron-scale selective area growth from as early as 2008. The second section is on the early work with GaN NSAG, followed by NSAG work with the ternaries InGaN and AlGaN, and finally the fabrication of GaN microtemplates by coalescing NSAG structures.

3.1 MicroSAG

The beginnings of this work were in the microSAG regime. The first experiments were to select the dielectric material of the mask. Recall that to achieve selectivity, we need a mask material that has a very low reaction rate with the epilayer species. Two mask materials were tested under numerous growth conditions, Silicon Nitride (Si_xN_y) and Silicon Dioxide (SiO_2). For the substrate, we used GaN-buffered-Silicon, because the GaN surface, though extremely poor quality, should have maximum reactivity with the GaN epilayer species. Results are shown in Figure 17, and are highly conclusive, with only SiO_2 resulting in perfect selectivity. This can be explained by the reactivity between our epilayer species and Si_3N_4 [16].

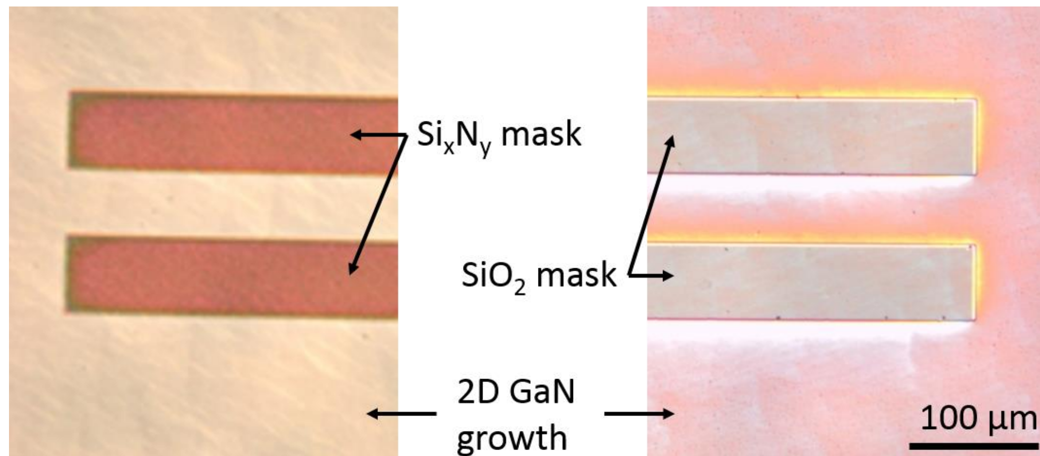

Figure 17. Comparison by optical microscopy of SAG using Si_xN_y (left) and SiO_2 (right) masks on GaN templates. Colors for each image were selected for best contrast. The Si_xN_y mask is found to be covered in polycrystaline GaN deposits, while the SiO_2 masking resulted in perfect selectivity.

Subsequent experiments were performed to explore the properties and physics of GaN SAG. The vapor phase diffusion model [17] for SAG is supported by experiments with large mask widths, because these growths exhibit drastically enhanced growth at the mask interface. See Figure 18 for a dramatic example. The maximum selective mask width predicted by this model was found to be about 50 µm for GaN.

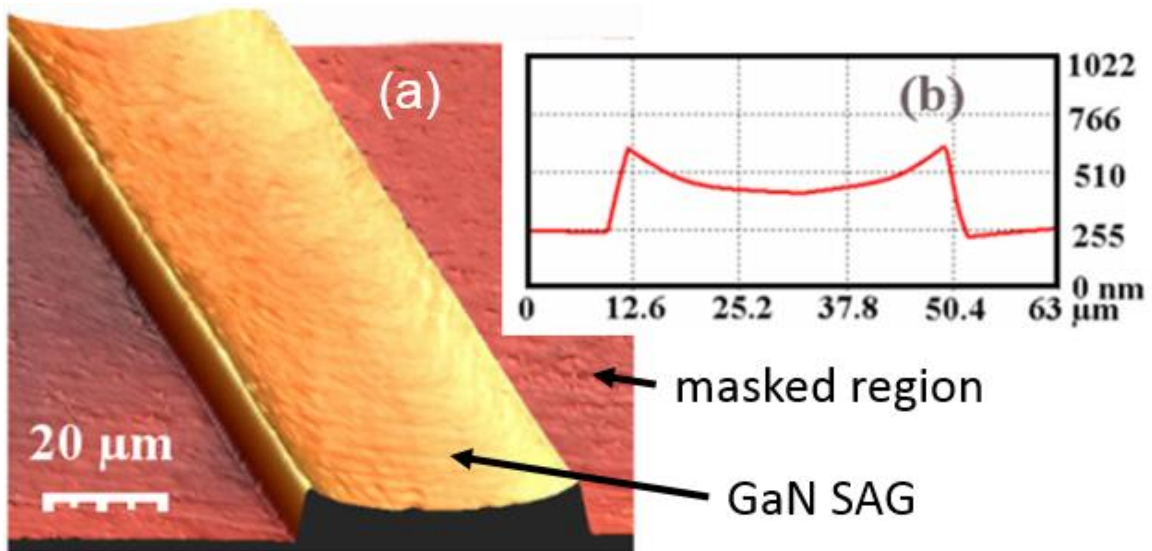

Figure 18. AFM of GaN microSAG on a SiO2-masked GaN template showing enhanced growth near the mask boundaries. (a) is a perspective reconstruction based on a 2D AFM map and (b) is a profile across the length of the growth.

The 3D stress relief mechanism described for NSAG [6] was found to apply also to microSAG, but only at the edges, where the lattice has some freedom to expand/contract. Figure 19 shows an XRD analysis of GaN hexagonal prisms SAG on Sapphire. In the bottom left CCD image of diffraction intensity from the (00.4) reflection, the submicron beam footprint illuminates the entire left side of the pyramid, albeit weakly when away from the beam center at 2 µm from pyramid apex. A smooth contiguity of weak signal provides a background for two strong signals, one from tilted planes at the beam footprint and another from untilted strained planes that dominate the interior of the pyramid. As one moves away from the apex of the pyramid, the tilted planes become more and more tilted (causing the diffracted signal to move in χ) and less strained, suggesting this tilting to be a mechanism of 3D relaxation. Note that the untilted signal retains a strong presence throughout, indicating that this planar tilting takes place only at the sidewall facets, perhaps taking place during cooling after growth has completed. The smooth contiguity of the weak signal indicates that this increasing of the tilting and relaxing happens gradually and without grain formation.

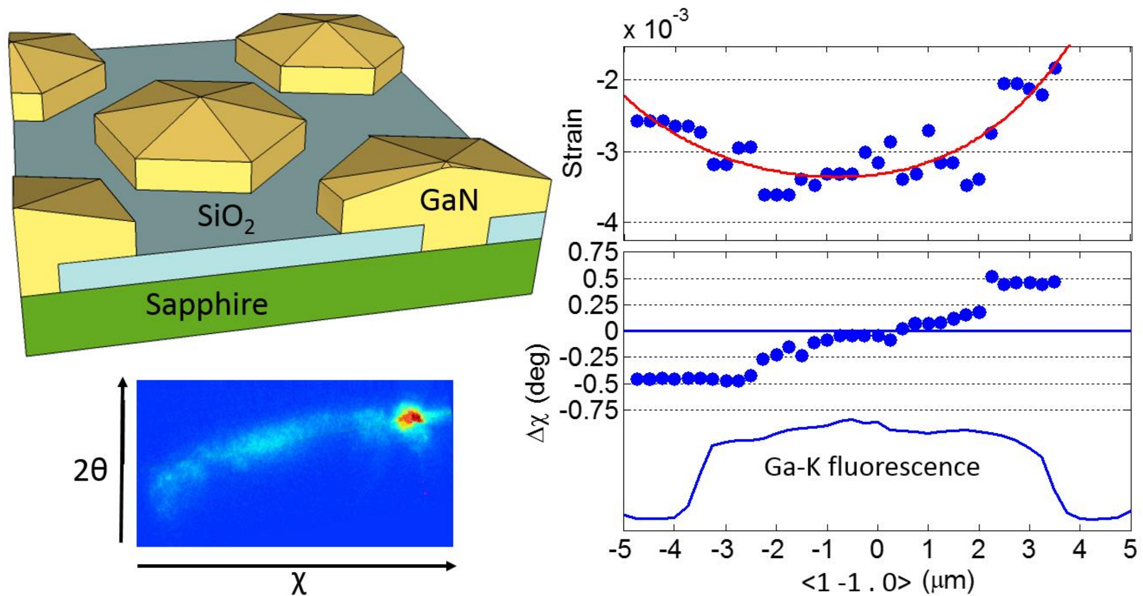

Figure 19. (top left) GaN hexagonal-pyramidal microSAG on Sapphire. (bottom left) CCD image of x-ray diffracted intensity from the (00.4) reflection taken at 2 μm left of center of a GaN pyramid. The tails of the submicron beam partially illuminate the entire left side of the pyramid structure, resulting in additional weak intensity from the rest. The 2 strong signals are from the central beam position at 2 μm left of center and from the uniform interior of the pyramid. The continuity of the weaker signal suggests a gradual tilting of planes as one moves from the center. (right bottom) a plot of the secondary "tilted," which moves in χ as the beam footprint is scanned along the <1 -1 . 0> direction over a pyramid. The Ga-K fluorescence is shown simultaneously to give an understanding of location on the pyramid. At (right top) is the strain shown on the same independent axis. As the tilt becomes more extreme, the tilted planes relax, suggesting that this tilting is a mode of 3D strain release during growth and/or cooling.

The optical efficiency of InGaN/GaN-MQW-based LEDs suffers from piezoelectric fields in the active region. This problem is mitigated on the semi-polar planes, so growing LED structures on the sidewalls of 3D structures like ours improves the spontaneous emission rate [18, 19]. To capitalize on this, we used 3 μm wide mask openings to overgrow 10 μm sided equilateral triangular prisms of n-doped GaN along the <1 1 . 0> direction on GaN-buffered Sapphire [10]. These ridges had <1 -1 . 1> faceted sidewalls. The structures were overgrown on either side of the mask aperture, resulting in about 3 μm of defect-free material on each side. An InGaN/GaN MQW structure was then grown on these ridges at a reduced growth temperature, and the device was capped with a 200 nm p-doped Mg:GaN layer.

Submicron-beam XRD measurements revealed the same planar tilting effect on these structures, even though they were far less strained than the pyramids that were grown on Sapphire. They also tilted at the same rate (0.6 deg/μm from the apex), suggesting that this may be some maximum possible tilting rate without grain formation. Figure 20 illustrates this analysis, with the same tilted signal observed as in the pyramids in Figure 19. This time, the central signal from the GaN buffer layer overpowered the secondary tilt signal for small tilts, making these tilts impossible to measure.

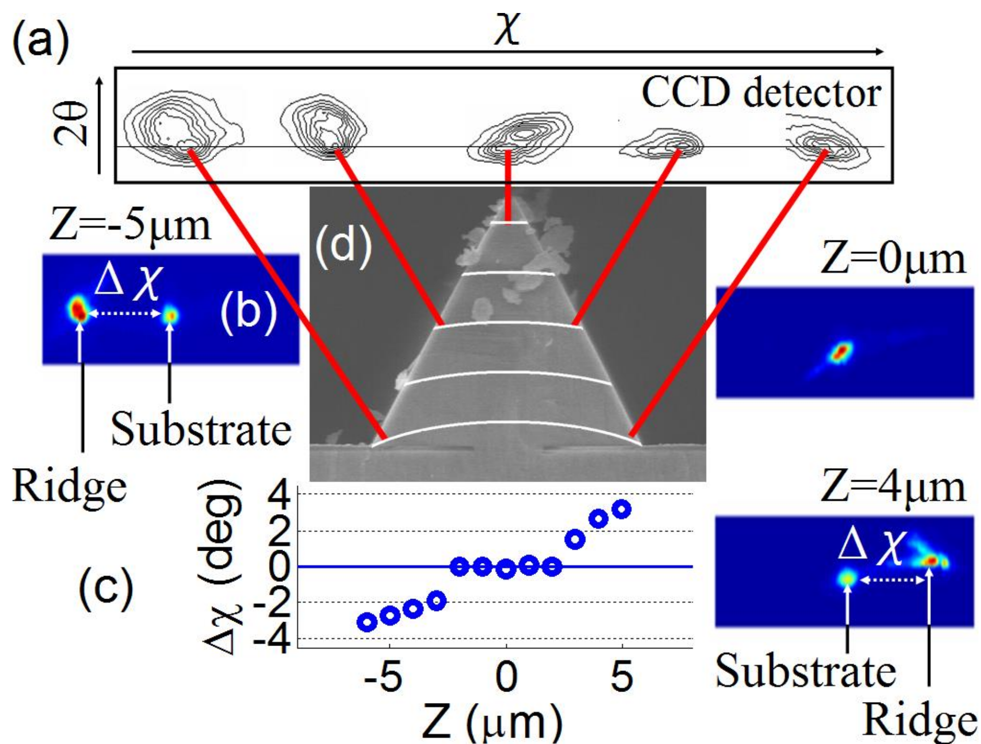

Figure 20. (a) a qualitative illustration of the tilt of the {0 0 . 1} planes observed as an azimuthal shift Δχ of the Bragg (0 0 . 2) reflection on the CCD detector. (b) An example CCD image defines Δχ as the difference in χ between the (0 0 . 2) GaN reflection from the ridge and that from the substrate. (c) Azimuthal shift Δχ as a function of the position Z from the apex of the ridge. Z should be understood to be the <1 -1 . 0> direction. (d) SEM image of the cross-section of a single GaN ridge with InGaN/GaN MQWs grown at the sidewalls (not resolved) with the tilt of horizontal {0 0 . 1} planes shown schematically with white curves. The actual tilting is much less drastic than the white lines suggest. http://dx.doi.org/10.1063/1.2901142

We also looked at reciprocal space maps at different points on the ridge sidewall between the apex and the mask in order to map the strain and period of the MQW structure. The sample was rotated 62 deg in χ and we looked at the (1 -1 . 1) reflection.

Selected maps are shown in Figure 21. The strong signal at the origins is the GaN buffer layer, and the n-type GaN in the ridge is presumed to be in the same location. The 0 peaks are the InGaN layers, and the periodicity of the higher order InGaN-peaks correspond inversely to the period of the MQW structure. Figure 22 shows the trends in calculated strain and period. We find that strain and period both decrease as we move further from the apex. The strain suddenly begins to drop as we reach the ELO portion of the structure. The decrease in strain can be explained by the same 3D strain release mechanism encountered in the pyramids. Unfortunately, this cannot be decoupled from decreased incorporation of Indium near the base, which we did not test for, but is reasonable to assume under the vapor phase diffusion model, since the In-N reaction has a much larger diffusion length than the Ga-N [20], so the base, being closer to the mask, would have a higher Ga/In ratio than the more distant apex. Assuming relaxation and using the formula by Schuster *et al.* [21], we can estimate our In incorporation to be between 30% at the apex and 25% at the base. The decreasing period can be explained by increased growth rate at the apex, which is both cooler than the base and closer to the laterally kinetic precursors.

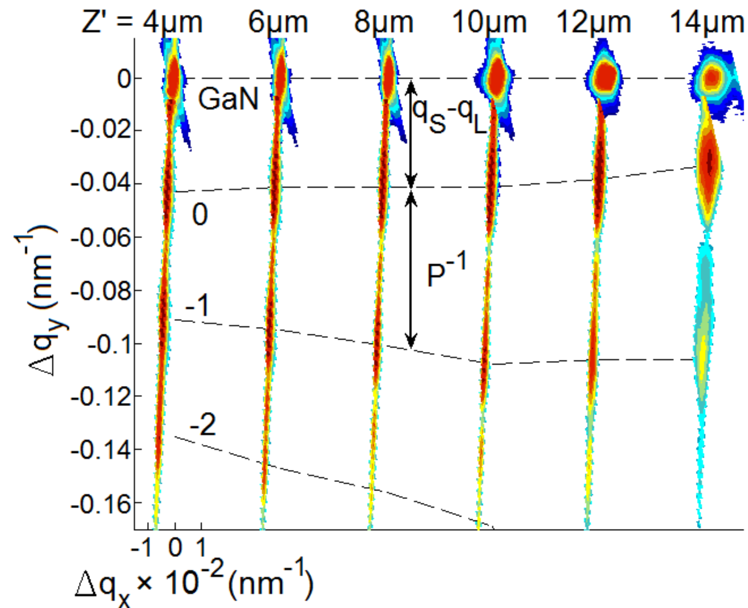

Figure 21. The (1 -1 . 1) reciprocal-space maps measured for selected positions on the ridge sidewall. The distance Z' from the apex of the ridge is shown in microns on the top of the plot. The MQW satellite peaks are marked according to their order. The origin Δqx= Δqy=0 corresponds to the (1 -1. 1) reflection from the substrate. The FWHM of the satellites in qx direction is comparable to the beam divergence (~160 arcsec) of our experimental setup. The larger widths of the GaN substrate peaks are due to color scale saturation. http://dx.doi.org/10.1063/1.2901142

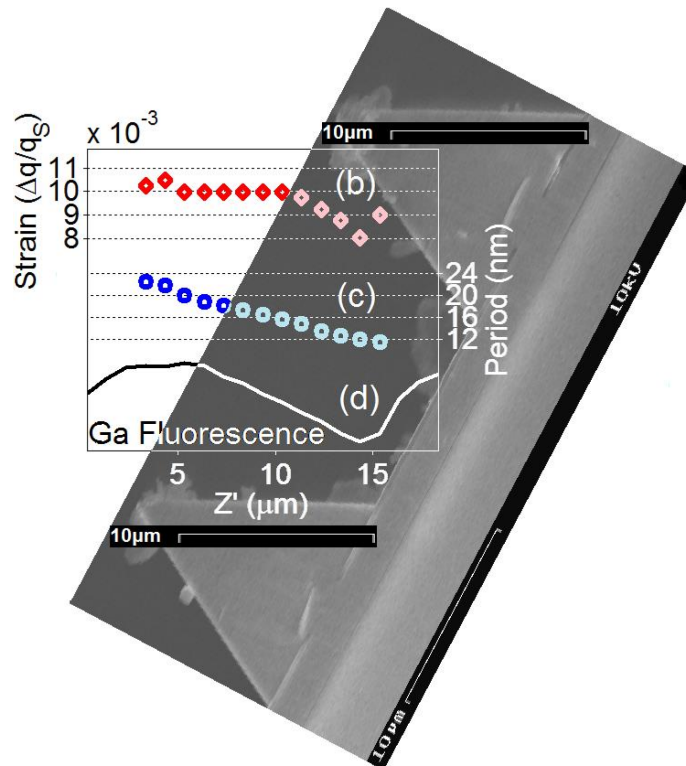

Figure 22. (a) SEM image of the ridge structure. The Strain of the InGaN (b, red diamonds) the period of the MQW (c, blue circles) and the Ga-K fluorescence (d, solid line) profiles are shown as functions of the distance Z' from the apex of the ridge. http://dx.doi.org/10.1063/1.2901142

3.2 GaN NSAG

For our first attempt at NSAG, we applied 10 x 10 μm^2 masks to GaN-buffered Sapphire templates. These masks had 100 nm apertures spaced 600 nm apart (Figure 23). Applying the optimized growth conditions from microSAG instantly gave perfect NSAG selectivity. These growth conditions are: 1000 ˚C, 100 Torr, 4500 V/III molar ratio, and Nitrogen carrier gas. We maintained a low growth rate of 200 nm/hr to avoid parasitic reactions. The results of a 2 hour growth are shown in Figure 24. A uniformity analysis was carried with AFM on 50 nanostructures, and it was found that the average size was 88 nm with a standard deviation of 12 nm. A handful of nanostructures had slightly overgrown the mask.

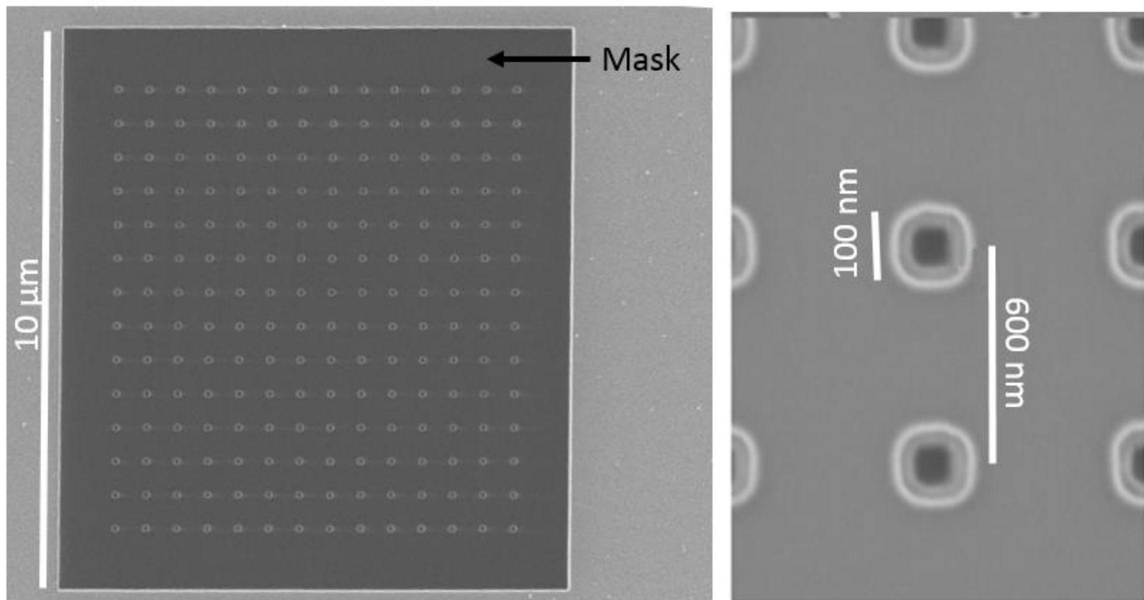

Figure 23. SEM of mask for our very first attempt of NSAG on GaN-buffered Sapphire. (left) overview of the 10x10 µm2 mask area showing all the apertures. (right) zoom on the apertures, which are 100 nm in diameter and spaced 600 nm apart.

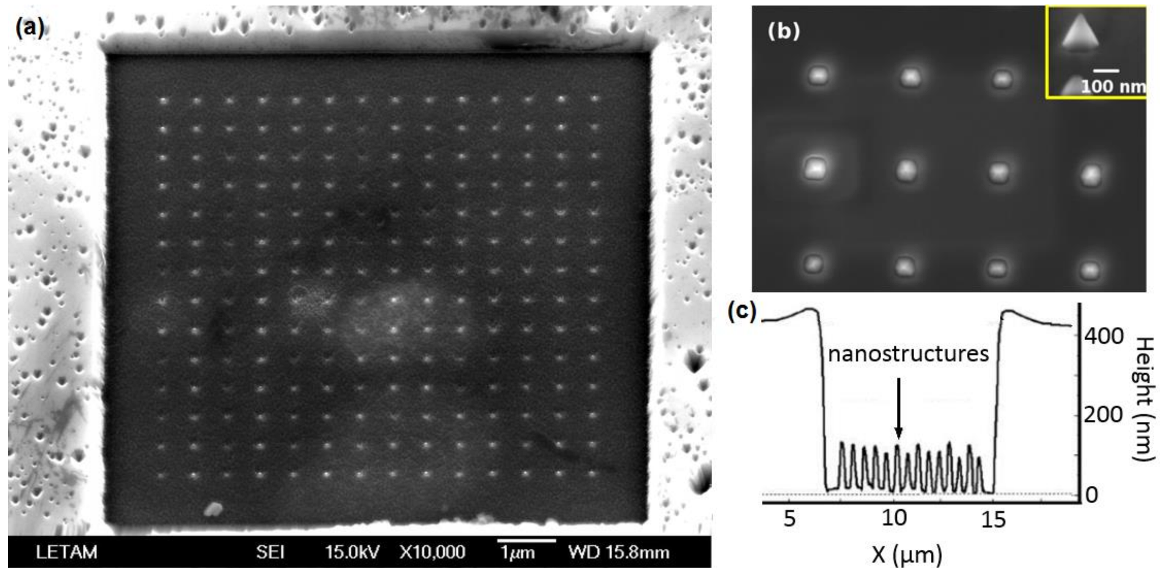

Figure 24. Results of first GaN NSAG on GaN-buffered Sapphire. (a) SEM of the mask area, showing the nanostructures and 2D field with perfect selectivity. (b) Zoom of the nanostructures with inset showing the sideview perspective. (c) AFM scan across the central row of nanostructures, clearly showing the height of the 2D field and each nanostructure.

After this success, we moved onto the mismatched substrates SiC and AlN-buffered-Sapphire. We used the same mask size, but shrunk our apertures down to 80 nm and added two 120x7600 nm^2 stripe-shaped apertures oriented along the <1 1 . 0> direction. Three GaN NSAG samples were grown using the same growth conditions used previously on GaN, except the pressure was raised to 450 Torr on two of the samples (AlN-on-Sapphire and SiC). For comparison, the third sample (SiC) was grown under the original 100 Torr of pressure. A variety of nanocharacterization tools were employed to study the resultant structures and infer what we can about the physics of NSAG. Figure 25 shows SEM/AFM images of the 3 samples, as well as a demonstration of the newly developed submicron-beam XRD technique described early in this dissertation [14]. Note the huge difference in smoothness of morphology between the NSAG structures and the 2D field, indicating that NSAG does in fact lead to improved quality for mismatched substrates. A uniformity analysis was performed on the dots grown on AlN-on-Sapphire, and they were found to be 150 nm with a standard deviation of less than 1 nm. In the SiC

samples, the sizes were less uniform, with standard deviations at over 20% of the average size.

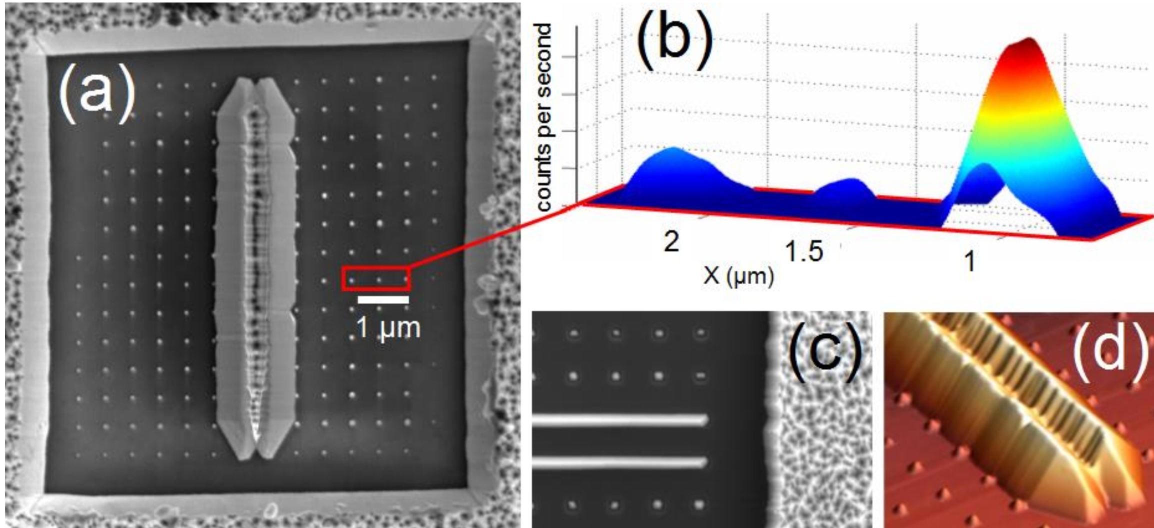

Figure 25. (a) SEM image of sample GaN NSAG on AlN-buffered-Sapphire grown at 450 Torr. (b) X-Y map of the diffracted intensity collected from the nanodots region on the AlN-on-Sapphire sample. Background is subtracted and θ is optimized for the rightmost nanodot. (c) SEM image of GaN NSAG on SiC grown at 100 Torr. (d) AFM image of GaN NSAG on SiC grown at 450 Torr.

A planar tilt analysis was performed on the coalesced GaN ridges on the AlN-on-Sapphire sample (Figure 26). The strong 0-tilt signal (signal 3 in Figure 26) indicates the presence of flat, high-quality GaN that is present throughout the 2-ridge structure. The 4 distinct tilted signals indicate 4 other orientations of the (0 0 . 1) planes. The distribution and discontinuity of these signals suggest the planar arrangement shown by white lines at the top of the figure. Indeed, the discontinuity and outward displacement of the apexes are confirmed by the CL data in Figure 26b. It would appear that during coalescence, the nanoridges begin to grow outwards, probably because tensile elastic relaxation is forced to proceed away from the fixed point of coalescence.

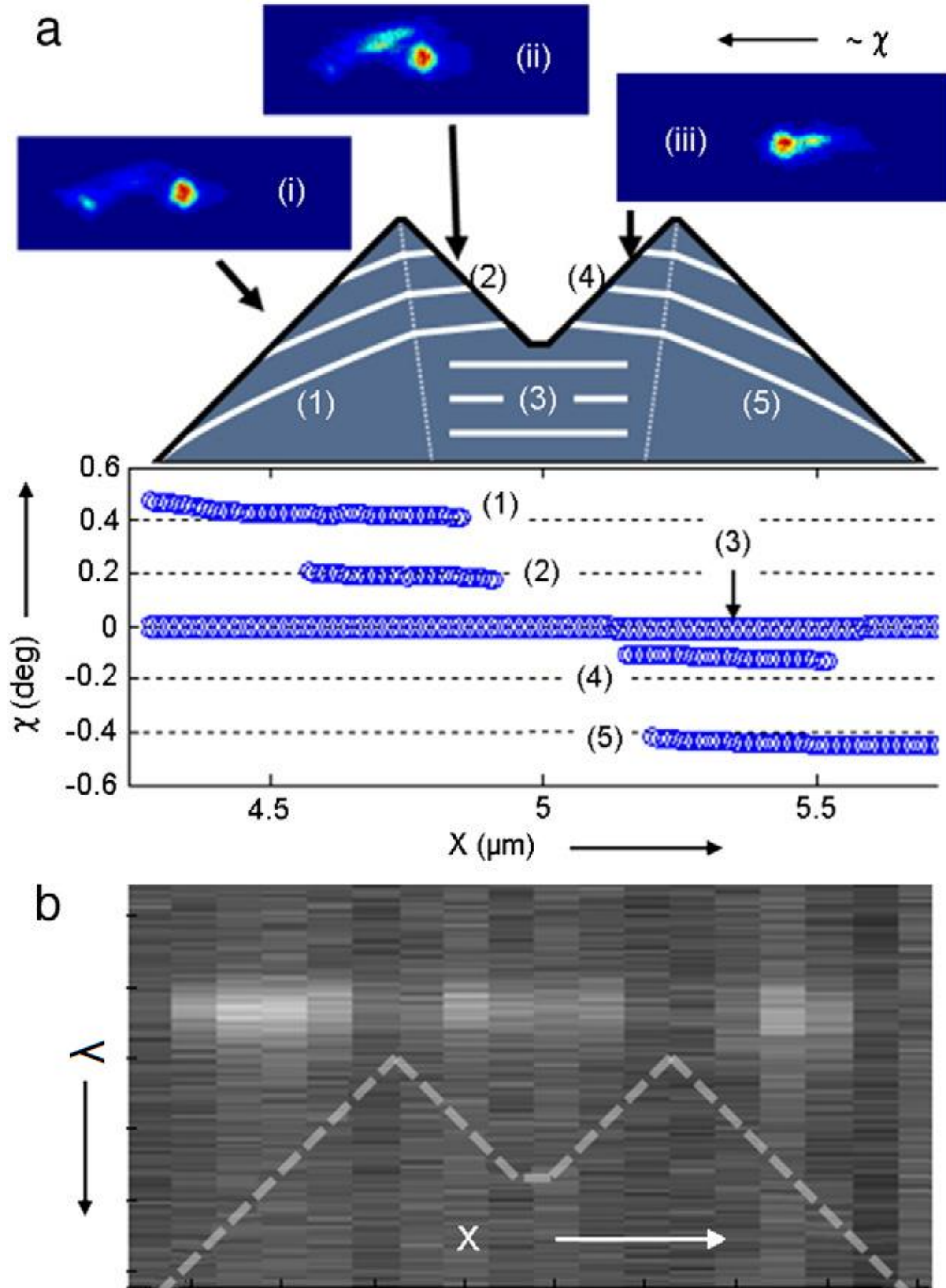

Figure 26. a) diffraction signal χ distribution for different positions across the 2-ridge structure in GaN NSAG on AlN-on-Sapphire. The horizontal axis corresponds approximately to the χ angle and the vertical axis corresponds approximately to the 2θ angle. (i), (ii), and (iii) denote CCD signal images for selected locations, and the Arabic numbering (1)–(5) shows which signals arise from which planar orientations. b) 18 CL spectra, taken simultaneously at different positions across the 2-ridge structure. The X axis is the same as that for a). The dotted line represents the ridge structure profile to make it easier to read (it simply shows the shape of the 2-ridge structure and is not related to wavelength). http://dx.doi.org/10.1016/j.tsf.2012.12.099

The coalesced ridges on the high-pressure SiC sample showed the same phenomenon, and the noncoalesced ridges in the low-pressure SiC sample showed the same 0.6 deg/μm tilting rate as seen in noncoalesced microSAG, further confirming that this is some kind of universal elastic lattice tilting. 3D reciprocal space mapping was performed on all the nanodots and nanoridges for both SiC samples, and the results were averaged. The results are plotted in Figure 27a. The high-pressure NSAG structures were considerably more relaxed than the low-pressure NSAG structures, and SEM images (not shown) suggest that the morphology of the high pressure sample suffers for this. Also, for the high-pressure structures, the dots were considerably more relaxed than the ridges, while there was no significant difference between structures for the low-pressure sample. This suggests that for aggressive growth, the 3D stress relaxation mechanism in dots is more effective at relaxation than the 2D relaxation in ridges. All NSAG structures were high enough quality that the 160 arc second momentum spread of our XRD setup dominated the FWHMs of the signal. Figure 27b shows the 3D reciprocal space map of a point on one of the NSAG ridges on the low-pressure sample. The closer (to the reader) signal originates from the 0-tilt flat planes, and shows a continuous transition through a small strain range (vertical axis). This suggests that the lattice of the low-pressure NSAG ridges are quite affected by the underlying SiC lattice, and have not broken free of it like those in the high-pressure sample have. The more distant and less strained signal is from the tilted planes and moves in χ with distance from the apex. This signal is contiguous with the main signal, but this isn't evident from the 50%-of-max isocline representation.

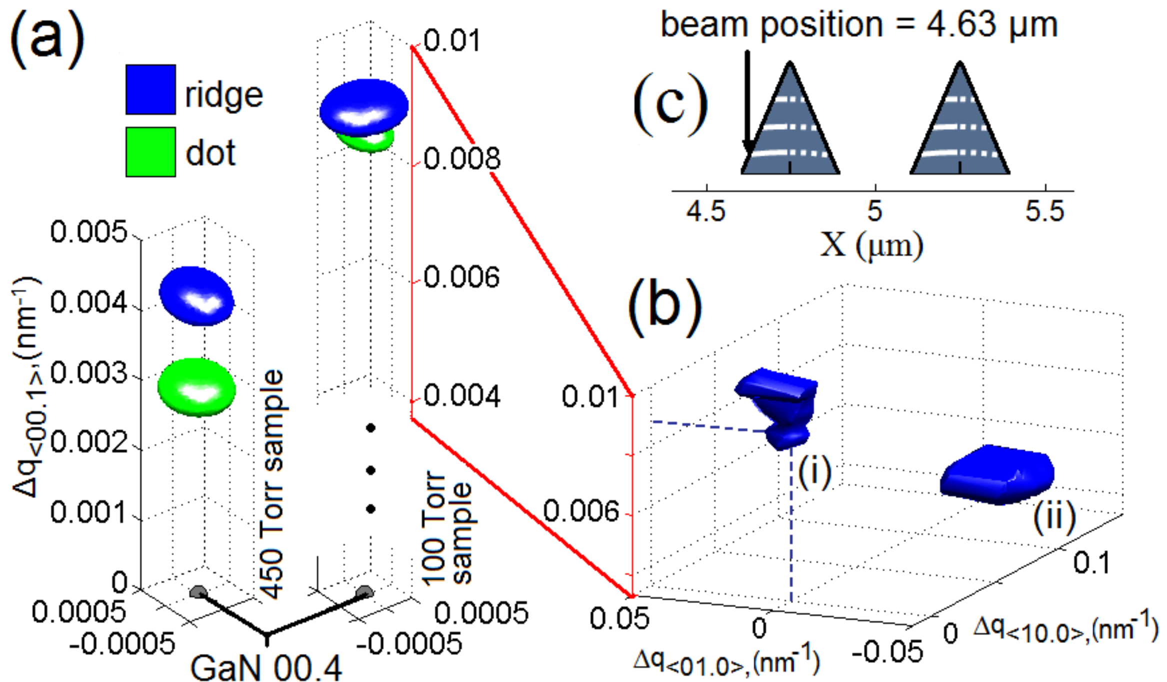

Figure 27. 3D Reciprorcal space mapping of the GaN NSAG under two different pressures on SiC substrates. (a) iso-intensity surfaces at the level of 99.9% of the maximum intensity of the 3D diffracted signal distribution for the NSAG dots (green) and ridges (blue). Data represents an average for signal from all NSAG structures of that type measured per sample. For the ridges, only signal from the untilted planes is considered. The Δq axes are relative to the (00.4) reciprocal lattice point of theoretical bulk GaN. (b) iso-intensity surface at the level of 50% of the maximum intensity of the 3D signal distribution for a position on a ridge of the 100 Torr NSAG. (i) is the main signal from the substrate-aligned (00.1) planes, and (ii) is the secondary signal from the tilted (00.1) planes. (c) position on the ridges where the signal in (b) was collected. http://dx.doi.org/10.1063/1.2901142

STEM images of the SiC samples appear in Figure 28. The left-most image shows clearly a void up the lower middle of the low-pressure ridge. This seems to indicate that two simultaneous growths from either side of the SiC pit under the aperture coalesced at the center. The GaN has a high defect density in the pit, but defect free by the time it peaks up over the mask. This indicates that all nonelastic relaxation takes place lower than the level of the mask surface. The same story appears in the high-pressure sample after it has been subjected to further GaN growth at the same conditions, resulting in a 2D coalescence of the two ridges. There is a void over the mask at the point of coalescence, but the material above and on either side is defect free. Some of the coalescence voids do eventually (after ~500 nm) disappear, especially those between

grains growing in the same aperture, highlighting coalescence of NSAG as a candidate for creating low-defect-density 2D GaN layers.

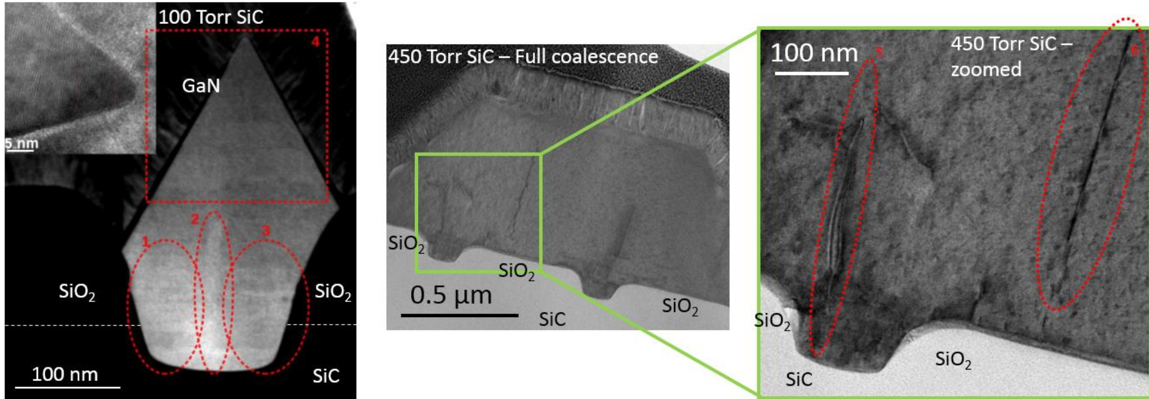

Figure 28. STEM images of the GaN NSAG ridges on SiC substrates. (left) HAADF STEM of the low-pressure SiC sample. The boundary between SiO2 and SiC is determined from a complimentary bright-field image (not shown). The highly defected regions 1 and 3 seem to have originated from either side of the SiC pit, resulting in a void at region 2, where they coalesce. Region 4 is defect free, and is zoomed in to the atomic level at the top left inset. (center) Bright field STEM of the high-pressure SiC sample after more growth time results in total coalescence of the two ridges. Note the highly defected regions analogous to the low-pressure sample. At (right) is a zoomed in portion of the (center) image, showing clearly the coalescence voids both at and just between each aperture. Between and over the voids is defect-free material.

Many GaN nanostructure-based devices use GaN nanostructures as a base upon which to grow ternary layers for device structures such as quantum dot-based laser diodes, nanoribbon HEMTs, or even simply traditionally micron-scale devices on a smaller scale with higher material quality and no nonradiative recombination centers. To study the evolution of the nanostructure surface faceting during growth, we periodically turned on TMAl gas for 1 minute at a time during normal NSAG of GaN [22]. The intention is that the resulting AlGaN layers would show up as markers of the GaN interface during characterization by STEM, showing us how the shape of the interface evolves during growth. These findings could later be directly applied to GaN nanostructures grown on Silicon.

To perform the study the TMAl gas was turned on during growth at minutes 3, 6, 11, 16 and every 15 minutes afterwards. Results for a ridge are shown in Figure 29.

Note the well-defined 2-3 monolayer AlGaN lines that demark the GaN nanoridge facets at the selected minutes. These layers are too thin to speak of a chemical composition, but the AlGaN nanowires that form at the apex were found to be uniformly sized at 2.5 x 6 nm^2 across many structures, and EDX analysis (not shown) indicates an 8% Al incorporation in the nanowires, which is significantly greater than the 5% Al incorporation in the 2D field, even though they're both grown on c-plane GaN.

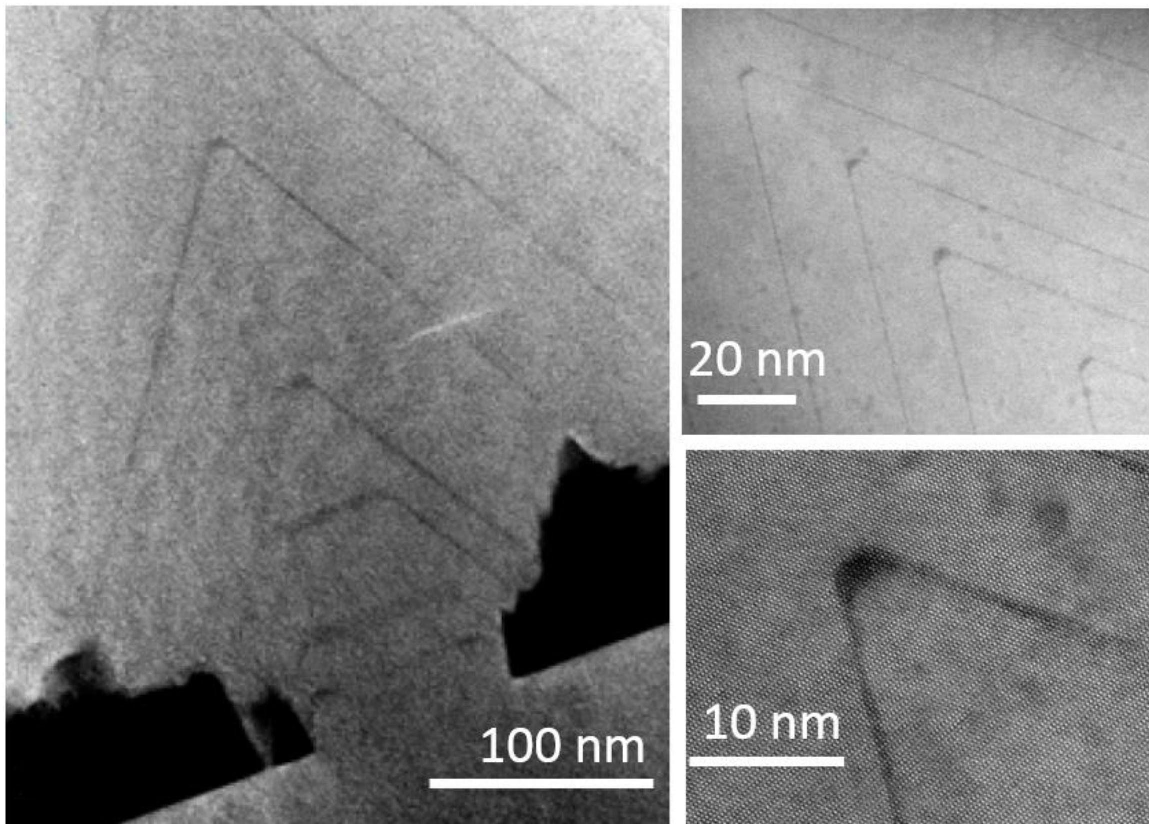

Figure 29. HAADF STEM images of the (1 1 . 0) plane of NSAG GaN nanoridges grown with periodic AlGaN markers grown on a GaN template. (left) Early growth faceting is characterized by a trapezoidal shape characterized by the (1 -1 . 1) and (0 0 . 1) planes. With increased thickness (right top), the growth becomes characterized entirely by the (1 -1 . 1) planes. (right bottom) Aluminum incorporation is significantly enhanced at the apex, resulting in AlGaN nanowires through the structure. In the nanopyramids (not shown), AlGaN nanodots form at the pyrimdal apexes. http://dx.doi.org/10.1016/j.tsf.2012.12.099

GaN growth begins trapezoidally, with the semipolar (1 -1 . 1) facet present, but not as strongly as the c-plane. With time, the semipolar planes begin to dominate the shape. At every step, the interface is smooth and sharp. This is all very good news, since

we can effectively select whether we want a c-plane-based device, e.g., for an AlGaN/GaN nanoribbon HEMT, or a semipolar-plane-based device, e.g., for an InGaN/GaN optical device.

3.3 InGaN/GaN NSAG

Having sufficiently mastered NSAG of GaN, we sought to use this technology in nanoscale heterostructures with InGaN, which has obvious optical [23] and solar-power [24] applications, and is fraught with strain-related issues [25, 26], even on GaN substrates. Two different InGaN/GaN structures were grown on GaN templates. The first was an InGaN/GaN MQW structure on nanoridges, and the second was InGaN nanopyramids/nanoridges grown on 20 nm NSAG GaN seed dots/strips.

An all-stripe mask pattern was used to grow InGaN/GaN MQW structures on the (1 -1 . 1) sidewall of NSAG GaN nanoridges on a GaN-buffered-Sapphire template [27]. The growth temperature was lowered from 1000 ˚C to 800 ˚C when growing the 5 InGaN layers. Results appear in Figure 30. It's directly apparent that the (1 -1 . 1) facet is lost at the apex of the NSAG GaN nanoridge. That this did not occur during the AlGaN marker experiment suggests that it is caused by InGaN growth conditions. There is enhanced Indium incorporation at the point where the (1 -1 . 1) plane gives way to steeper facets, creating quantum wires along the NSAG GAN. These wires have almost twice as much Indium as the MQW wells. This strange phenomenon occurred in every structure measured, and Figure 30d shows a very high uniformity in both shape and orientation, with apparent variations in diffracted intensity being explainable by beats due to frequency addition with our sampling frequency. This stands in stark contrast to the AlGaN nanostructures discussed earlier.

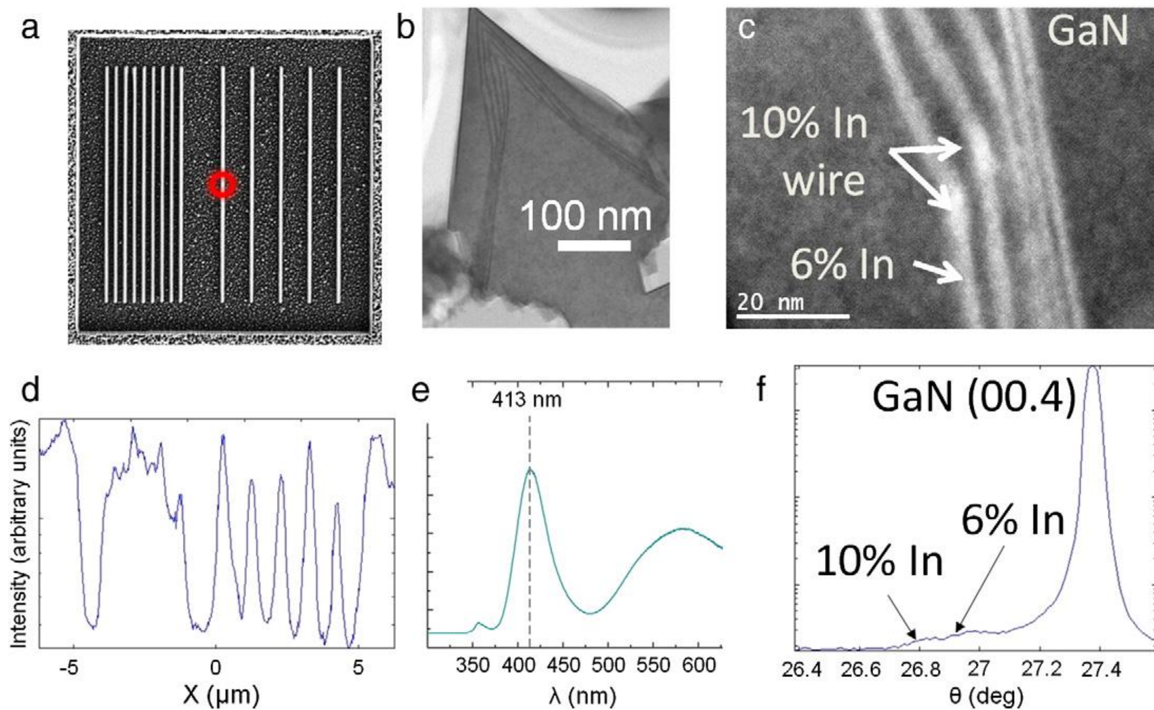

Figure 30. InGaN/GaN MQW on NSAG GaN on GaN-buffered-Sapphire. a) SEM image taken of the 10×10 µm2 mask region showing the layout of the nanoridges. The red circle indicates the "central ridge" where data was taken for b, c, e, and f. b) Bright field STEM image of the central ridge showing the MQW structure. c) HAADF STEM image of the area shown in subpanel b with labels indicating EDX chemical analysis results measuring indium concentrations. Two indium-rich nanowires are indicated by "10% In wire." d) Diffraction intensity taken by scanning across the 10 µm mask region in the direction perpendicular to the nanoridges at Bragg conditions optimized for In0.06Ga0.94N. The X axis corresponds exactly to the SEM image in subpanel a above. e) CL spectrum taken at the central ridge. f) XRD θ–2θ scan performed on the central ridge, clearly showing the two InGaN signals and the GaN signal. http://dx.doi.org/10.1016/j.tsf.2012.12.099

CL results give a strong emission of 413 nm light, which corresponds to the 10% InN quantum wires. The broad yellow peak is due to surface defects [28]. The InGaN peak is more than twice as intense as the emission from the MQW structure of the 2D field (not shown), which is very impressive considering the small size of the InGaN quantum wires. The difference can be explained by lack of threading dislocations (and therefore lack of nonradiative recombination points) in the nanostructures.

In a second experiment, pure InGaN (not MQW-structured) nanopyramids and nanoridges were grown on NSAG GaN nanodots and nanostrips [7]. The objective was to use the 3D strain-relief mechanism to overcome phase separation [29], impediment of InN incorporation due to compressive strain [30], and polarization fields due to strain

gradients [31]. This is of course in addition to the reduced defect density expected from NSAG, and the enhanced InN incorporation in semi-polar growth, which we can optimize growth conditions to produce. Additionally, since the InGaN nanostructures are to be grown on NSAG GaN nanostructures, we can apply exactly the same technique to GaN nanostructures NSAG on any other substrate.

Growth was carried out through 100-nm dot and stripe-apertured masks. 20 nm of NSAG GaN was produced using our usual conditions. This growth terminated in a c-plane, as shown by the lower markers in Figure 29, and these c-plane nanostructures served as interfaces for subsequent NSAG InGaN under the same growth conditions as for the InGaN layers in the previous MQW experiment. The InGaN growth resulted in very regular (1 -1 . 2)-faceted hexagonal nanopyramids and irregularly r-faceted nanoridges, as shown in Figure 31. Even though there is some inhomogeneity

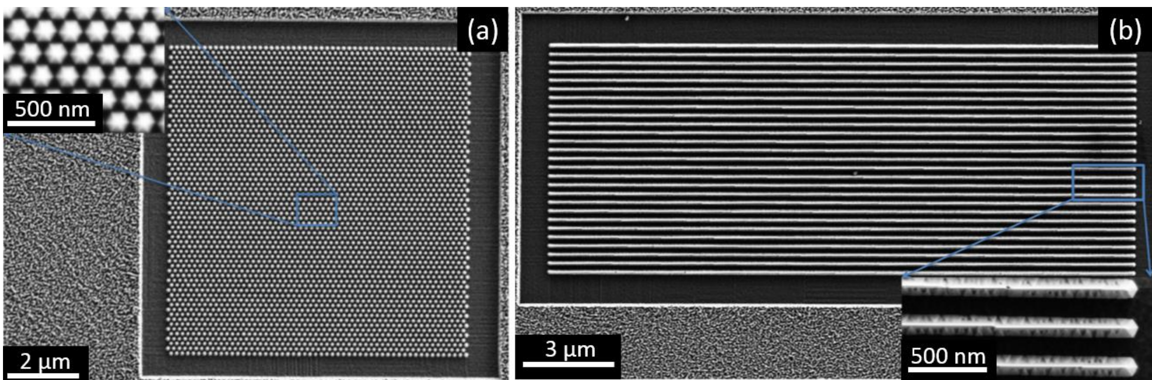

Figure 31. SEM of InGaN nanopyramids (a) and nanoridges (b) on 20 nm of NSAG GaN on a GaN/Sapphire template. http://dx.doi.org/10.1063/1.4900531

in the sidewall morphology of InGaN nanoridges, both nanostructure types are smooth, indicating that the 3D strain mechanism is in effect. Compare this to the morphology in the unmasked field (Figure 32 inset), where V-defects and trench pits dominate.

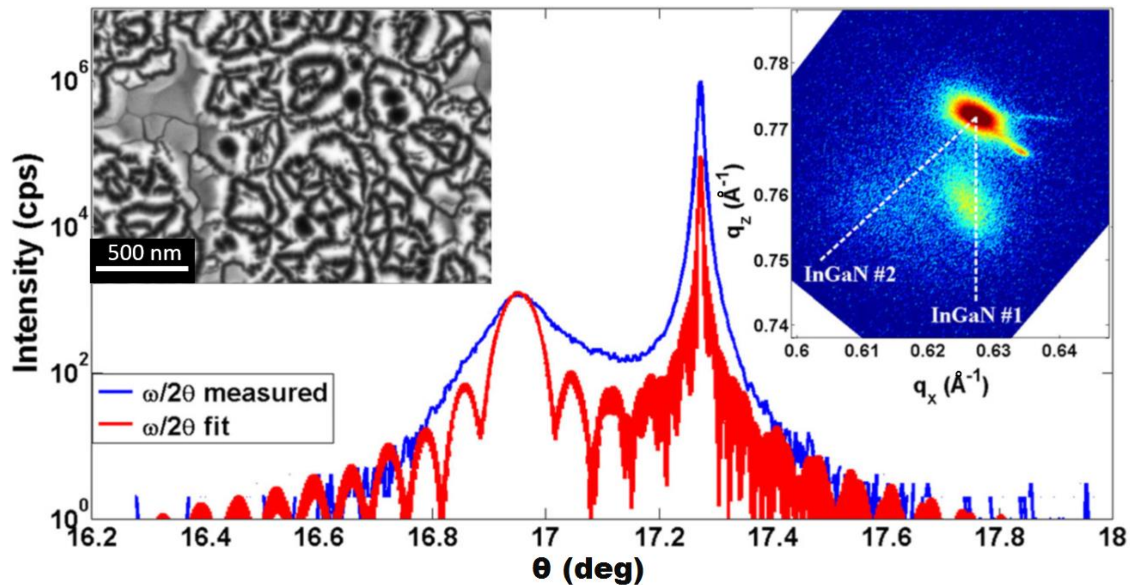

Figure 32. XRD of the (00.2) reflection of the 2D InGaN field on GaN/Sapphire template. Left inset is an SEM image of the surface. Right inset is a reciprocal space map of the (11.4) reflection. http://dx.doi.org/10.1063/1.4900531

Featured in Figure 32 is an ω-2θ scan of the (00.4) reflection of the InGaN in the unmasked field region. The low-angle peak corresponds to an InN incorporation of around 12% (The higher angle peak corresponds to GaN). In the right inset is a reciprocal space map of the (11.4) reflection showing two InGaN peaks, corresponding to a highly strained (InGaN #1 – 12% InN) and fully relaxed (InGaN #2 – 23% InN) InGaN lattices. The two distinct peaks indicates that there are two distinct phases rather than a continuous transition between the strained and relaxed phases. The abrupt relaxation happens either after a critical thickness or in phase grains dispersed throughout the growth, with the In-rich phase occurring where growth was semi-polar.

STEM, XRD and EDX analyses were performed on the nanopyramids. Four different magnifications of STEM are shown in Figure 33a-d. The shape uniformity is striking, and it's clear that the material is absent of threading dislocations. The interface between the nanopyramid and the 20 nm of NSAG GaN is clear in Figure 33c. Figure 33e is a ω×2θ mapping around the (00.4) reflection of both the nanopyramids and field growth using synchrotron-based XRD analysis (aside: Our synchrotron-based submicron-

beam XRD setup [14] is capable of analyzing individual nanostructures, but on this day, the beam was wandering, and beam time being precious, we were forced to make do.). The signal due to the field was isolated in a separate field-only mapping (not shown), so we were able to determine which signal is due to the field and which is due to the nanopyramids. The signal width for each is a product of orientation spread either within the material or in the case of the nanopyramids, between the individual nanostructures. Compared to the field growth, the nanopyramids show a slightly enhanced InN incorporation, and this is corroborated by the EDX analysis in Figure 34, wherein the InN composition is shown to vary with distance from the GaN interface, topping out at around 26% InN. Laterally, we see a dip in composition at the central vertical axis, likely due not to a low-InN lattice, but rather to the same graining effect seen in the nanoridges (see Figure 35). This also explains the low InN content along the top part of the vertical profile (LG1 in Figure 34), which is not reflected in the XRD.

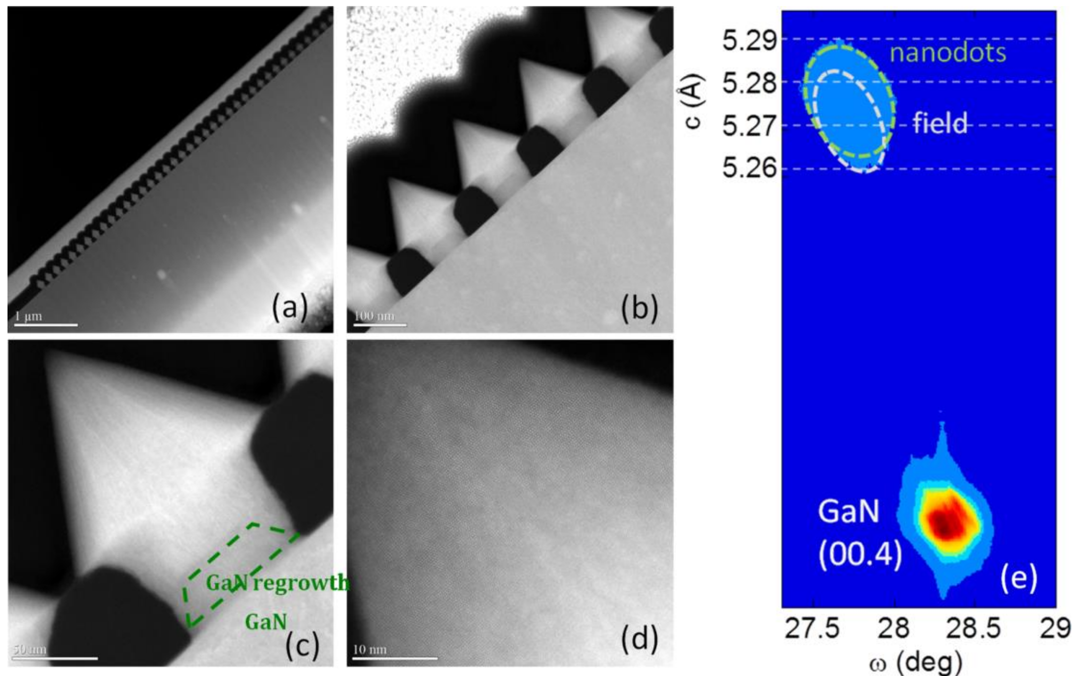

Figure 33. NSAG InGaN nanopyramids on 20 nm of NSAG GaN on GaN/Sapphire template. (a)-(d) shows different magnifications of STEM, with (c) indicating the 20 nm of NSAG GaN. (e) ωx2θ XRD map around the (00.4) reflection, containing signal from both the nanopyramids and field growth. The field growth signal was isolated by a subsequent mapping of the field without the dots (not shown). The 2θ axis has been converted to crystal parameter c. http://dx.doi.org/10.1063/1.4900531

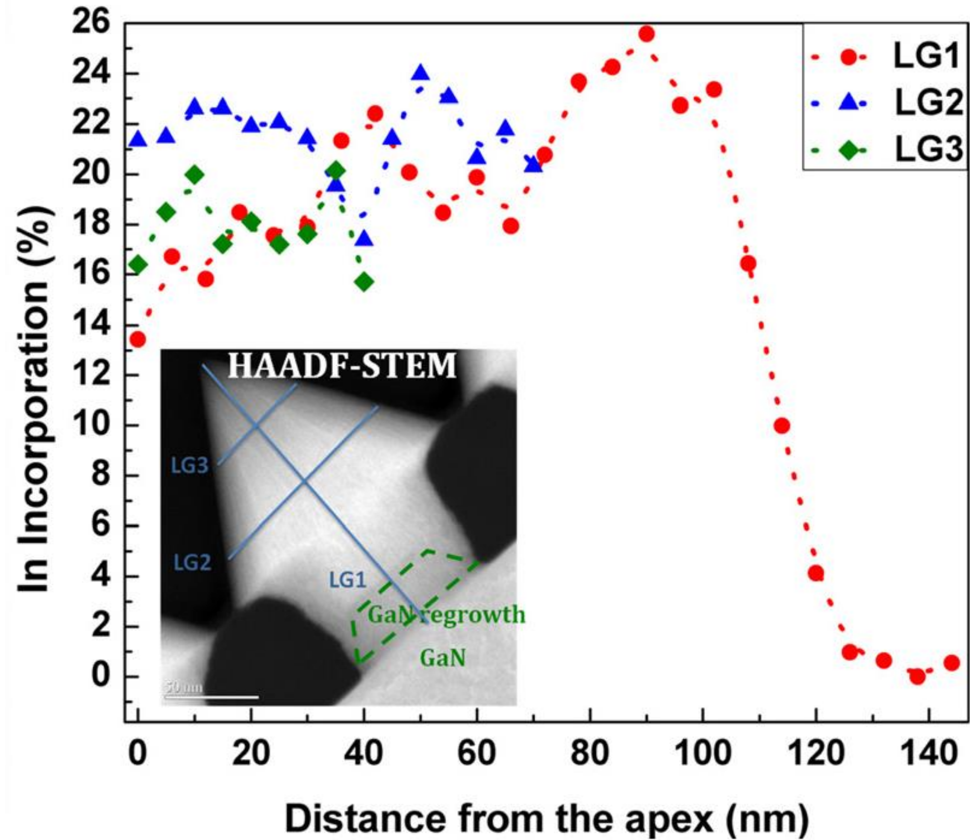

Figure 34. 3 different EDX profiles of an InGaN nanopyramid. The Geeen and Blue plots are lateral profiles, and the Red plot is along the c-plane. http://dx.doi.org/10.1063/1.4900531

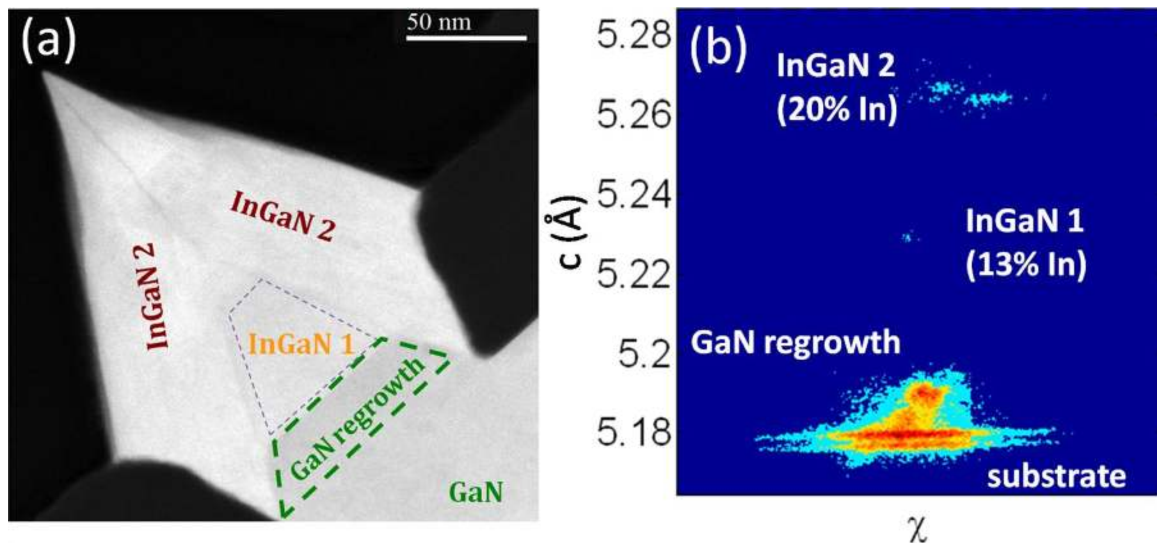

Figure 35. InGaN nanoridge on GaN/Sapphire template. (a) STEM showing the 3 phases of InGaN growth. (b) $\chi \times 2\theta$ map of the (00.4) reflection of the nanoridge by synchrotron-based submicron-beam XRD. http://dx.doi.org/10.1063/1.4900531

The STEM and sub-micron beam XRD analysis of the nanoridges in Figure 35 shows a strikingly clean and symmetric graining effect. The interfaces between the three InGaN grains and the GaN growth are very clearly visible in the STEM image of Figure 35a. The CCD diffraction capture in (b) shows distinct signal for each grain observed, including the two different phases of GaN (template and 20 nm NSAG). The high-In phase has two peaks distinct in χ, which is consistent with two independently grown grains of the same material phase. The InN incorporations were calculated using the methods of Schuster et al. [21], and were confirmed by EDX (not shown). Note that we observe the same change in termination plane as in the InGaN/GaN MQW nanoridge in Figure 30, even though InGaN growth here takes place at constant growth conditions. That suggests that this effect is characteristic of InGaN NSAG by MOVPE in general.

Optical characterization by CL is shown in Figure 36. Low-temperature (77 K) CL was performed with beam energies of 3, 5 and 7 keV, corresponding to maximum energy loss depths of 25, 55, and 120 nm, respectively. Thus, the 3 keV beam energy (red) activates primarily the top, In-rich grain for the nanostructures, in agreement with our STEM/EDX results. Higher beam energies in the planar InGaN reveal two distinct luminescence peaks centered at 420 nm and 520 nm, corresponding to 12% and 21% InN, respectively, according to the work of Orsal *et al*. [32] We observe a higher proportion of In-rich (InGaN 2) signal compared with In-poor (InGaN 1) signal in shallower measurements, suggesting that the In-rich phase occurs after some critical thickness, likely due to relaxation [26, 33]. The broad band at 590 nm is interpreted as the GaN defect band. In the nanostripe, bands from the two different InGaN phases are present, centered at 464 nm and 525 nm (14% and 21% InN), and we note that probing increasing depths enhances the In-poor phase, corroborating the phase grain arrangement found by STEM. The nanopyramid shows only the In-rich phase, in agreement with our XRD and STEM/EDX results.

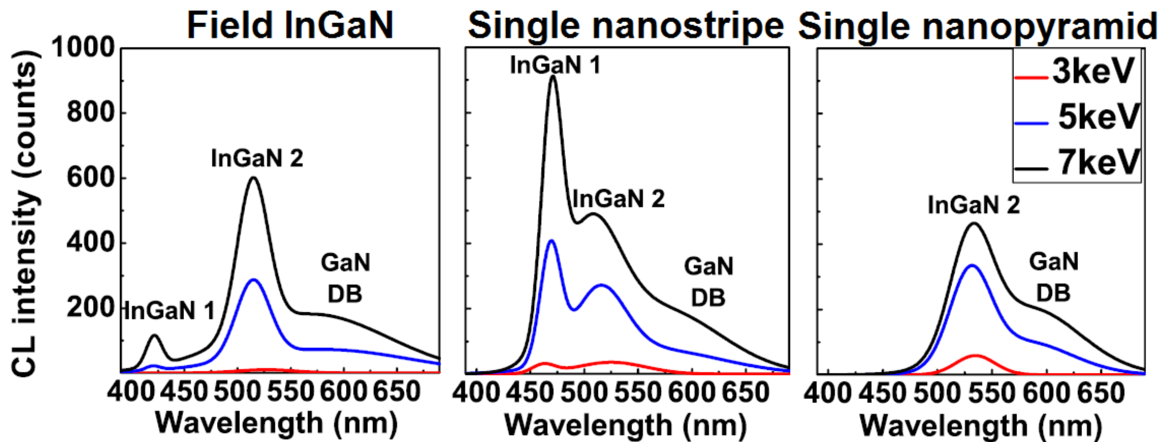

Figure 36. 77K CL at 3 different voltages of InGaN planar and NSAG growth on GaN/Sapphire template. The wide peaks labeled GaN DB are interpreted to arise from the GaN defect band. http://dx.doi.org/10.1063/1.4900531

To prove the usefulness of this new technology for devices, we used it to grow a PIN heterojunction solar cell [34]. 150 nm-thick $In_{0.09}Ga_{0.91}N$ nanopyramid arrays were grown by NSAG on an n-GaN-on-Sapphire template. After CL characterization of the InGaN nanopyramids and planar regions, they were completely covered with a Mg-doped p-GaN layer with a hole concentration of around 2×10^{17}. The SiO_2-masked area was then etched away in 5% hydrofluoric acid to expose the n-GaN layer, and then 3 different PIN structures were contacted: 2 nanopyramid-based PINs and 1 planar PIN. Contacting was achieved with tungsten probes.

The CL results (not shown) were as expected according to the previous experiment. The NSAG growth had enhanced InN composition (9%) compared to the planar region (7%), and contained a secondary, In-rich phase. Figure 37 shows the I-V characteristics of the three contacted PIN structures. We note clear rectifying behavior in all cases, and ideality factors around 4-5, as in other reported InGaN core shell solar cells [35]. We note that our NSAG-based PINs produce current 3 orders of magnitude greater than do planar PINs, and that the IV ratio at ±1 V is 20 times greater, which is an unambiguous display of the usefulness of NSAG in GaN/InGaN/GaN PIN solar cells.

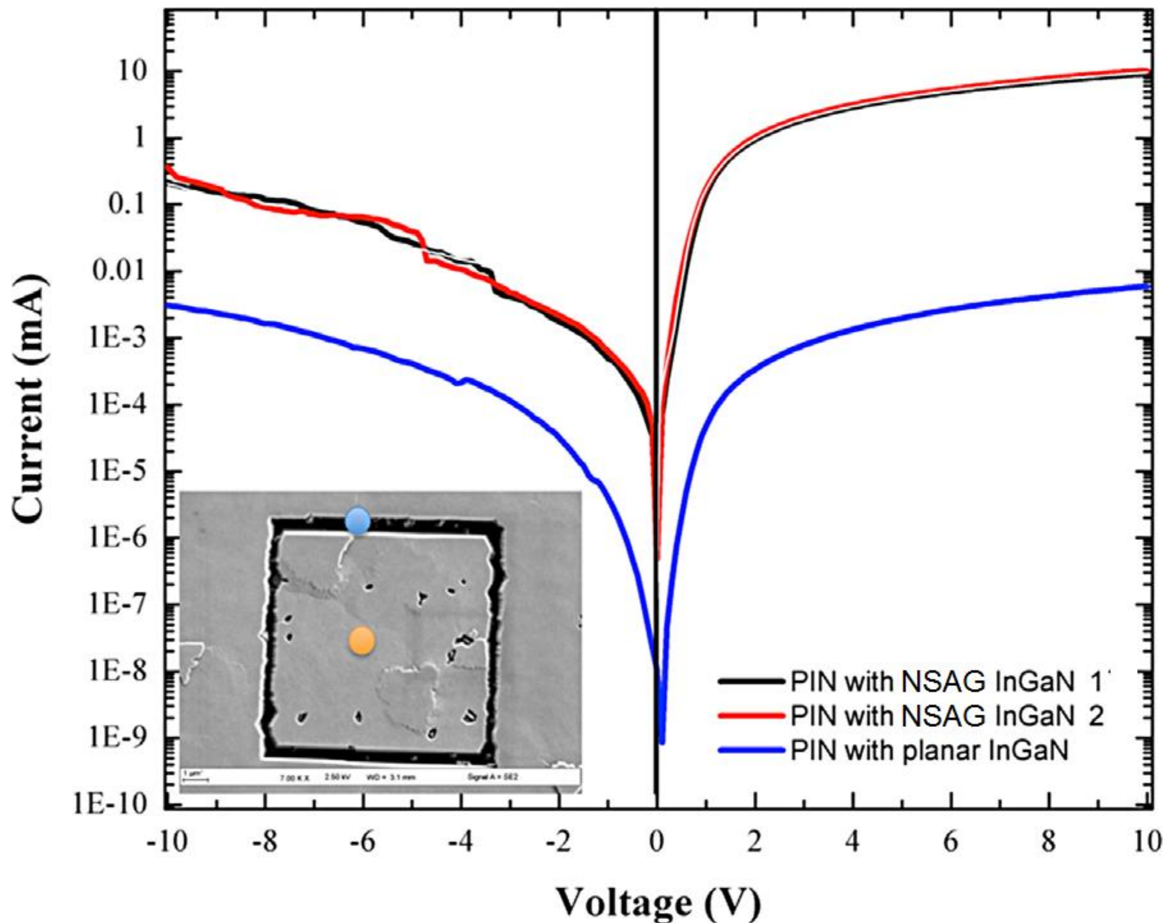

Figure 37. I-V analysis of the three contacted PIN structures. The inset shows an SEM image of one of the nanopyramid-based PINs, with the orange and blue dots representing tungston probe positions for contacting the p and n layers, respectively (The SEM image was taken before HF etching). http://dx.doi.org/10.1002/pssa.201400278

3.4 AlGaN NSAG

A new stripe-only mask pattern was used to study NSAG of AlGaN on a GaN template (Figure 38a) [27]. To that end, we aimed to examine the growth evolution of our NSAG GaN in order learn how to optimize the GaN facet interfaces [22].

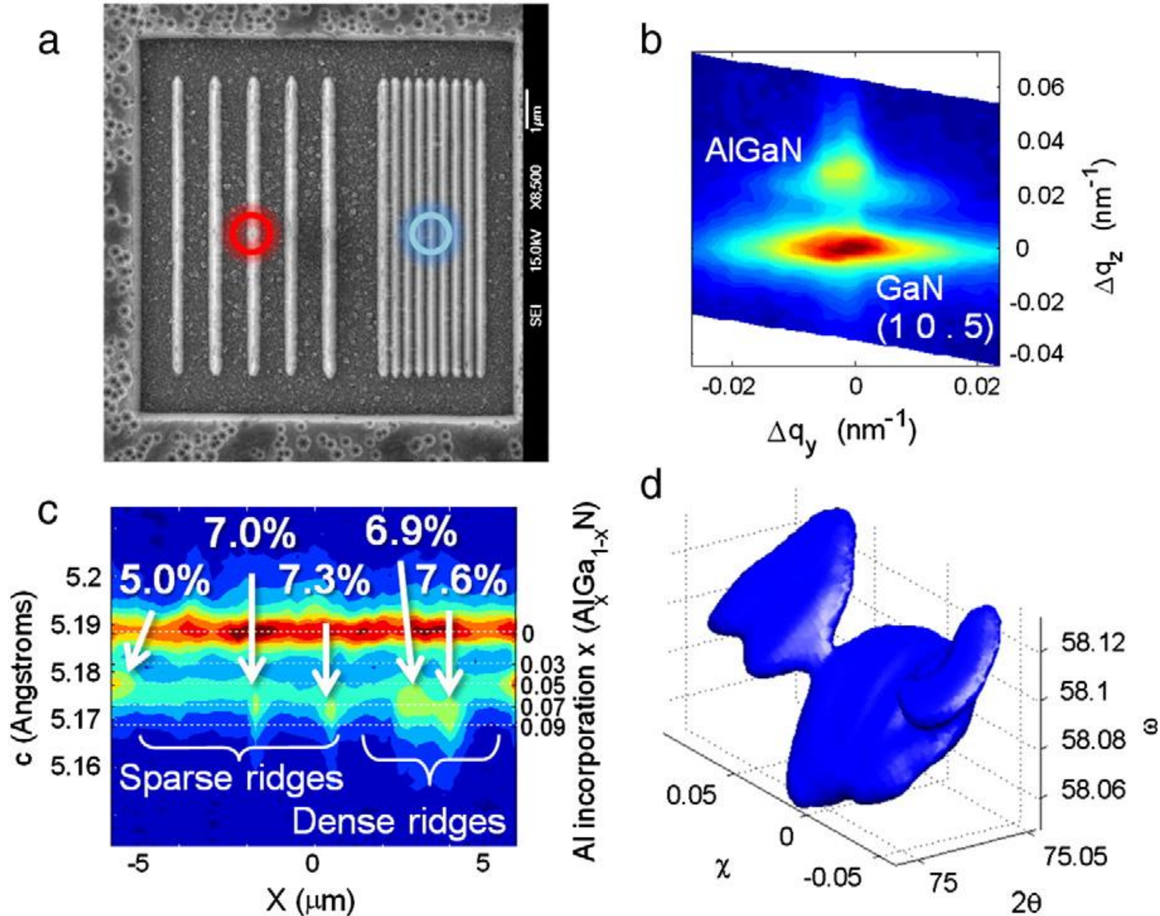

Figure 38. Results of NSAG of AlGaN on a GaN-on-Sapphire template. a) SEM image taken of the 10×10 µm2 mask region in the AlGaN nanoridge sample, showing the layout of the nanoridges. The red circle indicates the location where the data was taken for b and the blue circle indicates the location where the data was taken for d. b) 2D reciprocal space map of the (1 0 . 5) reflection, taken at the location denoted by the red circle in subpanel a. c) X-scan of diffracted intensity measured with a single channel detector for the (0 0 . 6) reflection across the center of the 10×10 µm2 mask area in the direction perpendicular to the nanoridges. The Y axes are lattice parameter (left) and aluminum incorporation (right). Aluminum composition %s corresponding to some signals are noted. d) 3D angle space map of 3 different ridges, represented by a 75% isointensity surface of diffracted intensity at the (10.5) reflection. The central signal is strongest because it originates from the ridge under the strongest central part of our X-ray beam, which was centered at the position denoted by the blue circle in subpanel a. http://dx.doi.org/10.1016/j.tsf.2012.12.099

In this mask pattern, some stripes were arranged densely (Period = 300 nm), and some were arranged sparsely (Period = 1 µm). The growth conditions were the optimized ones we found for GaN NSAG, except with the addition of TMAl. The AlGaN NSAG was not selective (there were polycrystalline deposits on the mask), but still formed well-faceted nanoridge structures. Submicron-beam XRD results shown that the AlGaN nanoridges were all elastically strained, while the field (not shown) was fully relaxed. No

difference was found between the (rather low) Aluminum incorporation between the sparsely and densely arranged nanoridges, but the NSAG was found to have significantly more incorporation than the 2D field. 3D diffraction angle space mapping showed that the lattices of each nanoridge, while showing a good individual quality and uniformity, were oriented independently from each other, even though they all grew from the same substrate. Figure 38d shows diffracted intensity from 3 densely arranged AlGaN nanoridges. Each disk shape originates from one of the structures, and differ in both strain (interpreted as Aluminum incorporation) and orientation.

3.5 Coalesced NSAG microtemplates

An application of NSAG briefly mentioned in section 3.2 is the fabrication of microtemplates by using ELO to coalesce NSAG nanostructures to form a smooth 2D layer that can then be used as a template upon which to grow a device. Threading dislocations originating from the original substrate will not pass the mask, so the density of such dislocations is reduced by a factor at least as large as the ratio of the area of the mask to that of the apertures. Additionally, in the case of mismatched substrates, the microtemplate layer is allowed to elastically release much of its strain during early NSAG and ELO (before coalescence), resulting in a higher quality material than can be expected for normal 2D growth. Additionally, NSAG through apertures smaller than the average grain size of the substrate will result in a microtemplate with regularly spaced grains, bounded by planes of coalescence.

For this study, a GaN-buffered Sapphire substrate was masked with densely spaced stripe-shaped nanoapertures along the <1 -1 . 0> direction, through which triangular prism-shaped GaN nanostripes where grown by NSAG using the same growth conditions as in previous sections. Figure 39a shows this early stage of fabrication. The ambient gas is then changed from Nitrogen to Hydrogen for ELO until coalescence

(Figure 39b). A functional layer of 20 nm InGaN is then grown on top to simulate an active region.

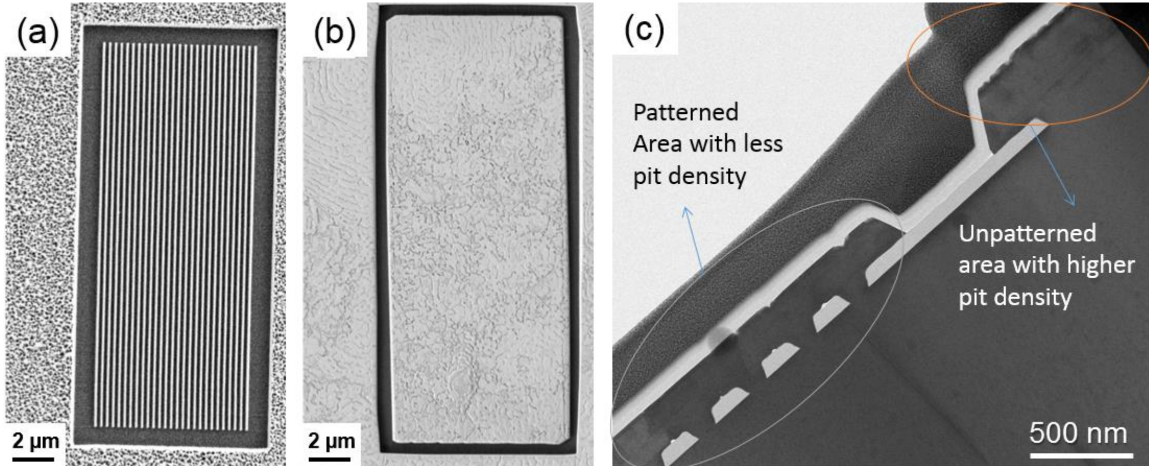

Figure 39. InGaN on NSAG GaN microtemplate. (a) SEM image of NSAG GaN nanoridges before ELO. (b) InGaN grown on NSAG GaN microtemplate formed by applying ELO and coalescence to the structure in (a). (c) HAADF-STEM image of the (1 1 . 0) plane showing InGaN growth on both the NSAG microtemplate (left) and the 2D field (right). The inset is in the bright-field mode for a clearer view of the InGaN/GaN interface.

The reader is referred to Ref. [36] for analysis of the InGaN layer, but for the purposes of the current work, the figure of merit is the STEM image in Figure 39c, which shows a cross-section of both the field and microtemplate regions. The most striking difference is the density of v-defects, which is more than an order of magnitude less in the microtemplate region. This is because grain boundaries are present only at the points of coalescence and occasionally also over the nucleation site, making them not only less in number but in a somewhat predictable arrangement. We also see a few instances of grain boundaries becoming deleted before the surface.

CHAPTER 4

SELECTIVE AREA GROWTH ON SILICON

After achieving a deep competence in SAG on traditional, high-cost substrates, we are ready to apply our research cycle, characterization expertise and extensive experience to tackling the problem of Group III-Nitride SAG on Silicon substrates. The first section of this chapter will detail our early work on bare Silicon. The second will present our results on AlN-buffered-Si(111) templates and compare these results to those we achieved earlier on GaN-buffered-Sapphire, AlN-buffered-Sapphire, and SiC. For a review of the state of the art of techniques for improving the quality of GaN layers and/or nanostructures on Silicon substrates, the reader may refer to the following references on AlN nucleation layers [37-40], Silicon islands/pillars [41, 42], patterned Silicon [43], MBE NSAG [44], MBE nanocolumn coalescence [45], and intermittent quantum dot layers [46].

4.1 Early work on bare Silicon

Before beginning growth on Silicon, we must take steps to remove contaminants and the monolayers of native oxide. We prepared Silicon wafers for processing using the following steps:

1. Ultrasonic ethanol bath (5 minutes)
2. Boiling acetone bath to remove the majority of molecular contamination (5 minutes)
3. Second ultrasonic ethanol bath to remove all acetone (5 minutes)
4. Deionized water rinse
5. Drying in pure Nitrogen
6. Sulfuric acid (3:1:1 H_2SO_4:H_2O_2:H_2O) bath at 100 ˚C to remove organic contaminants (5 minutes)

7. Deionized water rinse

8. Drying in pure Nitrogen

9. hydrofluoric acid (2.5%) bath to remove atomic contaminants and the native oxide monolayers

10. Deionized water rinse

11. Drying in pure Nitrogen

The last 3 steps are repeated until step 10 results in visible beading on substrate surface. This indicates that the surface has become hydrophobic and so the oxide monolayer is gone.

To assure selectivity, we used growth conditions identical to those for more expensive substrates. The only change was that we aimed to minimize initial Si-N reactions on the Silicon surface by withholding ammonia until after the temperature is maxed out at 1000 ˚C. Figure 40 shows SEM images of the results of GaN microSAG on bare Silicon (111). We achieved perfect selectivity along with the horrendous polycrystalline 2D growth expected of GaN growth directly on Silicon.

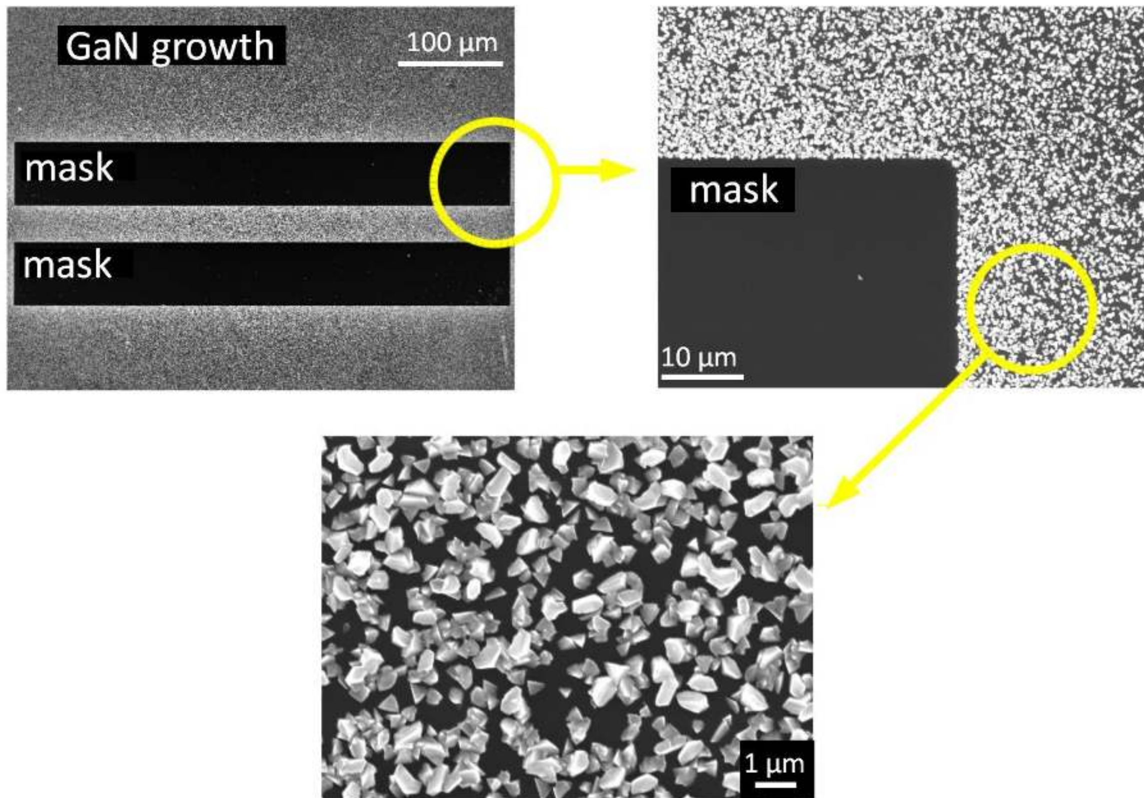

Figure 40. SEM images with three different zoom levels of GaN microSAG on Silicon(111)

Next, we tried GaN NSAG on bare Silicon (111) with similar results. Figure 41 shows optical microscopy images of coalesced NSAG on line-only and densely-packed-dots mask patterns. As in the micron-scale regime, we achieved perfect selectivity, but growth continues to be sparse and polycrystalline. The polycrystals seeded in the apertures are so strongly misoriented that the geometry is random and coalescence does not create anything resembling a coherent layer. Subsequent experiments on un-buffered Silicon were unable to produce reasonable-quality, and this naïve approach was abandoned for AlN-buffered Silicon templates.

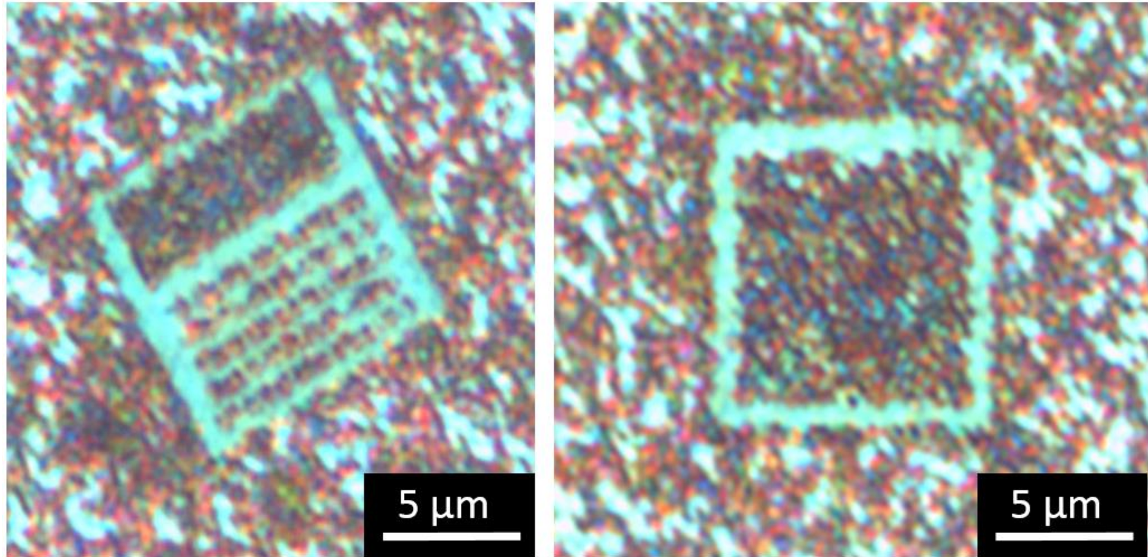

Figure 41. Optical microscope images of GaN NSAG on bare Silicon (111) substrates. The (left) image is of growth on the line-only mask pattern, and the (right) image is of growth on a closely-packed dots-only mask pattern. In both cases, growth time was extended to observe coalescence in the dense ridges and dots.

4.2 The AlN-buffered Silicon (111) template

Lattice and thermal expansion coefficient mismatch aside, growing on bare Silicon has chemical problems involving unwanted reactions between Si and our precursor species [47, 48]. After failing to grow on bare Silicon, we began experimenting with templates comprised of 200 nm AlN buffer layers grown on Silicon (111) wafers by a patented plasma vapor deposition technique [49]. For these growths, we used 100 nm thick SiO_2 masks patterned with either densely-spaced (P=367 nm) 70x2000 nm^2 stripes or densely-packed (honeycomb d=166) 70 nm dots. Total mask dimensions ran a gamut from 10x10 µm^2 to 34x34 µm^2, with a variety of margins between the aperture array and mask edge. Figure 42 shows STEM images of our AlN-buffered Silicon template. The 200 nm AlN buffer is nanocolumnar, with each columnar grain being misoriented from the others. This can be explained by the N-Si reactions that took place early in the AlN growth, creating an amorphous Si_xN_y layer that formed the uneven and noncrystalline substrate for subsequent AlN growth.

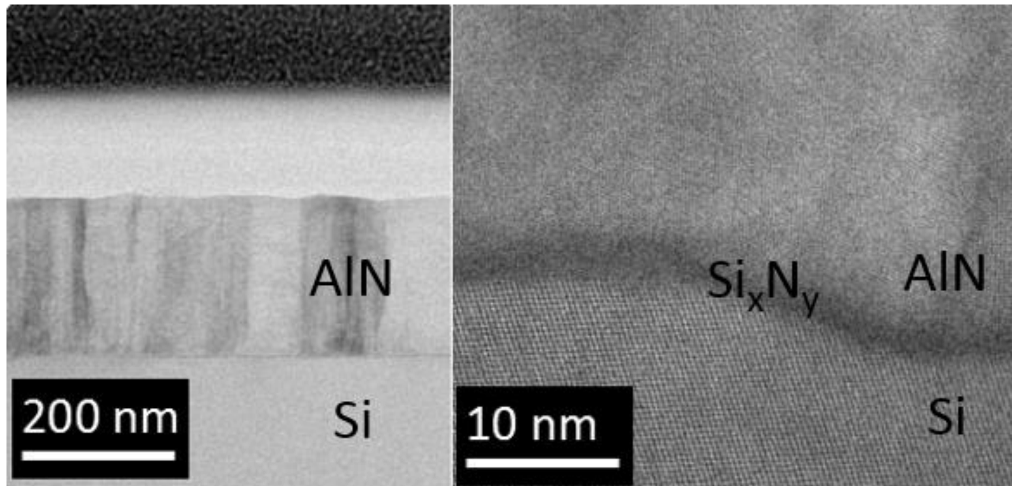

Figure 42. Two different zooms of HAADF STEM images of the (1 -1 . 0) plane of our AlN-buffered Si (111) used for all NSAG in this chapter. The AlN layer is 200 nm thick and has an incoherent, nanocolumnar configuration. The interface betwen the AlN and Silicon surface is amorphous, and was found by EDX (not shown) to contain greatly increased amounts of Nitrogen, pointing to Si_xN_y.

4.2.1 GaN NSAG

We successfully achieved selective NSAG of GaN on AlN-buffered Silicon (111) by growing under Nitrogen ambient at 1000 ˚C and 80 Torr and with a molar V/III ratio of around 100. Figure 43 shows SEM images of the successful NSAG. The growth has perfect selectivity, but nanostructures are not monocrystalline and have poor uniformity of size, shape, and orientation. The crystalline granularity is due to the nanocolumnar nature of the AlN surface, which results in multiple nucleation grains of GaN that, after growing to meet each other, are too misaligned to coalesce into a single grain. This is also the cause of the poor uniformity of shape and orientation. This effect is most noticeable in the stripe-apertured NSAG, where multiple seeding locations are guaranteed to occur in the same opening. In the dot apertures, we often had one seed per aperture, which resulted in a single-crystal nanopyramids with strong faceting.

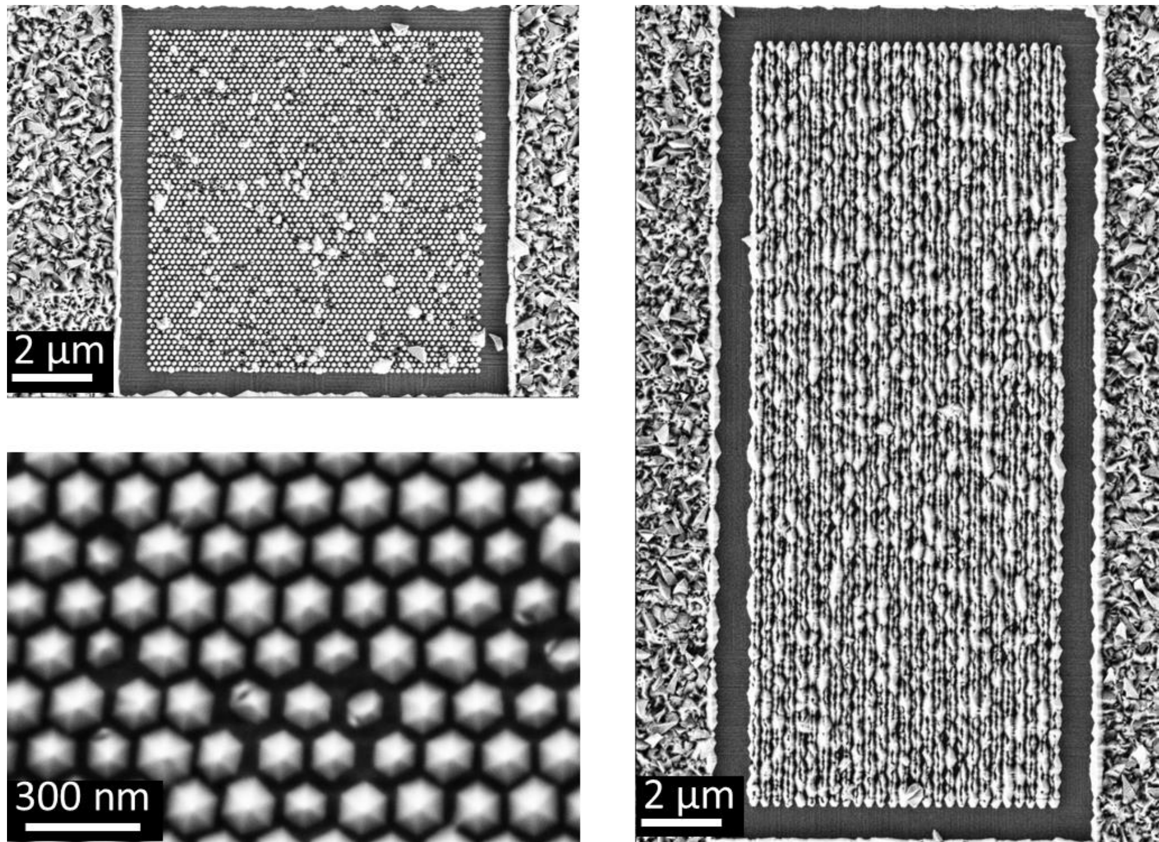

Figure 43. SEM images of GaN NSAG on AlN-buffered Silicon (111) templates. (top left) GaN nanodots grown on a 10x10 µm^2 mask. (bottom left) close zoom of the GaN nanodots. (right) GaN nanoridges grown through <1 -1 . 0>-oriented stripe-shaped apertures on a 10x22 µm2 mask.

The size differences can be explained by pits present in the AlN buffer layer under the mask. This effect is analyzed by STEM and EDX in Figure 44, which clearly shows the Ga atoms filling the pits in the AlN. These pits were later found to be due to overexposure during the SiO_2 mask etching. NSAG growth taking place in apertures suffering from this pitting effect appears stunted compared to growth which does not, presumably because the leaching of Ga atoms delayed seeding.

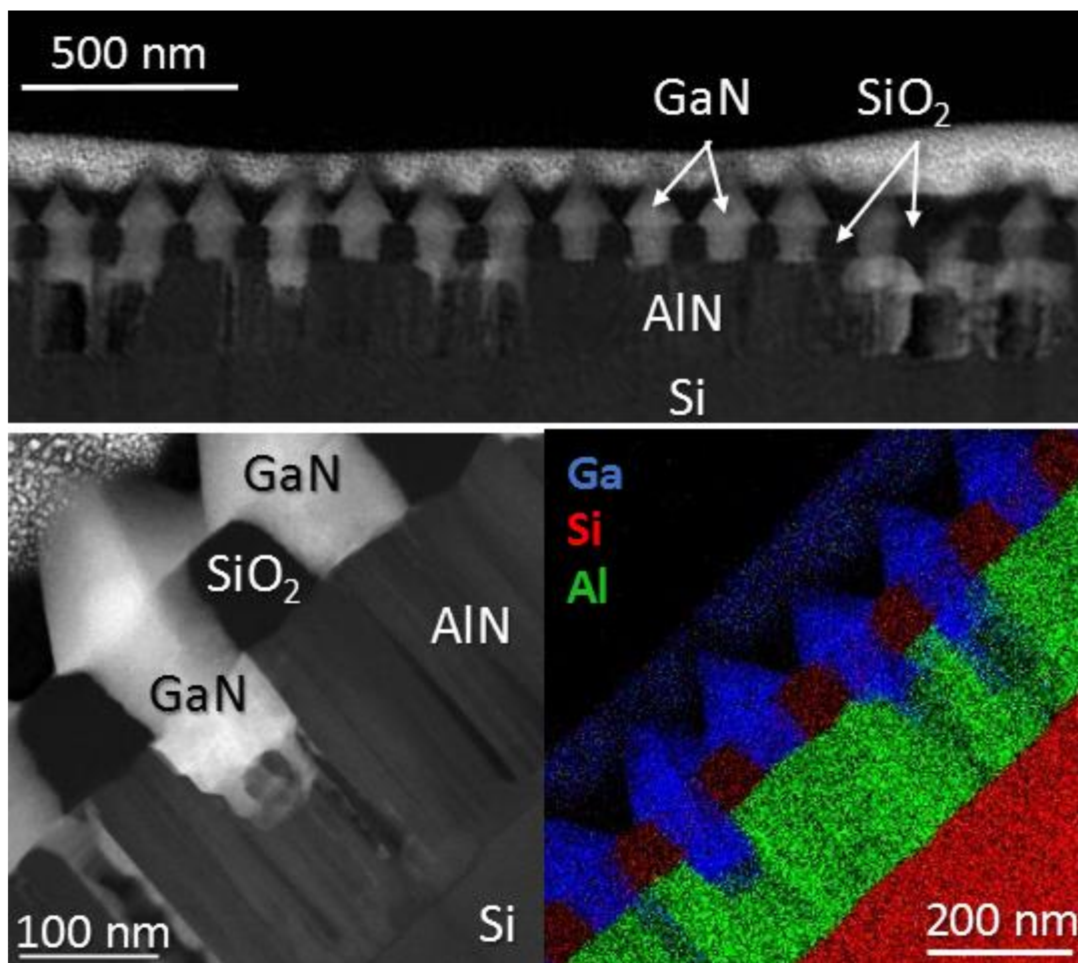

Figure 44. HAADF STEM and EDX analysis of the (1 -1 . 0) plane of NSAG GaN nanoridges on AlN-buffered Silicon showing the pitting effect at the AlN/GaN interface. The (top) image shows how nanoridges grown atop pitted regions are smaller than others. The (bottom left) image shows a close up. The (bottom right) image is an EDX analysis of the region. The back-etching effect can be described as AlN being eaten away and only partially replaced by GaN, leaving a good deal of empty space in the affected region.

A new masking method not involving reactive ion etching (see section 2.1.1) solved the pitting problem (Figure 45), but because of the nanocolumnar nature of the AlN, we were unable to achieve single-crystal nanostructures from stripe apertures. In addition to the new masking method, we decided to continue the present work solely with dot patterns, which produced well-faceted and 90% single-crystal nanopyramids with our 80 nm apertures.

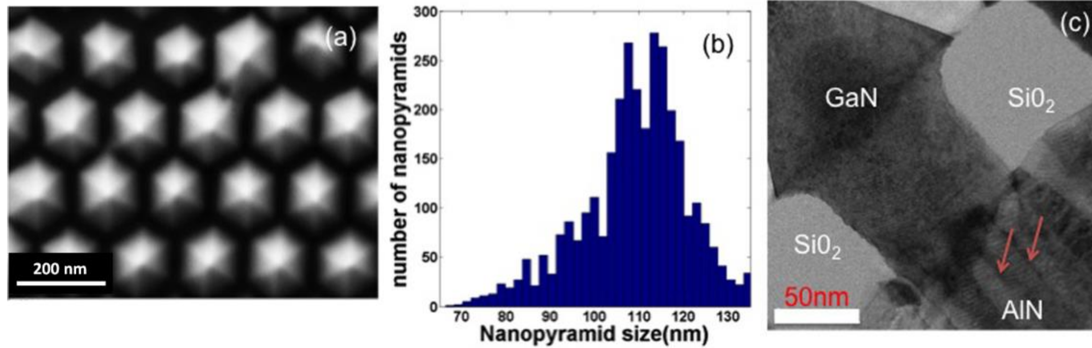

Figure 45. GaN NSAG on AlN-buffered Silicon using masks produced by our improved HSQ-based masking technology. (a) SEM image of the GaN nanopyramids, showing improved uniformity over the previous figure. (b) Size (distance between the two opposite edges) distribution histogram of the GaN nanopyramids extracted from SEM images. (c) Cross sectional STEM images of a single GaN nanopyramid on the AlN/Si template showing the lack of invasion by Ga atoms. http://dx.doi.org/10.1063/1.4931132

4.2.2 InGaN grown on NSAG GaN nanodots

InGaN is the alloy that covers visible-wavelength emission/absorption, making it the group III-Nitride system for lighting and photovoltaic applications. Despite intense interest in growing InGaN on Silicon, the exceptionally poor lattice matching results in low crystalline quality and large compositional and morphological nonuniformity [50-53], and this is in addition to the strain related problems already present in InGaN growth on GaN substrates (see section 3.3). After achieving uniformly-sized GaN NSAG on AlN-buffered Silicon(111), we went on to tackle this problem.

We used a densely-packed dots pattern to grow 20 nm thick GaN nanodots by NSAG at 1000 ˚C and 80 Torr, under Nitrogen ambient with a V/III molar ratio of 100. Then, we adjusted our growth conditions to 800 ˚C and 100 Torr, and turned on the TMIn to grow 100 nm of InGaN on the dots, resulting to InGaN nanopyramids atop 20 nm GaN seeds. SEM and CL results are shown in Figure 46. We achieved faceted, uniform nanopyramids with a primary luminescence peak at 525 nm, corresponding to an InN content of 20.7%. This luminescence is roughly 50% stronger, 20 nm redder, and 30% sharper (FWHM) than that from the field, and it's interesting to note that the nanostructures do not produce an InGaN defect band.

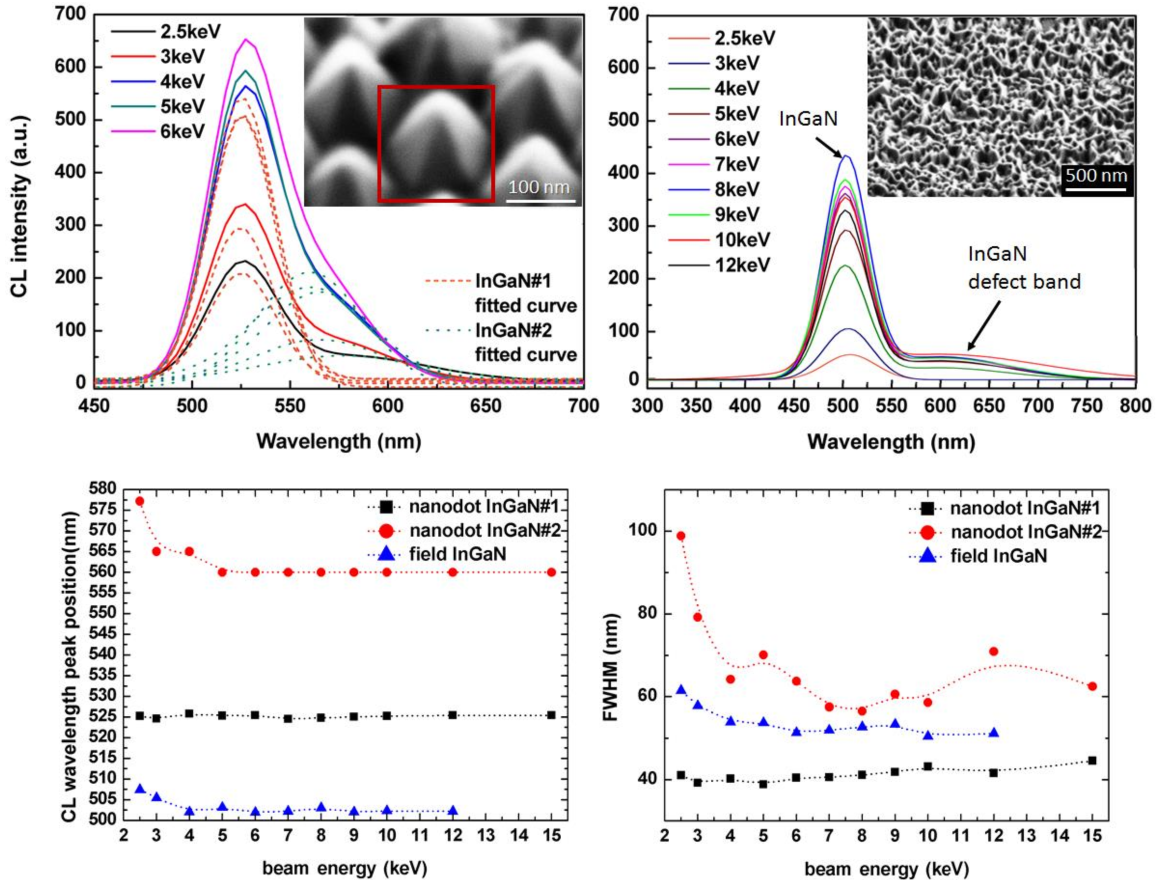

Figure 46. Cathodoluminescence analysis of InGaN nanopyramids grown on 20 nm NSAG GaN nanodots. (top left) CL spectra at various e-beam energies of the InGaN nanopyramids. 2-peak fits are shown with dotted lines. The more intense peak is denoted InGaN#1, and is positioned at 525 nm, which corresponds to a (fully relaxed) In content of 20.7%. The secondary peak is denoted InGaN#2, and its position redshifts with depth, spanning between 560 nm and 577 nm, which correspond to an InN content between 24.1% and 25.6%, respectively. It's interesting to note that the nanopyramids do not show a defect band. (top right) CL of the 2D field, showing both the InGaN peak (between 502 nm to 507 nm, corresponding to 18.2% and 18.8% InN, respectively) and the InGaN defect band around 620 nm. (bottom left) an analysis of the CL peak positions as a function of beam energy, which corresponds to depth in the sample. The secondary In-rich peak "InGaN#2" redshifts by 17 nm as we traverse the depth of the nanopyramid, while the other InGaN peaks remain relatively constant. (bottom right) analysis of FWHM of the observed InGaN peaks in the nanopyramids and the field. The FWHM of InGaN#1, the primary InGaN peak in the nanopyramid, is about 30% smaller than that of the InGaN peak from the field. The secondary, In-rich InGaN peak InGaN#2 has a large FWHM at the surface, and becomes smaller as we advance deeper into the nanostructure.

CL spectra also show a secondary, In-rich InGaN signal at 560 nm (24.1% InN), which actually becomes bluer (lower InN content) and higher quality (lower FWHM) as we look deeper in the nanostructure. We will continue to see this phenomenon in

subsequent InGaN nanopyramid growths, and we will perform a cross-sectional study later in this section.

A second InGaN nanopyramid sample was grown with increased TMIn flow in order to increase our In incorporation. Figure 47 shows the results. The nanopyramids were again well formed, and there were again 2 InGaN peaks in CL and no defect band. This time, In incorporation was enhanced by 3% InN, but at the expense of significantly wider CL curves. In this case, the secondary, In-rich InGaN peak was almost as strong as the primary peak, and suggests areas of In incorporation as high as 28.7%.

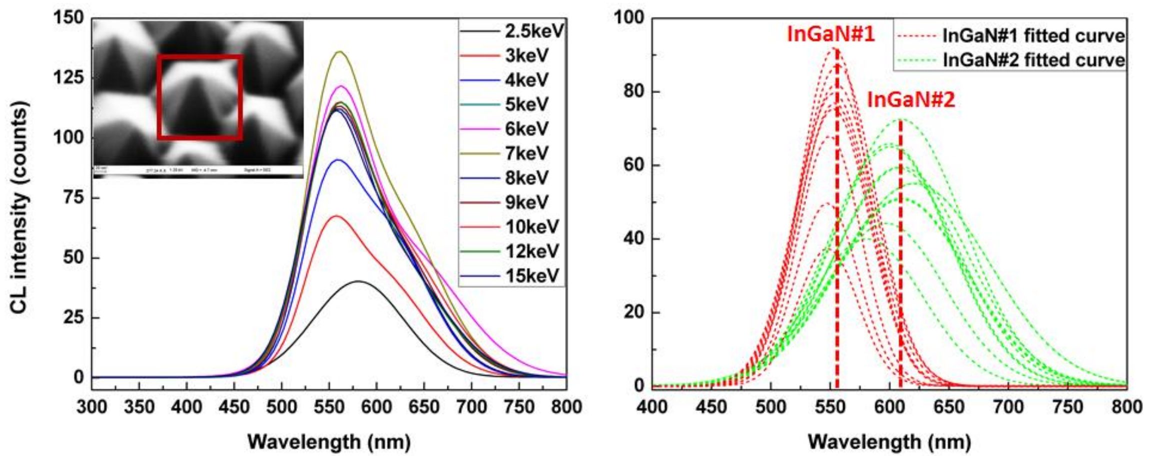

Figure 47. Cathodoluminescence analysis of a representative InGaN nanopyramid from the sample grown with higher TMIn flow on 20 nm NSAG GaN nanodots. (left) CL spectra at various e-beam energies of the InGaN nanopyramids. (right) 2-peak fits of the curves on the left. The more intense peak is denoted InGaN#1, and is positioned at 556 nm, which corresponds to a (fully relaxed) InN content of 23.7%. The secondary peak is denoted InGaN#2, and its position redshifts with depth, spanning between 597 nm and 610 nm, which correspond to an InN content between 27.5% and 28.7%, respectively. The nanopyramids do not show a defect band.

By then lowering the growth temperature to 780 ˚C, we achieved a boost in InN composition (to 33% in NSAG) without any increase in CL FWHM. We then did a full analysis of this low-temperature sample that was analogous to that done for the GaN template in section 3.3 [54]. As before, we begin with a high-resolution XRD analysis of the planar InGaN growth from the unmasked part of the sample (Figure 48). We see clearly the 3 peaks corresponding to the AlN buffer layer, 20 nm GaN layer and the

InGaN. Asymmetric reciprocal space mapping (inset) reveals that all layers are fully relaxed, justifying the use of Vegard's law for associating the fit to fully relaxed $In_{0.28}Ga_{0.72}N$. SEM analysis of the planar InGaN (not shown) shows the expected rough morphology defined by V-defects and trenches.

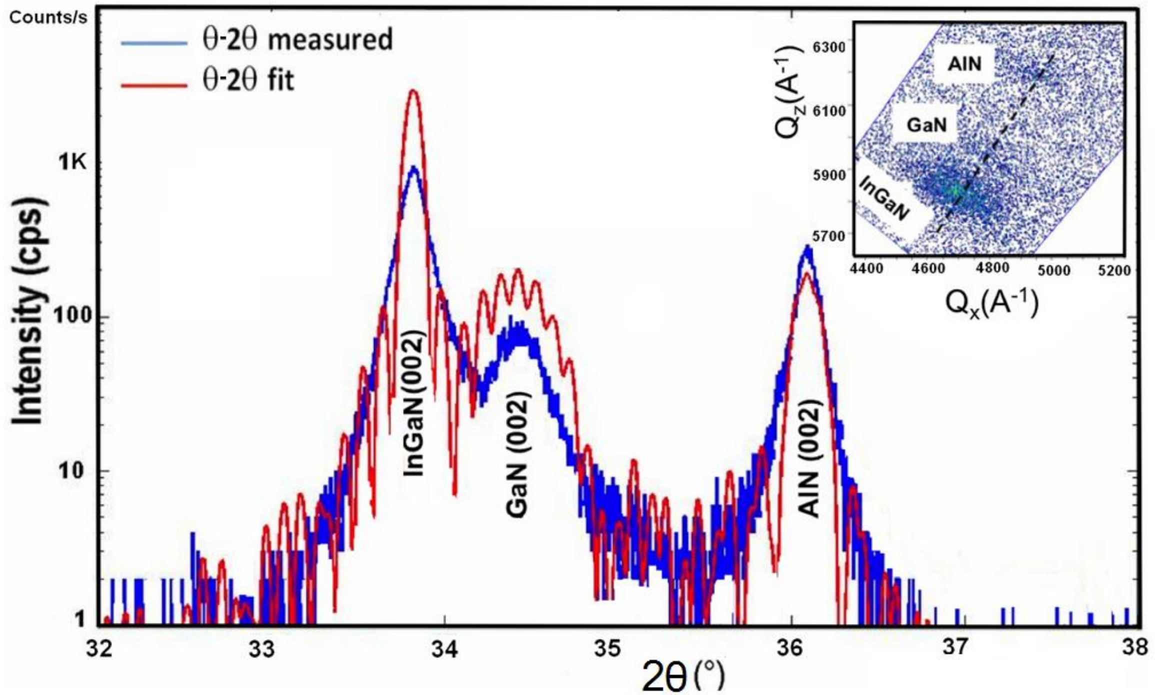

Figure 48. High-resolution XRD θ-2θ scan with its simulated fit for the (00.2) reflection of planar InGaN (outside of the patterned area) on the low-temperature InGaN sample. Inset is the RSM of the (11.4) reflection, showing that both the GaN and InGaN are fully relaxed. http://dx.doi.org/10.1063/1.4931132

Figure 49 shows SEM analysis of the InGaN nanopyramids. As in previous samples, we see perfect selectivity and a six smooth-sidewall morphology, though the lower temperature has reduced the growth rate and therefore the average pyramid size. Over 90% of the nanopyramids are hexagonal with clear facets. Figure 49c presents a statistical analysis of nanopyramid size, with over 90% of the nanopyramids within 7 nm of 86 nm (measured side to side, not corner to corner).

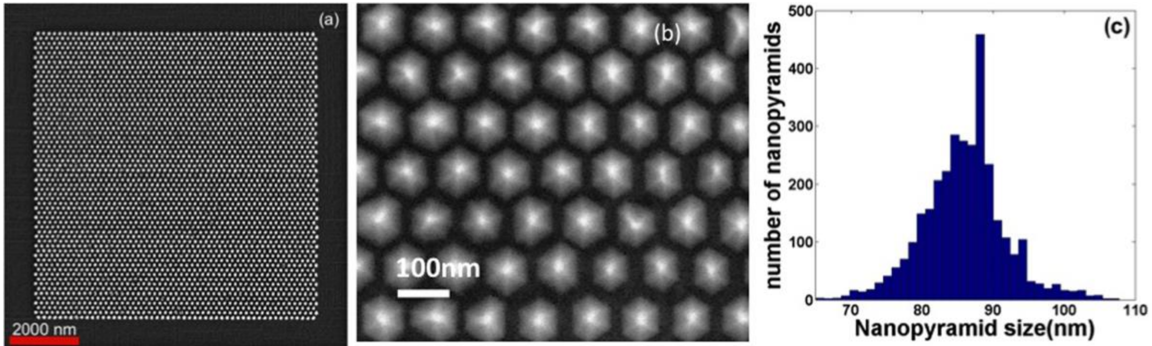

Figure 49. SEM analysis of the low-temperature InGaN nanopyramids on 20 nm GaN nanodots. (a) SEM image of the InGaN nanopyramids grown on the 10×10 μm² patterned region. (b) Higher magnification SEM image of the InGaN nanopyramids. (c) Size distribution histogram of nanopyramids. http://dx.doi.org/10.1063/1.4931132

The structure and composition of the InGaN was studied by cross-sectional STEM. Figure 50a shows a bright-field STEM image of the planar growth in the unmasked area of the sample. The extreme 3D nature of the growth is evident, with a high density of V-defects caused by threading dislocations originating from the AlN buffer layer. In contrast, the nanopyramids in Figure 50b and c are monocrystalline, dislocation free and very uniform in morphology and faceting. This is due to the single crystal GaN nanodots originating from a single nucleation point on the AlN buffer layer, as explained at the end of the previous section. We also see no sign of dislocations, indicating fully elastic strain in the InGaN (and perhaps GaN) layers. The EDX analysis in Figure 50c shows a very uniform 33% InN composition throughout the nanopyramid. (The low reading at the apex and GaN interface is expected for EDX near interfaces.). This confirms that our NSAG technique has successfully overcome the clustering and composition pulling that plagues 2D planar InGaN growth.

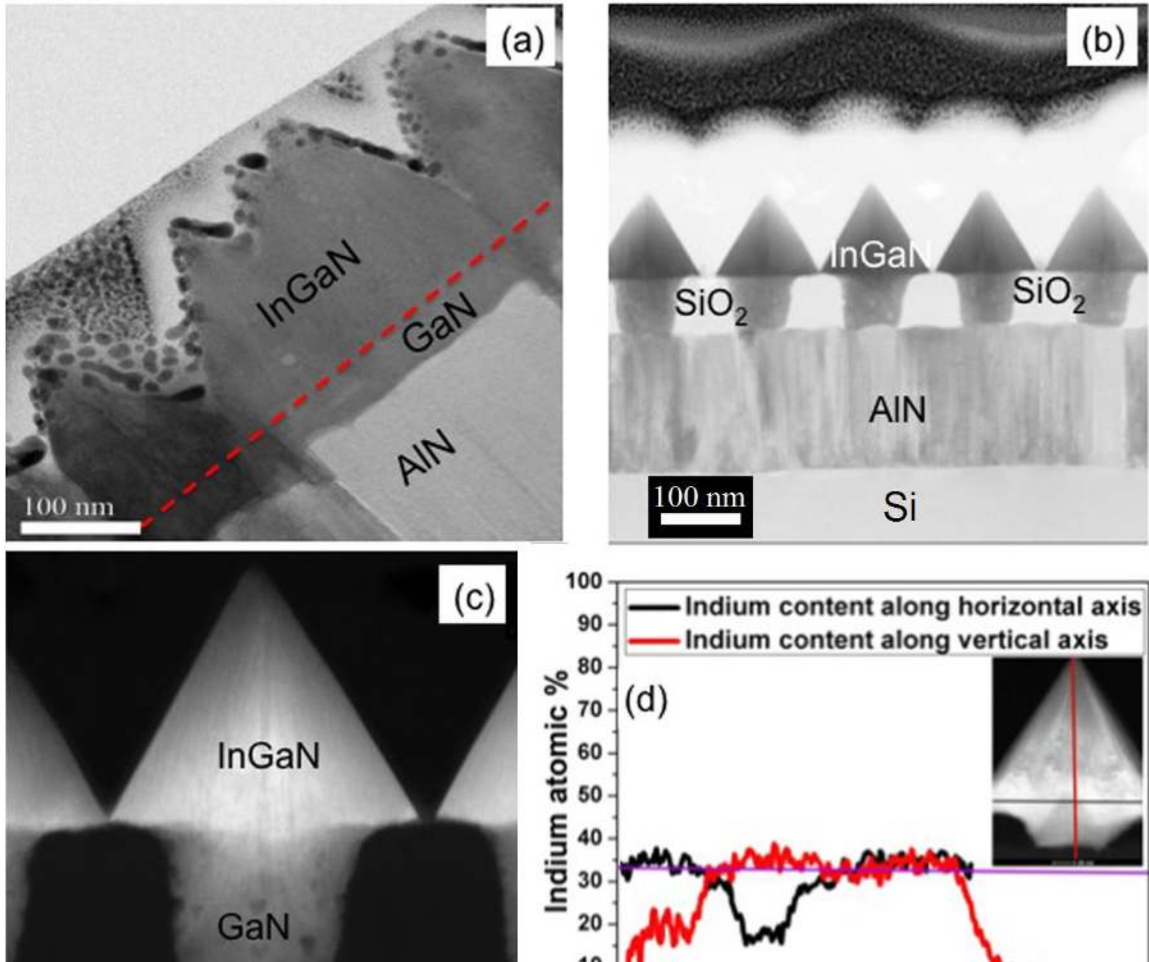

Figure 50. STEM/EDX analysis of the low-temperature InGaN sample. (a) Bright-field STEM image of planar InGaN grown on the non-patterned area. The red dotted line denotes the perceived interface between InGaN and GaN. (b) Bright-field STEM image of InGaN nanopyramid arrays grown on the patterned area. The different coloration between the parts above the mask and below the mask are due to thickness effects in the cross-section, and do not indicate different phases/grains of material. (c) Cross sectional HAADF-STEM images of a single InGaN nanopyramid. (d) EDX line scans for indium in InGaN nanopyramids along the vertical (red) and horizontal (black) axes of the nanopyramid. http://dx.doi.org/10.1063/1.4931132

The emission characteristics of both the planar and NSAG growth was studied with low-temperature CL (Figure 51). At these beam energies (5–7 keV), the electron beam energy corresponds to a depth of maximum energy loss varying in the range of 40-60 nm, and thus, the spectra consist of luminescence from the 100 nm thick InGaN region. Planar InGaN (inset) exhibits two luminescence bands, which are centered at 562 nm and 700 nm. The short wavelength peak can be attributed to the near band edge emission of InGaN with an InN incorporation of 25% (InN composition determined

according to the work of Orsal *et al.* [32] taking into account both the relaxation rate of the layer and the associated bandgap bowing parameter). The other luminescence band spanning from 550 nm to 750 nm originates probably from the localization of excitons at potential minima in In-rich InGaN areas suggesting the expected In content fluctuations in planar InGaN. In the nanopyramid, we observe a large luminescence band centered at 625 nm, corresponding to InN composition of 30%. A second, weaker luminescence band centered at 680 nm (InN composition of 33%) can also be seen. Thus, under the same growth conditions, we observe higher InN composition in the nanopyramids than in planar InGaN. Under similar excitation (5 keV), comparing the largest luminescence bands, we obtain almost four times larger peak intensity from the InGaN nanopyramids than from planar InGaN, likely due to higher crystalline quality in the nanopyramid.

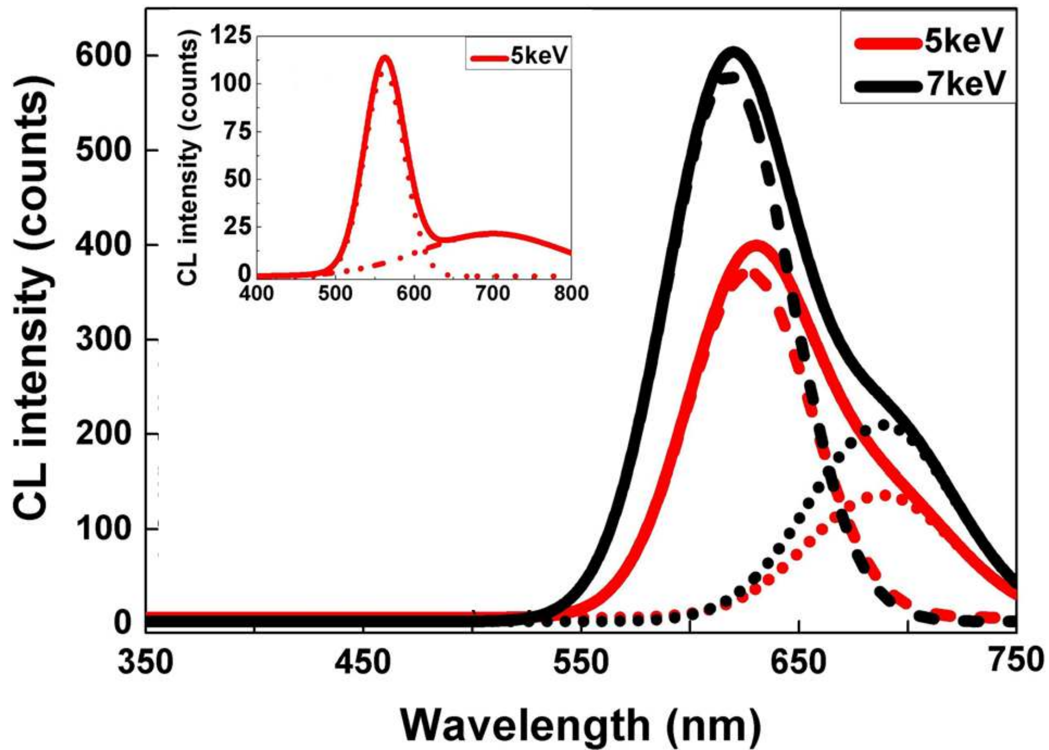

Figure 51. Low temperature (77 K) CL emission spectra from a single low-temperature InGaN nanopyramid with respective peak deconvolutions in dashed lines. Inset shows the CL spectra and peak deconvolutions from the planar InGaN. http://dx.doi.org/10.1063/1.4931132

In conclusion, we used previous success growing NSAG GaN on AlN-buffered Si(111) to develop a technique for obtaining highly uniform, single-crystal, dislocation-free InGaN nanopyramids that are free from phase clustering effects and other nonuniformities found in planar growth. With additional effort, we achieved a maximum InN composition of 33%, with NSAG material showing four times better emission characteristics than planar material on the same substrate. We note that this improvement over planar growth is far more pronounced for AlN(111)-buffered Silicon substrates than for GaN, which was only around a 30% improvement (see Figure 36).

4.2.3 Mask geometry study of InGaN on NSAG GaN nanodots

A study of the effect of the margin-size between the dot-shaped apertures and the outer edge of the mask was performed for InGaN grown on NSAG GaN nanodots. The objective was to explore a potential technique for creating structures with differing InN concentrations using only a single growth run, which would allow us to inexpensively make InGaN-based micro-pixel devices.

The three mask geometries explored are shown in Figure 52(a)-(c). There's a very clear growth enhancement for larger margins, if only for the outermost nanopyramids, and CL results confirm that growth on 16 µm margin masks have different optical properties than that on 4 and 1 µm margin masks, resulting in both green and orange luminescence, respectively, in the same growth. The outermost pyramids had optical properties identical to those of the interior pyramids, despite their enhanced size.

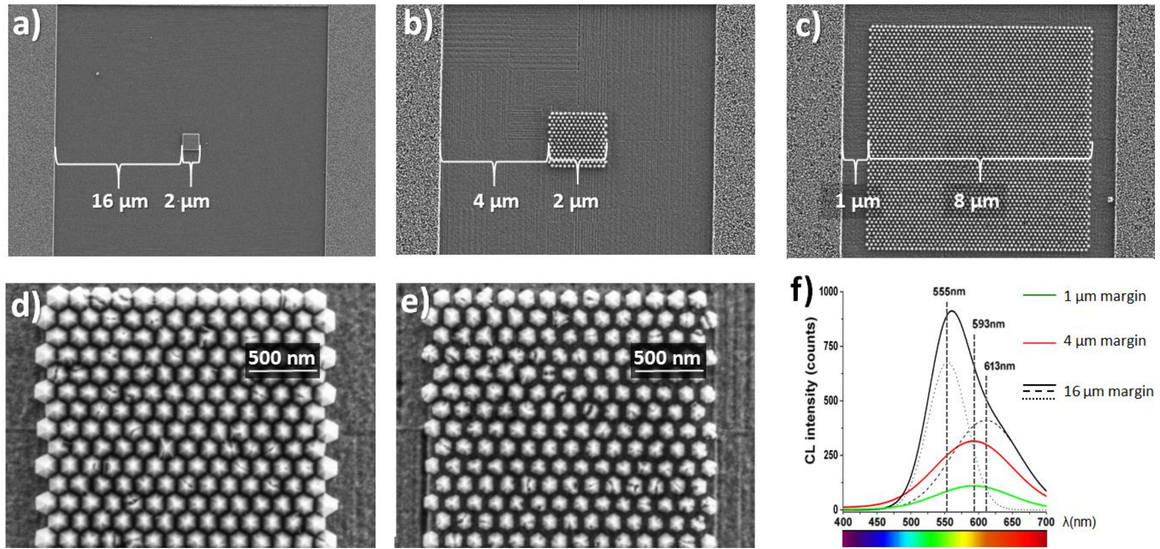

Figure 52. The different mask dimensions used to study the effect of mask margin size on InGaN on NSAG GaN on AlN-buffered Silicon (111). (a) SEM image of growth on the 16 μm-margin mask. (b) SEM image of growth on the 4 μm-margin mask. (c) SEM image of growth on the 1 μm-margin mask. (d) close-up SEM image of growth on the 16 μm-margin mask. (e) close-up SEM image of growth on the 4 μm-margin mask. (f) Fits of CL spectra of the InGaN nanopyramids grown on 3 different margin sizes. Solid curves are total fits, and the dotted and dashed black curves are deconvoluted fits of the 2 peaks present in the 16 μm-margin mask sample. Peak positions are indicated with dashed lines and the visible spectrum is shown along the λ-axis.

A statistical analysis of the nanopyramid sizes was performed using SEM images as intensity maps. Figure 53 illustrates the technique and shows the results for the 4 μm and 16 μm margin masks. Size distribution for the 1 μm margin mask (not shown) were found to be very similar to that for the 4 μm margin mask. All 3 margins produced inner pyramids of around 1400 nm^2, with size enhancement on the outermost pyramids increasing with margin size as follows: the 1 μm margin produced 2000 nm^2 outer pyramids, the 4 μm margin produced 2250 nm^2 outer pyramids, and the 16 μm margin produced 3000 nm^2 outer pyramids. The CL spectra (Figure 52) were uniform in a single mask, and did not depend on whether inner or outer dots were measured, indicating that the growth enhancement operates equally on both InN and GaN bond formation.

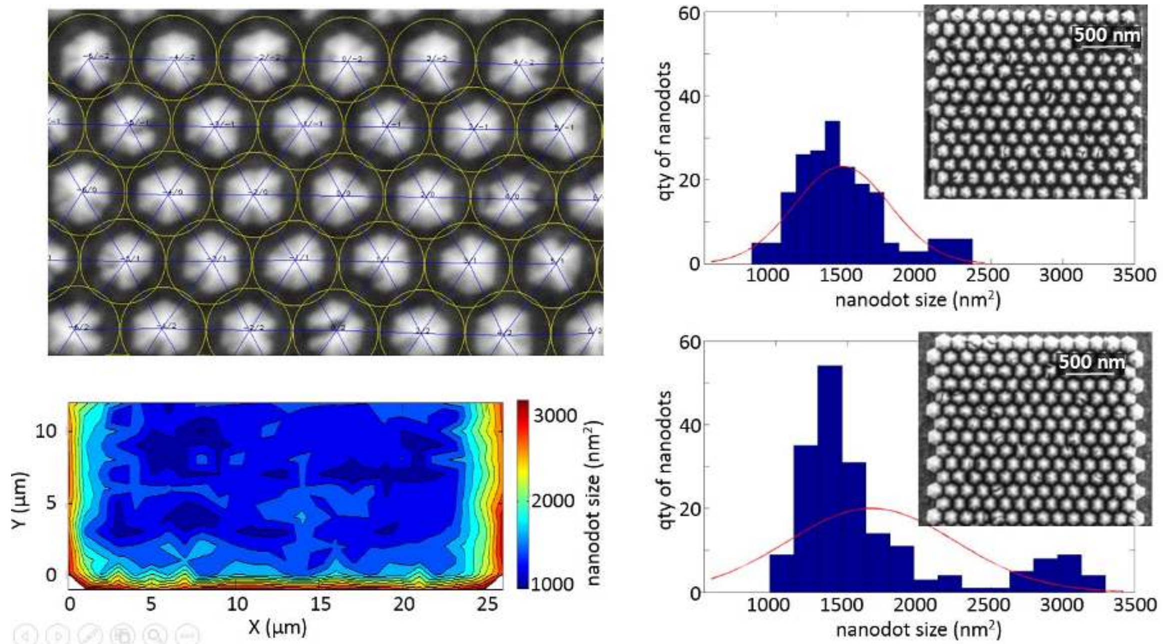

Figure 53. Nanopyramid size analysis of InGaN on NSAG GaN on AlN-buffered Silicon (111) for mask margins of 4 and 16 µm. (top left) SEM image of nanopyramids grown on the 4 µm margin mask. A nanopyramid's size is calculated by the area of inclined surface contained within its corresponding yellow circle, i.e., any part that's flat is presumed to be the mask surface. (top right) Size analysis for the 4 µm margin growth. (bottom right) size analysis for the 16 µm margin growth. (bottom left) nanopyramid size distribution for the 16 µm margin growth.

Cross-sectional STEM and EDX was performed on the 4 µm margin nanopyramids. A representative example is shown in Figure 54. The HAADF STEM image clearly shows the 20 nm NSAG GaN grown on the AlN buffer layer, with the InGaN nanopyramid grown on top. The dislocation-free InGaN nanopyramid contains two different phases of InGaN, which is expected for high-temperature InGaN growth [55, 56]. The 26% InN hexagonal phase corresponds well to the 590 nm CL peak shown in Figure 52. The 10-15% InN cubic phase would correspond to CL signal around 420 nm – 480 nm, which is not present.

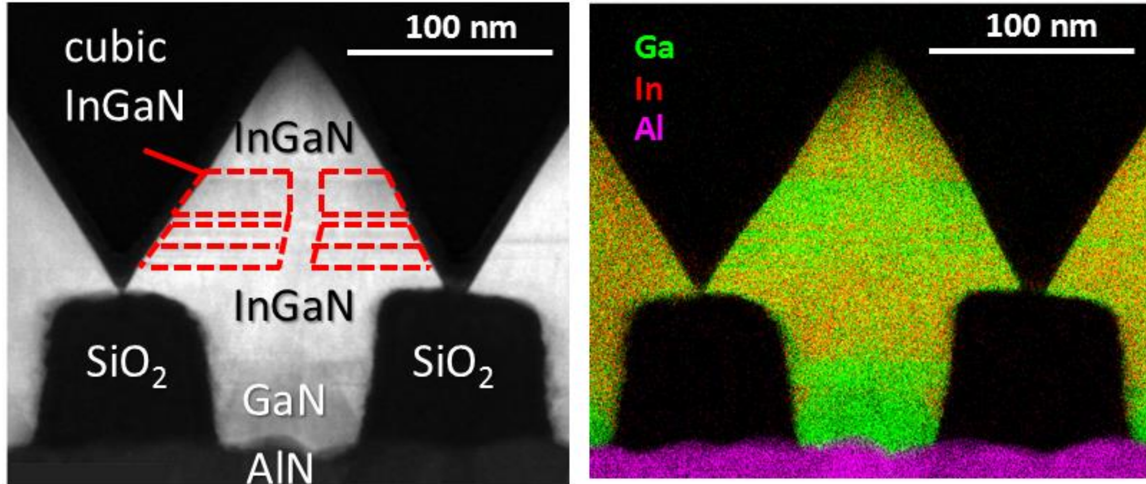

Figure 54. STEM and EDX analysis of the (11.0) plane of an InGaN nanopyramid grown on a 4 µm margin mask. (left) HAADF STEM image of an InGaN nanopyramid grown on 20 nm NSAG GaN. The red dotted lines indicate regions of cubic InGaN, which have been confirmed by simultaneous e-beam diffraction (not shown). The NSAG GaN nanodot is clearly discernable between the InGaN and AlN. (right) Simultaneous EDX analysis of the same cross section. Ga atoms are colored green, In atoms red, and Al atoms purple. The cubic regions are between 10 and 15% InN while the hexagonal regions are around 26% InN.

In an effort to boost InN composition and eliminate non-luminescing phases, we performed the same growth at a lower temperature. A summary of the results are shown in Figure 55. Again we find a similar growth enhancement effect in the outermost nanopyramids, and our CL spectra are redshifted, indicating a higher InN composition. In this sample, we achieved both green and red peaks in the same growth, a significant step towards our goal of creating single-growth micropixels. Additionally, this growth did not produce cubic regions, but rather two different hexagonal InGaN phases which are quite well dispersed within each other and do produce CL peaks. All margin sizes produced two CL peaks, corresponding to around 25% and 30%-InN phases of InGaN. Also worthy of note is that in this growth, margin size did not affect chemical composition (The green was from unpatterned field growth), so this effect seems isolated to higher growth temperatures and/or growth with cubic insertions.

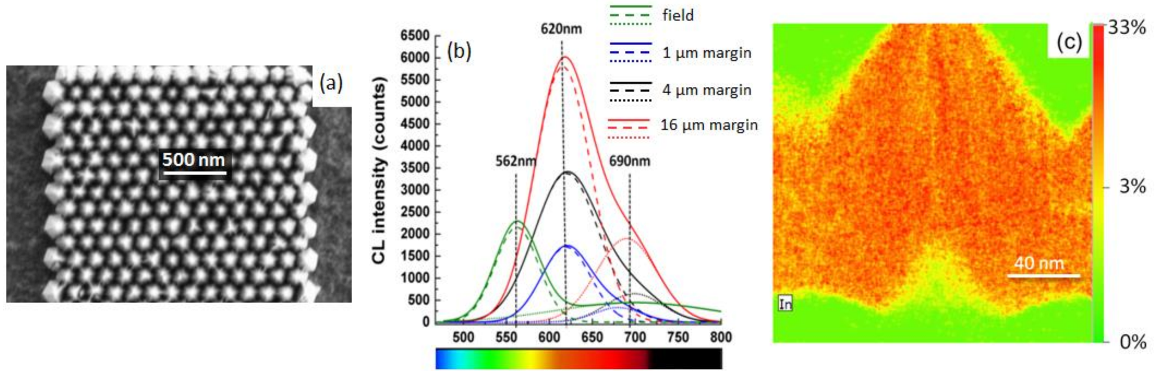

Figure 55. Margin study summary for reduced-temperature InGaN growth on NSAG GaN. (a) SEM image of the 4 μm margin growth. (b) CL analysis for 3 margin sizes and the field. Solid lines are total fits and dashed/dotted lines are fits of two peaks deconvoluted from the total fit. (c) EDX analysis of the (11.0) plane of a nanopyramid, showing fairly uniform In distribution.

4.2.4 InGaN grown on coalesced NSAG microtemplates

Following the achievement of NSAG microtemplates on GaN (section 3.4), we sought to extend this technology to the AlN-buffered Silicon (111) substrate. As on GaN, we first produced NSAG GaN through <1 -1 . 0>-oriented stripe-shaped apertures on a 10x22 μm^2 mask, this time using our optimized conditions found in section 4.2.1. We then changed to Hydrogen ambient to create ELO growth conditions to coalesce these nanoridges over the mask until they planarized into a 2D layer, atop which we grew our 20 nm InGaN layer. An overview of the growth is shown in Figure 56.

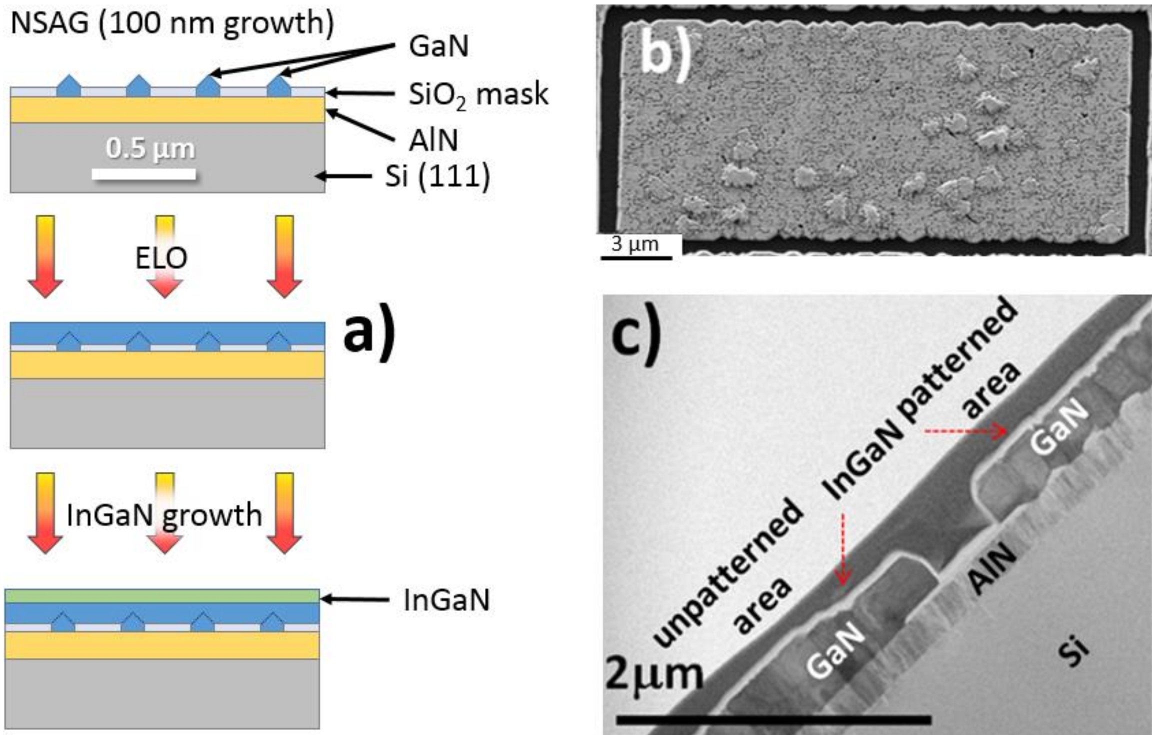

Figure 56. 20 nm of InGaN grown on coalesced NSAG GaN on AlN-buffered Silicon (111). a) The growth steps: GaN nanoridges are obtained by NSAG on AlN-buffered Silicon. Then, growth conditions are adjusted for ELO and carried out to coalescence and planarization, resulting in a high-quality 2D layer. 20 nm of InGaN is then grown on this coalesced GaN. b) SEM image of the 10 x 22 µm² masked region after coalescence and InGaN growth. The dark area is the non-apertured mask region. c) wide-zoomed bright-field STEM image showing the field (left) and NSAG region (right). The thin, white layer is the 20 nm InGaN growth. The dark layer atop the entire sample is Carbon, which was applied during FIB for characterization by STEM.

Figure 57 shows the surface roughness analysis of the InGaN grown in the NSAG region versus that grown in the field. A quick visual understanding of the high-level roughness can be gleaned from the SEM image on the right, which shows both the field and the NSAG region, separated by a dark unapertured mask margin. The topography is dominated by irregularly-shaped hillocks of which there are less in the microtemplate than in the 2D field. The roughness rms on the 3x3 μm^2 scale is 8.909 nm and 24.780 nm for the NSAG region and the field, respectively. However, on the smaller (0.75x0.75 μm^2) scale, the field is actually less rough than the NSAG region, indicating that the features giving rise to the larger-scale roughness are themselves quite broad.

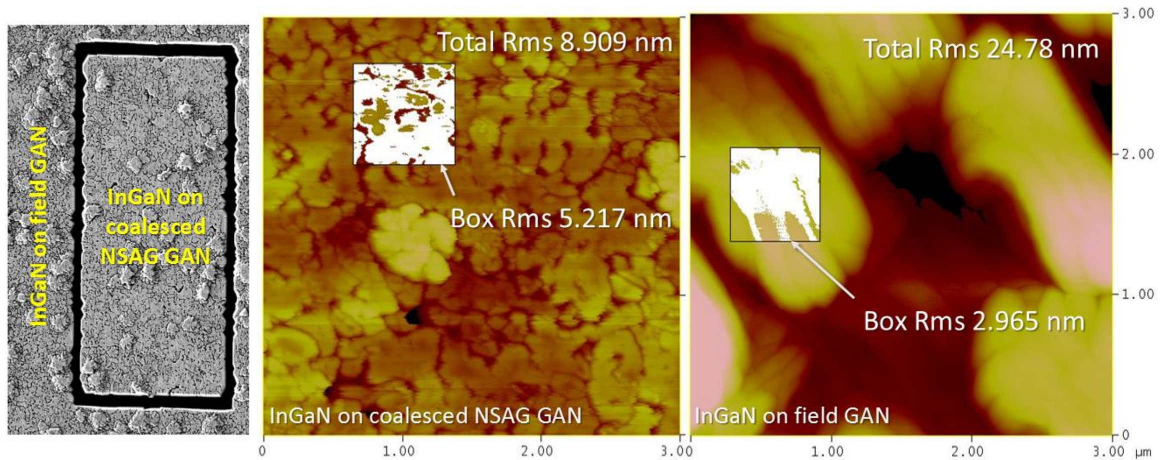

Figure 57. Comparison of the InGaN surfaces in the NSAG region and field region. (left) SEM overview including both the NSAG region and field region. (center) AFM of a 3x3 µm² square of the InGaN surface in the NSAG region. The RMS roughness in the entire region is 8.909 nm, and that of the small boxed area is 5.217 nm. (right) AFM of a 3x3 µm² square of the InGaN surface in the field region. The RMS roughness in the entire region is 24.780 nm, and that of the small boxed area is 2.965 nm.

Figure 58 lays out a cross-sectional study of the lattice and optical properties. The bright-field STEM image shows the granular structure, with grains bounded by coalescence axes, including coalescence that takes place between disparate nucleation seeds in the same aperture. This pattern creates an average grain width of roughly 340 nm, half the size of the period of the stripe apertures. At each grain boundary is a v-defect, circled in green in the STEM image in Figure 58. It's also clear from this image that threading dislocations originating from the AlN/GaN interface do not survive to the planarized GaN surface.

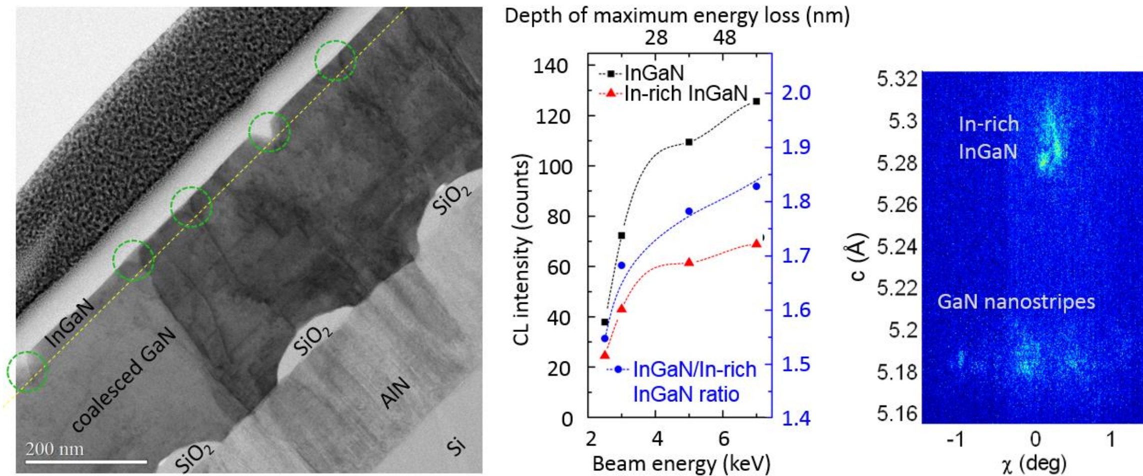

Figure 58. Lattice and bandgap analysis of InGaN grown on coalescened NSAG GaN on AlN-buffered Silicon (111). (left) bright-field STEM image of the (1 -1 . 0) plane. The dotted yellow line demarks the InGaN/GaN interface, which doesn't show up well in the bright-field regime. V-defects are circled in green. (center) CL peak intensity of signal from InGaN (black squares) and In-rich InGaN (red triangle) versus electron beam energy connected by a Chi-squared fit. Beam energy can be converted to depth of maximum energy loss (top axis) using Monte Carlo statistics, which allows us to perform an intensity vs depth analysis. The ratio between the peak intensities of CL signal from InGaN and In-rich InGaN (blue) increases with depth, indicating that the In-rich InGaN is present more strongly (or perhaps entirely) in the top layer. (right) CCD image of diffracted intensity from the (00.4) reflection at the grain boundary between two coalesced NSAG GaN nanoridges. The ω angle is optimized to show diffracted signal from the two grains of In-rich InGaN, which has very little mosaic spread, even though the underlying coalesced NSAG GaN nanostripes show a variety of grain orientations.

CL analysis shows two InGaN peaks, a strong one suggesting a 13% InN composition and a weaker one from a more In-rich InGaN lattice suggesting 17% InN. These two compositions are present in both the NSAG region and the field (not shown), though the NSAG region produces 6.7 times the intensity of the field region, indicating substantially higher InGaN epilayer quality on microtemplate GaN than on field GaN.

Depth-resolved CL finds that the ratio between the intensity of CL from the dominant InGaN and that of the In-rich grain increases with depth, indicating that the In-rich lattice exists mostly or entirely at the surface. Figure 58 also shows a CCD image taken with submicron-beam XRD. The goniometer was optimized to highlight the In-rich signal, which is seen to be quite uniformly oriented, especially compared to the diversely oriented grains of the coalesced GaN upon which it grows. It's interesting to note that the two planar InGaN grains grown on adjacent GaN grains are so closely

oriented. This may suggest that changing growth conditions and/or precursor species tends to encourage the merging of grains or that the NSAG GaN was already near some sort of coalescence critical thickness where grains begin to merge. It's also possible that grain boundaries are easier to coalesce in InGaN than in GaN. Note that the orientations of the two InGaN grains are between two GaN grains, and also that parts of the lattices of each InGaN grain do share the same orientation. In the field (not shown), the InGaN XRD peaks indicate grains misoriented on the same scale as the underlying GaN field.

When comparing the STEM image in Figure 58 to that of analogous growth on the GaN-buffered Sapphire template (Figure 39), the first thing that stands out is the sheer density of dislocations and stacking faults that the former suffers during early growth. These defects are largely overcome before the InGaN/GaN interface, but one type of defect that persists are the grain boundaries, both those at the coalescence points over the masks and those originating from multiple grains seeding in the same aperture. On the GaN-buffered Sapphire substrate, some of these grain boundaries are deleted before reaching the surface, but we do not see that on AlN-buffered Silicon (111), probably because of the larger misorientations between grains that is due to the nanocolumnar AlN layer.

4.2.5 NSAG BGaN

BGaN is a particularly interesting and challenging material system. Besides the resilience and bandgap engineerability shared by other Group III Nitride systems, BGaN has the potential for tunable resistivity and neutron sensitivity [57, 58] and is transparent to the near-UV spectrum. Additionally the large difference in lattice parameter compared to other Group III-Nitrides makes it extremely interesting for bandgap and strain engineering [59, 60]. However, it's perhaps the most challenging of the ternaries, suffering from strain-related degradation, Boron clustering, phase separation, and 3D

columnar growth even at very low BN concentrations [61]. After using NSAG to solve similar problems in InGaN, we decided to study the application of these techniques to BGaN. To that end, we performed NSAG of BGaN on both AlN-buffered Si(111) and GaN-buffered Sapphire, which allowed us to decouple the effects of lattice mismatch and nanocolumnarity from those of our NSAG technique. We used the same masks as for the previous margin study of InGaN (section 4.2.3), and optimized growth conditions independently for the two substrates.

On both templates, NSAG of BGaN was performed in a low pressure MOVPE reactor with a target of 1.5% boron incorporation. Triethyboron, trimethylgallium and ammonia were used as growth precursors. We opted for nitrogen ambient after experiments under hydrogen ambient produced highly irregular, top-heavy nanopillars on the AlN/Si(111). For both templates, the growth temperature was 1000 °C, the pressure 100 Torr, and the V/III ratio around 800.

To understand the effect of the templates used, we first analyzed 2D BGaN growth in the unpatterned field region. The lattice was studied using X-ray diffraction, wherein well-identified XRD peaks for the 00.2 reflection of BGaN were obtained with ω-2θ scans on both GaN and AlN/Si(111) templates along with their corresponding template peaks as shown in Figure 59. The BGaN (002) peak is almost in the same 2-theta position on both templates, indicating very similar mean unit cell sizes and boron incorporation on both the templates. Total relaxation in the structure was confirmed by reciprocal space map (not shown). Thus, from the simulation fit shown in (Figure 59), we interpret the XRD peak position to indicate around 1.5% BN composition (composition inferred based on Vegard's law with CBN = 4.17 Angstrom) on both substrates. As expected, the diffracted intensity from the BGaN field on the GaN substrate is around an order of magnitude stronger and the FWHM around 3 times narrower than that on the AlN/Si(111), suggesting a vastly superior lattice uniformity. In-situ reflectivity measurements (not shown) indicated growth of ~150-nm-thick layers on both substrates.

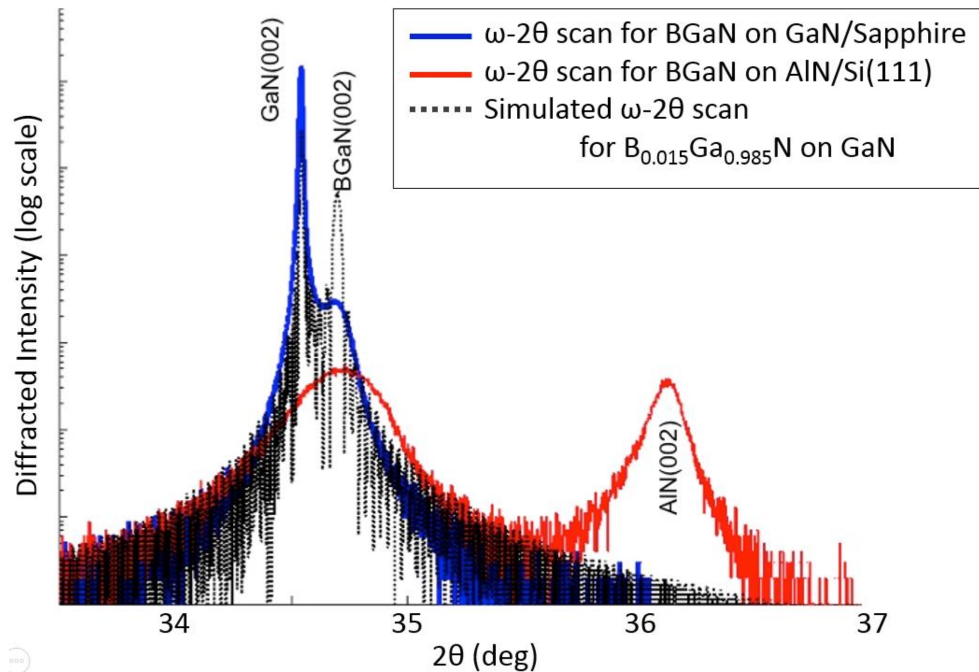

Figure 59. XRD of BGaN growth in the unpatterned fields of GaN/Sapphire (blue) and AlN/Si(111) (red) compared against simulated diffraction of 1.5% BN-composed BGaN on GaN. http://dx.doi.org/10.1088/0957-4484/27/11/115602

The surface morphology of both the templates is the typical rough and 3D BGaN surface as shown in Figure 60. The 2D-3D transition should be more drastic in the AlN/Si(111) templates due to higher lattice mismatch induced strain and nanocolumnar nature of the AlN/Si(111) template. Comparing Figure 60(a) and (b), the BGaN on the AlN/Si(111) template has a 3D surface very similar to BGaN on GaN template. The 2D-3D transformation in BGaN epilayers on GaN templates is induced by boron clustering, phase separation and excess strain, due to boron incorporation, resulting in randomly spaced multi-crystalline fused nanocolumns strongly aligned to the GaN growth axis as reported previously by S. Gautier, et al. [61].

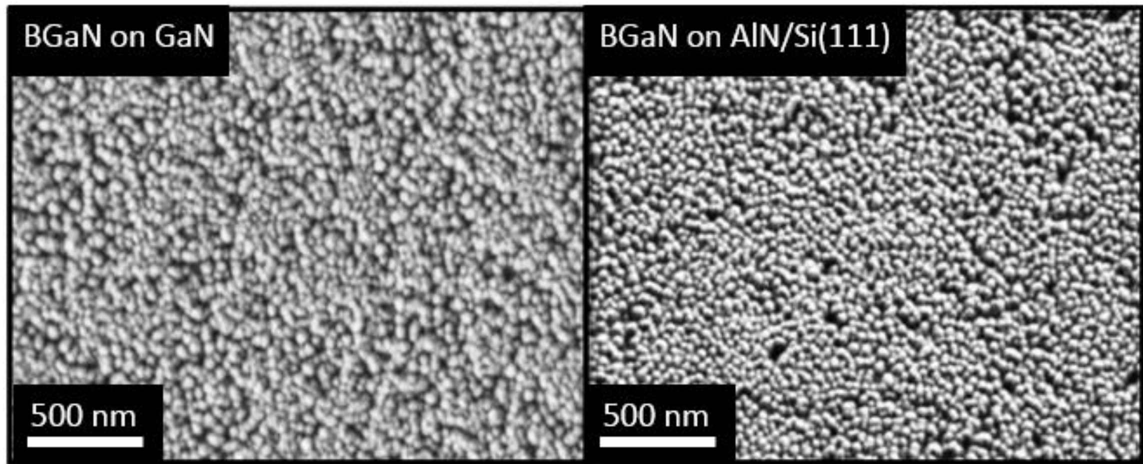

Figure 60. SEM images of 2D BGaN growth in the unpatterned field on (left) GaN/Sapphire and (right) AlN/Si(111). http://dx.doi.org/10.1088/0957-4484/27/11/115602

The selectivity, morphological quality, and uniformity in shape and size of BGaN nanopyramids in the patterned area of the GaN and AlN/Si templates were evaluated using SEM analysis. Figure 61a and b show SEM images of the NSAG BGaN nanopyramids for both substrates with their respective higher magnification images. In both cases, we achieved perfect selectivity throughout the 10x10 μm^2 mask, smooth {1 -1 0 1} faceting, and a good morphological uniformity (>90% are hexagonally shaped, the remaining triangular) as shown in the insets of Figure 61a and b respectively. A histogram of nanopyramid size distribution extracted from several patterns on GaN template and AlN/Si (111) template is shown in Figure 61c and d respectively. The mean diameter of the BGaN nanopyramids on patterned GaN templates is 83.4 nm with standard deviation of 8.21 nm, and on the AlN/Si (111) template the average size of the nanopyramids is 102.3 nm with standard deviation of 6.63 nm. A comparison of NSAG crystal size with the 3D nanocolumnar features in the field (haphazard arrangement of small grains with mean diameter ~40-70 nm (see Figure 60b), shows that NSAG has produced larger (~80-130 nm) single crystals with regular spacing, good uniformity, and smooth faceted surfaces without any visible defects on the surface (within the detection limit of the SEM), leading to the conclusion that almost all of the nanopyramids on GaN

templates are single crystals while more than ~90% of the nanopyramids grown on AlN/Si(111) are single crystal. These analyses of selectivity, size and quality confirm that the NSAG yields BGaN nanopyramids which are simillar in quality irrespective of the template used.

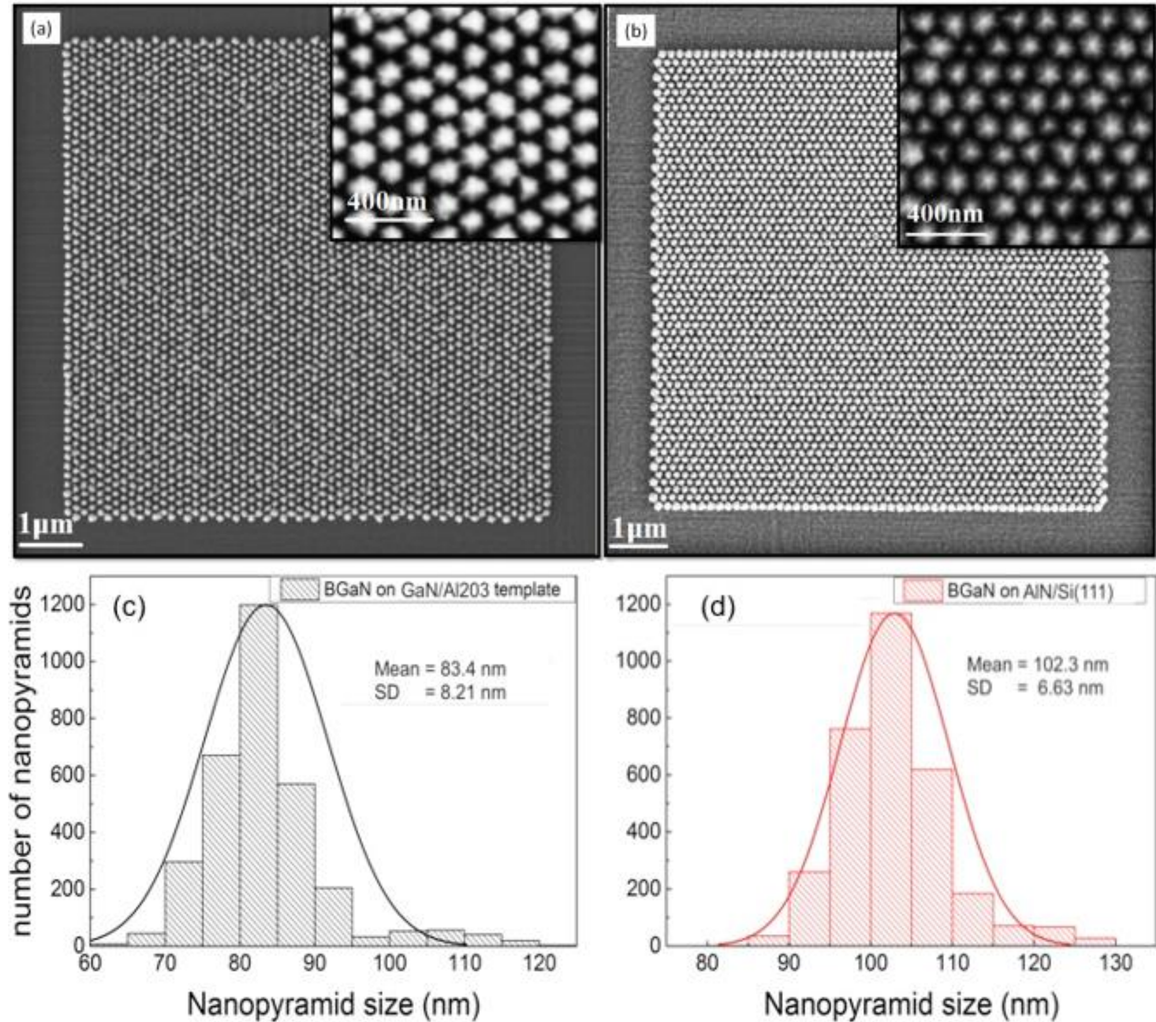

Figure 61. SEM morphology analysis of NSAG BGaN on GaN/Sapphire (a,c) and AlN/Si(111) (b,d) templates. The same 10x10 µm² masks were used for both templates. http://dx.doi.org/10.1088/0957-4484/27/11/115602

To further investigate the crystalline nature of the BGaN nanopyramids STEM analysis was carried out. Only BGaN nanopyramids on AlN/Si (111) templates were studied since NSAG is substrate independent, and so similar results are expected from the

BGaN nanopyramids on GaN templates. A representative nanopyramid cross-section is shown in Figure 62a. As expected, it is single crystal and completely free of threading dislocations from the heterointerface. The variations in contrast of the image and the grain boundary-like line tracing the top of the mask are due to the thickness variation in the TEM lamellae. The nanopyramids are single crystal because of the small 70-80 nm diameter mask opening, which lowers the nucleation rate such that the first nucleation on the seed is typically the only nucleation, leading to monocrystalline structures. The nano-scale growth dynamics should also result in full strain relaxation due to the availability of lateral free surfaces that allow the accommodation of stress without dislocation generation, as evident from Figure 62a. After around 80 nm of growth, the faceting shifts from {1 -1 . 1} marked with blue dashed lines to {1 -1 . 2} marked with red dotted lines. This is unlike anything we've seen with GaN and InGaN, which have had {1 -1 . 1} semipolar facets for the entire structure. BGaN's shift in faceting occurs at 80 nm even for enhanced-growth rate conditions (not shown), so it may be due to the difference in surface kinetics induced by low migration or higher sticking coefficient of Boron atoms.

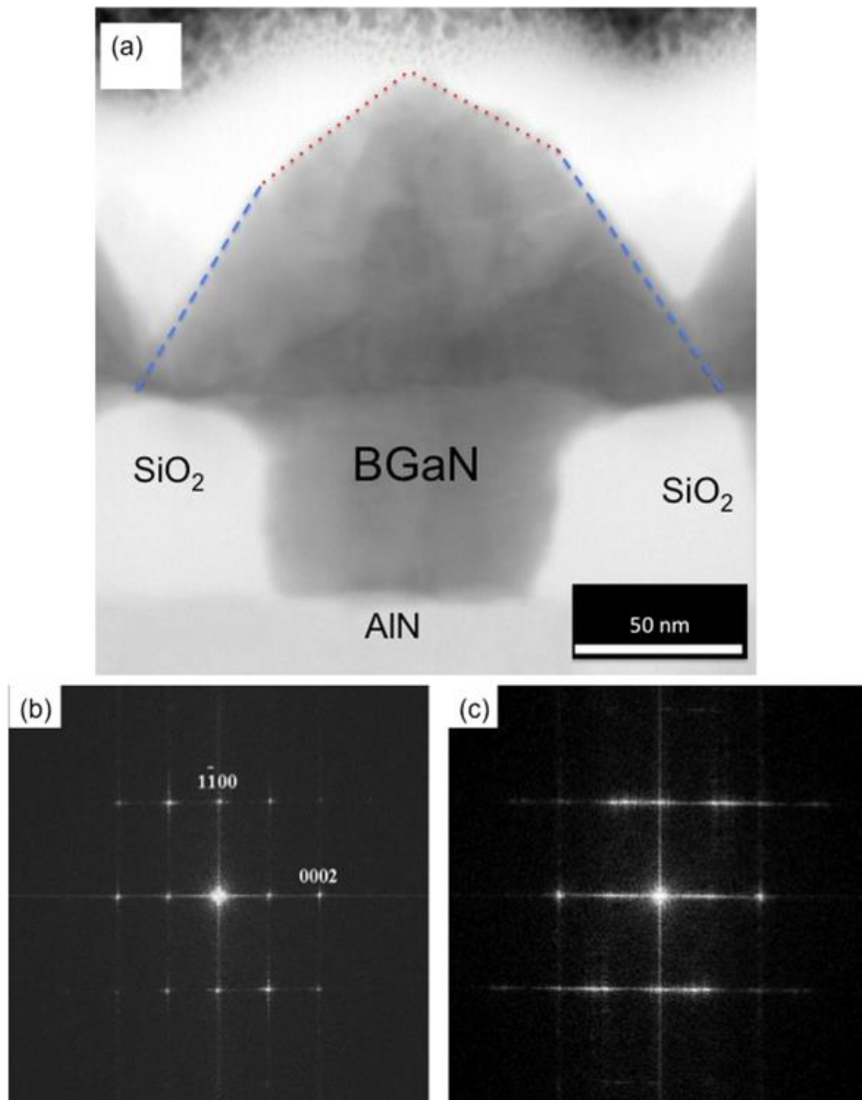

Figure 62. STEM analysis of the (1 1 . 0) plane of NSAG BGaN on AlN-buffered Si(111). (a) bright-field STEM of a typical nanopyramid. The apparent grain boundary across the middle is due to the top part being thicker, and thus darker. (b) fast Fourier transform (FFT) of high-resolution HAADF STEM images taken from the sub-mask region showing a very low density of stacking faults. (c) analogous FFT from the over-mask region, showing a high density of stacking faults. http://dx.doi.org/10.1088/0957-4484/27/11/115602

We also observed stacking faults in the top portion of the nanopyramids in the edge of the patterns (not shown), which had higher growth rate due to enhanced surface migration of the precursors from the masked regions. Detailed fast-Fourrier transform (FFT) analysis from the base of the nanopyramids (stacking fault-free region) and the top portion of the nanopyramids is shown in the Figure 62b and c, respectively. The sharp FFT pattern obtained near the base of the nanopyramids suggests that it is purely

wurtzitic. The diffused line patterns obtained near the stacking fault region suggests additional 2-3 nm wide cubic insertions in this region. This may be due to the enhanced migration of the precursors inducing increase in growth rate at the pattern edges.

Optical properties of the BGaN nanopyramids were studied using depth-resolved cathodoluminescence that showed a clear BGaN peak at 370 nm along with the near band edge (NBE) peak of the GaN template at 364 nm as shown in Figure 63a. This peak corresponds to a BN composition around 0.7-1.25 % (BN composition from the bandgap is determined according to the work of A. Ougazzaden et al. [59] taking into account the associated bandgap bowing parameter). Emission peaks of BGaN nanopyramids on the GaN template are similar to those from the non-patterened area as shown in Figure 63c. Under similar excitation, the intensity ratio between the GaN NBE and the BGaN NBE is higher (by approximately 10%) for the BGaN nanopyramids than for the field indicating better crystalline quality in the nanopyramids. On the AlN/Si(111) template, a double emission peak was obtained, one at 380 nm and another broad peak at 415 nm, shown in Figure 63b. The short wavelength peak can be attributed to the NBE emission of BGaN with a BN composition of 1.7 to 2.0 %. The other broad peak may originate from the localized variation of B incorporation induced by inhomogeneities in the BGaN layer. This indicates that the lattice strain has a compounding effect on BGaN on AlN/Si(111) resulting in phase separation. For BGaN nanopyramids on AlN/Si(111) templates, we observe a single broad emission peak at 381 nm indicating better crystallinity of the nanopyramids. The difference in B incorporation inferred by the CL spectra should be interpreted with the understanding that our XRD results (Figure 59) show that the BGaN average lattice parameters are the same for both templates with broad variation in boron content on the AlN/Si templates, so the differing CL emission profiles may likely indicate localized variation of the boron on AlN/Si templates. Determination of BGaN composition from nondestructive characterization techniques is an ongoing issue, and the reader is referred to Refs [59, 62, 63].

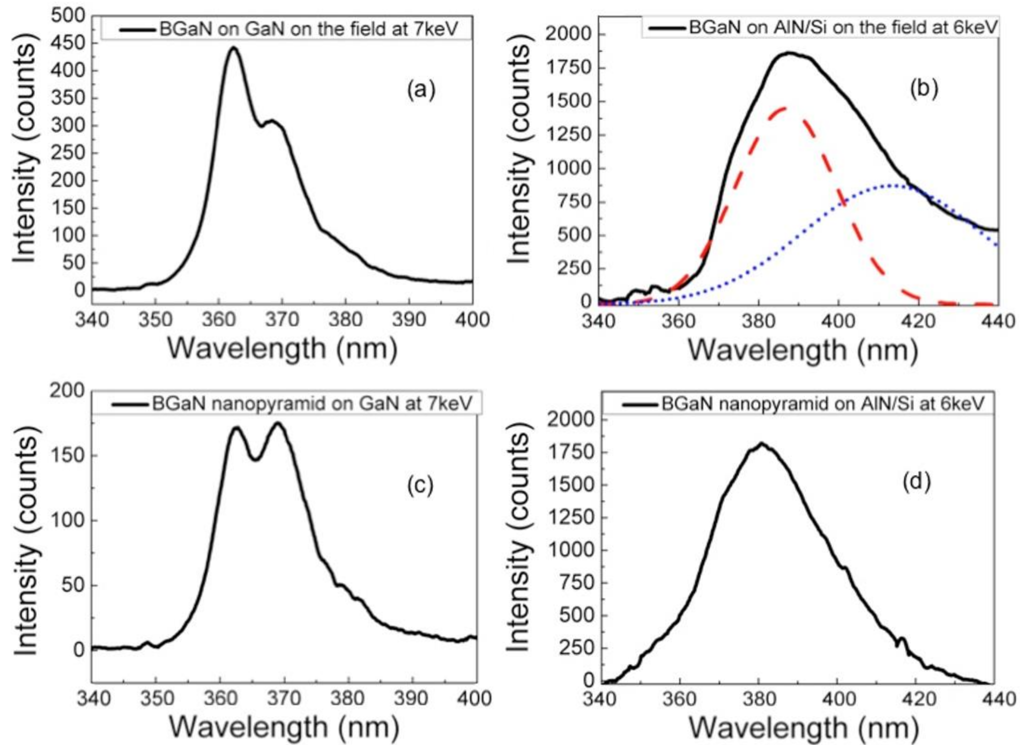

Figure 63. CL emission spectra from (a) BGaN on the GaN template on the unpatterned field, (b) BGaN on the AlN/Si(111) template on the unpatterned field (with fit of deconvoluted peaks), (c) a single BGaN nanopyramid on the GaN template, and (d) a single BGaN nanopyramid on the AlN/Si(111) template. http://dx.doi.org/10.1088/0957-4484/27/11/115602

In summary, we have simultaneously studied NSAG of BGaN nanopyramids on two substrates, comparing the inexpensive AlN/Si(111) to the conventional, more lattice-matched GaN/Sapphire. STEM and SEM analysis clearly shows that the nanopyramids on both substrates have smooth sidewalls and are mostly single crystalline, and CL analysis suggests BN composition between 1.25 and 2.0%. As expected, we found unmasked field growth of BGaN to be of a much lower quality on AlN/Si(111) than on GaN, but also found that the former benefitted more from NSAG, owing to its low BGaN nucleation rate on the nanocolumnar AlN buffer layer. While the epilayer quality on AlN/Si(111) is still far behind that on GaN, this work is a significant step towards the ability to produce high-quality BGaN epilayer and nanostructure-based devices on a far less expensive substrate.

CHAPTER 5

CONCLUSIONS AND FUTURE WORK

5.1 Summary of Completed Work.

This work achieved a range of success in NSAG of Group III-V Nitride nanostructures and microtemplates on both traditional substrates and the inexpensive AlN/Si(111) template, and we opened the way for exciting future work in this subject.

Our first grand success was the achievement of NSAG GaN on AlN/Si(111), where we achieved perfect selectivity and defect-free nanopyramids, 90% of which are single crystal. The primary difficulty was found to be the nanocolumnar nature of the AlN buffer layer, which causes the independently seeded grains to be highly misoriented with respect to each other and unable to coalesce into a single crystal. The single-crystal nanostructures we did achieve were due to the small size (~75 nm) of our nano-apertures limiting nucleation to one seed per aperture. This of course precludes arbitrarily long single-crystal lateral nanowire-like structures, which require elongated nano-apertures that invite multiple nucleation sites.

We then turned our focus to InGaN nanopyramids grown atop 20 nm NSAG GaN nanostructures. The intent was to use the 3D strain relief mechanisms of NSAG to mitigate InGaN's strain-related issues, which occur even on GaN templates. We began our work here using GaN templates, and this work culminated in NSAG-based PIN solar cell devices that produced current 3 orders of magnitude greater than their planar counterparts, and which had 20 times greater IV ratios at ±1 V. We then leveraged these techniques with our previous success growing NSAG GaN on AlN/Si(111), and produced InGaN nanopyramids on AlN/Si(111) with no defect band and 50% stronger luminescence than in unpatterned, 2D growth. These nanopyramids were highly uniform, single-crystal, dislocation-free, and free from phase clustering effects and other

nonuniformities found in planar growth. With additional effort, we achieved a maximum InN composition of 33%, with NSAG material showing four times better emission characteristics than planar material on the same substrate.

Success with InGaN nanopyramids suggested applications in pixel devices, and we undertook a study of the effect of mask geometry on InN composition. The end goal was to create a fabrication process for an InGaN-based micropixel device with a single growth step, wherein differently colored micropixels would result from different mask geometries on the same template. We found that increasing mask margin (the masked space between the nano-aperture region and the un-masked field) size blueshifts the spectra, which allowed us to grow both red and green emitting regions in the same growth.

We also explored the use of NSAG to create GaN microtemplates out of coalesced NSAG nanostructures. The resultant GaN microtemplate had far less v-defects than growth in the unpatterned field region, but grain boundaries formed by coalescence of differently oriented grains (a consequence of the nanocolumnar AlN buffer layer) were never deleted. Nevertheless, the InGaN layer grown atop the microtemplate was superior to that atop the planar field in that it both had less orientation spread and almost 7 times the emission intensity.

Lastly, we achieved NSAG BGaN nanopyramids on both AlN/Si(111) and GaN/Sapphire. As expected, we found unmasked field growth of BGaN to be of a much lower quality on AlN/Si(111) than on GaN, but also found that the former benefitted much more from NSAG, owing to its low BGaN nucleation rate. As with NSAG of GaN, BGaN nanopyramids on AlN/Si(111) were single crystal to the extent that nucleation occured once per aperture, which happened in more than 90% of the apertures. On AlN/Si(111), XRD and CL showed BN composition to be between 1.3 and 2.0%, and the nanopyramids on both substrates exhibited smooth sidewalls.

5.2 Future Work

5.2.1 NSAG on AlN-buffered Si(100)

While our achievements on Si(111) are enormous, the majority of silicon-based semiconductor technology takes place on the (100) facet of silicon. Thus, achieving group III-nitride device structures on Si(100) would allow rapid integration into existing silicon-based semiconductor technology. Unfortunately, group III-nitride growth on Si(100) is exceptionally difficult, because the lattice is not only highly mismatched but cubic! Recently, a partner lab has developed a technique for depositing nanocolumnar, c-plane AlN on the (10.0) plane of silicon wafers. Initial attempts to use these templates for GaN NSAG have produced samples showing poor selectivity and poor uniformity, but these results are nonetheless promising (Figure 64). The uneven quality of the AlN buffer layer makes it difficult to uniformly mask the surface, resulting in irregular and less-than-fully-developed apertures, openings outside intended aperture sites, and a peeling effect where the mask does not stick well to the surface. The current focus is on improving mask deposition and aperturing. Some preliminary results in this direction are shown in Figure 65. Once we've developed NSAG masking techniques for Si(100), the majority of our existing results on Si(111) will readily transfer to this new regime.

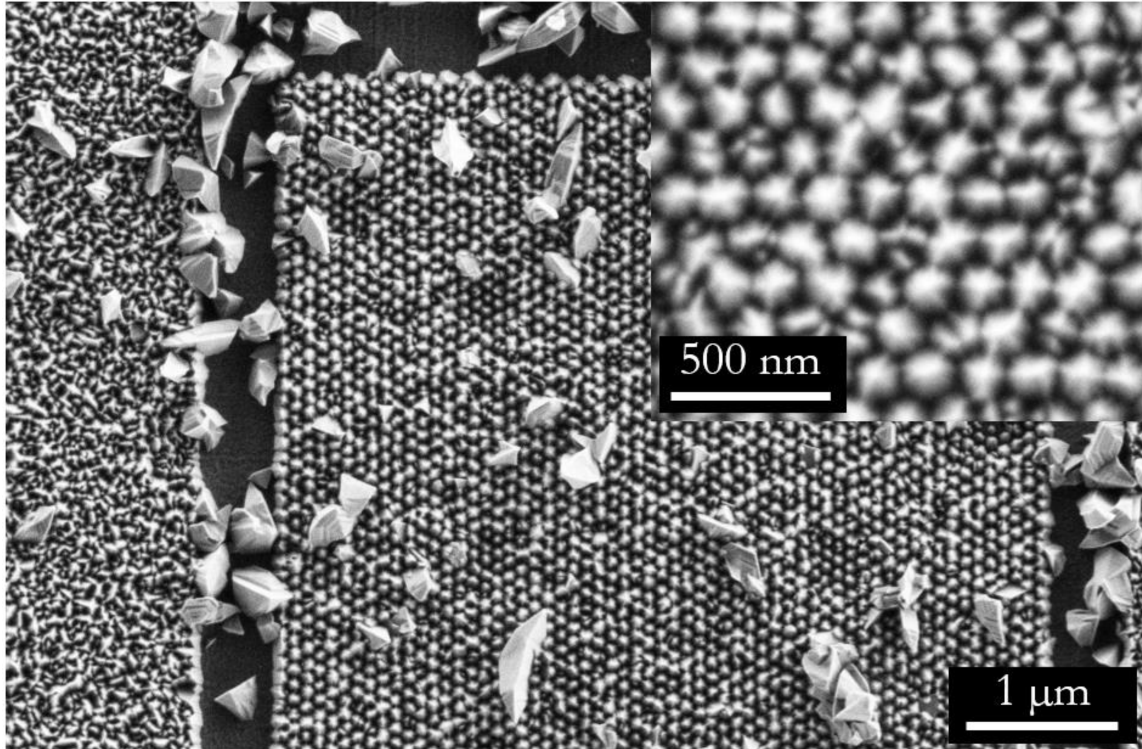

Figure 64. SEM images of initial attempt at GaN NSAG on AlN-bufferd Si(100).

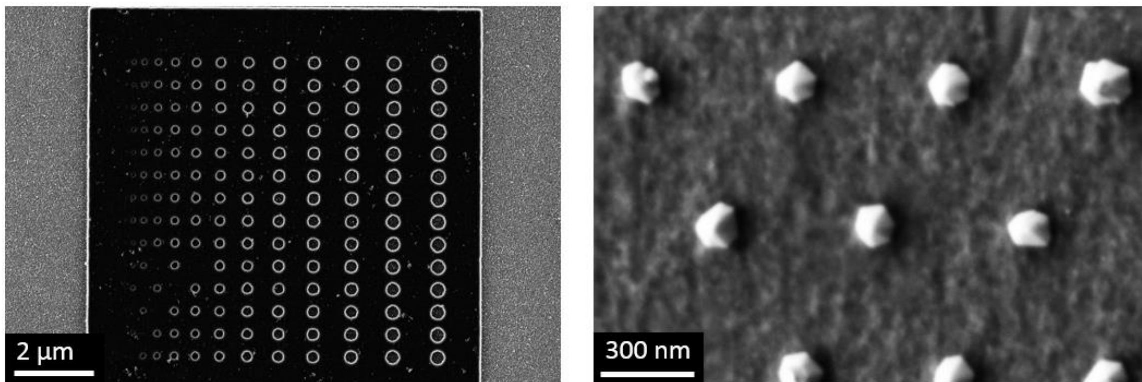

Figure 65. Further work on AlN/Si(100). (left) a mask pattern exploring different aperture diameters and e-beam lithography exposure times. (right) a small (nonrepresentative) area of mask with small-diameter apertures where perfect selectivity and single-crystallinity has occurred.

5.2.2 Further study of mask geometry

After promising results using mask margin to redshift InGaN nanopyramid luminescence (section 4.2.3), we would like to study also the effect of hole spacing and wider margins. To date, we've achieved monolithic, single-growth-step micropixel structures with emission range between 569 (green) to 690 (red), but the InGaN ternary has the capacity to cover the entire visual spectrum, if only we can select for composition using mask geometry. In section 4.2.3, we found that all mask margins below 4 μm result in the same emission, so we would continue our search in the larger margins. Large aperture spacing has not yet been tested, but we should expect that surrounding a nucleation site with more mask material should produce an effect similar to increasing mask margin.

5.2.3 Use NSAG microtemplates to produce devices

In section 4.2.4, we used a 20 nm InGaN top layer to demonstrate the suitability of our coalesced NSAG GaN microtemplate on AlN-buffered Si(111), and we found that this InGaN produced almost 7 times the emission intensity of the InGaN grown on the planar GaN in the unmasked region. This is a good proof that InGaN-based devices grown on our microtemplate would superior to those grown using more naïve methods, and we intend to leverage this success to produce such devices on silicon substrates. These devices will be considerably less expensive than analogous devices already on the market that are grown on traditional SiC or Sapphire substrates, so it's extremely interesting to compare device performance between these and our devices.

Additionally, there is still work to be done improving the quality of our microtemplates, which while free of threading dislocations are currently limited to grain sizes of roughly half the size of our aperture spacing. An obvious direction for improvement is to increase grain size by increasing our aperture spacing, but perhaps more interesting is to work at deleting these grain boundaries at the surface.

Figure 66a shows a cross-sectional STEM image of the GaN microtemplate achieved in section 4.2.4. Grain boundaries originate from coalescence planes between the apertures and from apertures in which multiple nucleation sites occur. Grain boundaries indicated by blue circles are in fact deleted before reaching the surface of the microtemplate, indicating that it may be possible to create a single-grain surface if only we continue growing GaN under ELO conditions.

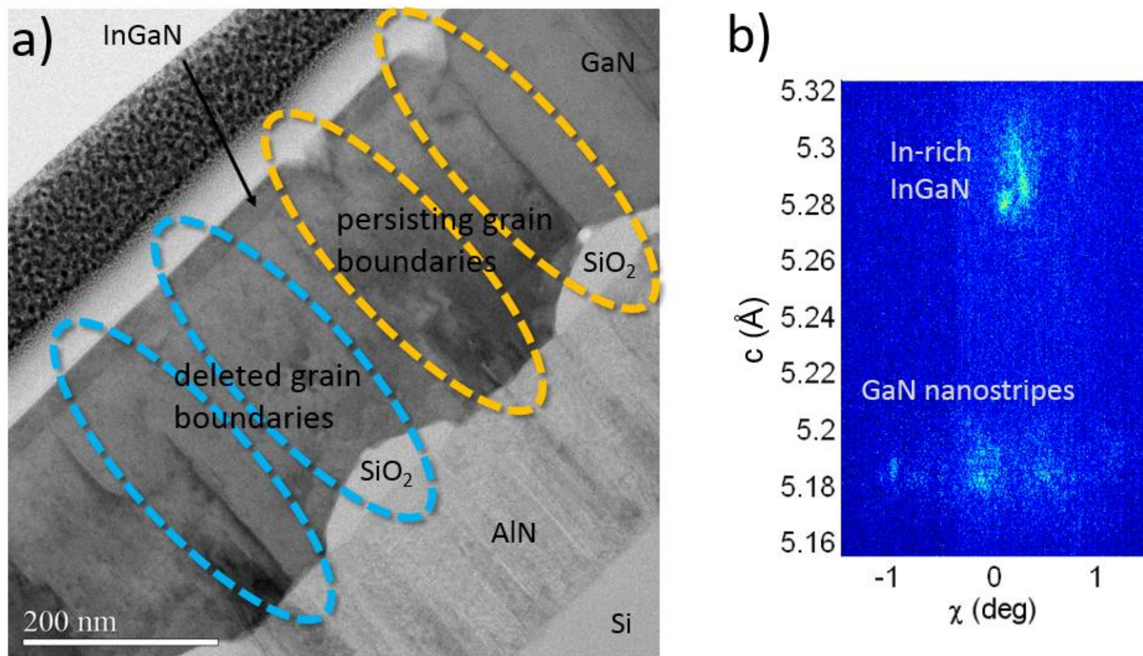

Figure 66. Surface grain analysis of planar InGaN grown on NSAG GaN microtemplates. a) bright-field STEM image of the (1 -1 . 0) plane of coalesceed NSAG nanostripes on AlN-buffered Si(111). Grain boundaries (originating from coalescence planes and from multiple nucleations in the same aperture) that are deleted before reaching the InGaN/GaN interface are circled in blue, while those that do manage to propagate to the surfaced are circled in yellow. b) CCD image of diffracted intensity from the (00.4) reflection at the grain boundary between two coalesced NSAG GaN nanoridges. The ω angle is optimized to show diffracted signal from the two grains of In-rich InGaN, which has very little mosaic spread, even though the underlying coalesced NSAG GaN nanostripes show a variety of grain orientations. EDX depth analysis (not shown) indicate that this In-rich phase forms the surface of the InGaN layer.

Figure 66b is a CCD image of diffracted intensity from submicron-beam XRD at a grain boundary of the same sample. It's striking that the spread in orientation (horizontal χ axis) between the InGaN grains (shown by EDX depth analysis in Figure 58 to form the surface of the InGaN top layer) is much less than that of the underlying GaN

grains. We understand the propagation of grain boundaries to be due to high mismatch in orientation between neighboring grains, so a slightly thicker InGaN layer may see the deletion of a great deal of grain boundaries.

We can grow InGaN thicker than 20 nm and create active regions. Nanodots are a better candidate than nanostripes for maximizing grain size. There's also some evidence that we may achieve true coalescence if we use InGaN as an intermediate layer or simply grow the GaN microtemplate a bit thicker.

5.2.4 Graphene-masked NSAG

Graphene's exceptional properties have generated an intense interest in integrating graphene into group-III Nitride-based device structures [64-68], for example as a transparent top contact for optoelectronic devices [69-71] or as a heat-spreading layer [72]. It so happens that graphene also stands to solve one of the primary difficulties with NSAG (shared by other thin-film structures), which is that of back-contacting [70, 73-75].

Graphene offers a solution to this problem in that it is both a conductive and non-wetting material that can thus serve simultaneously as an NSAG mask and a back contact, creating a vastly superior back-contacting model and reducing the number of fabrication steps. Figure 67 illustrates this concept. Note that the final placement of the graphene mask after the NSAG allows it to serve as a conductive back contact and heat-dissipating layer.

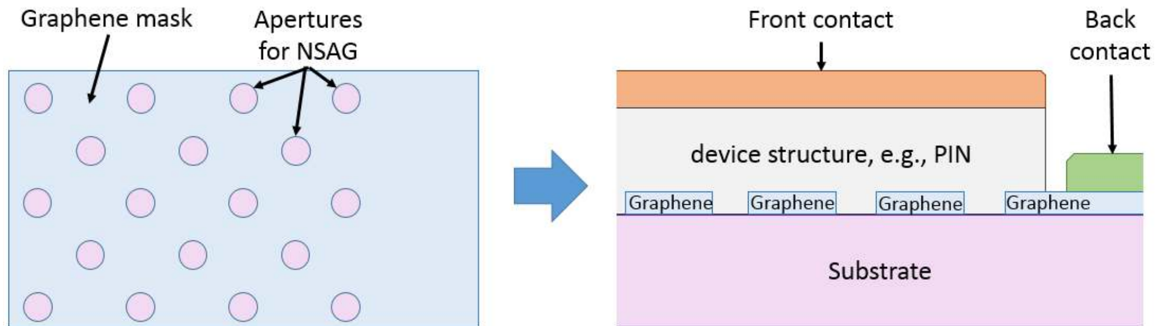

Figure 67. The principle of graphene serving simultaneously as a mask for NSAG and a back contact in the final device structure. (left) Graphene would replace SiO_2 as the masking material in NSAG growth, resulting in (right) a device structure with a built-in back contact.

In literature, graphene multilayers have been successfully deposited on Group III-Nitride materials [69-71], and our group has recently published [76] results on NSAG GaN on graphene masks formed on SiC substrates by confinement-controlled sublimination [77] and patterned using negative-resist e-beam lithography, similarly to our early process for patterning SiO_2.

SEM images of our results are shown in Figure 68. The patterned graphene mask is visible in Figure 68a, and the NSAG is in Figure 68b. Fast-Fourier transform of STEM images (not shown) reveals a triangular cubic GaN structure that becomes wurtzite after further growth time. The growth is perfectly selective and overgrows the graphene mask, resulting in a heat-dissipating back-contact.

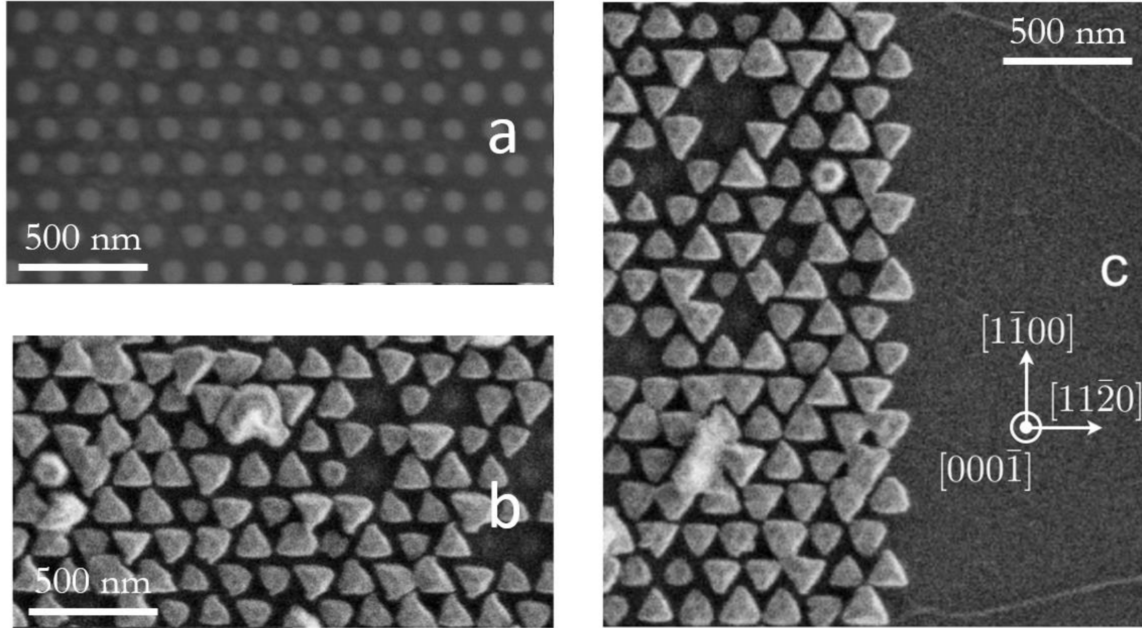

Figure 68. SEM images of NSAG GaN grown through a graphene mask on SiC. a) The pattered graphene mask. The light-colored circles are apertures through which the SiC substrate is exposed. b) predominantly triangular cubic phase GaN is grown through the graphene mask. c) The edge of the aperture area of the graphene mask showing the perfect selectivity.

While this work is ongoing on SiC, there is a great potential for other substrates. Chemical vapor deposition of SiC is already a mature technology, so that's one potential avenue to applying this technology to silicon substrates. Additionally, we've published [78] a technique to grow epitaxial graphene on SiN, which is a material easy to form on Silicon.

5.2.5 BN-based neutron detector

Thin layers of boron nitride (BN) and its alloys have emerged as an important multifunctional material system [79-81] with wide direct bandgap, high resistance to oxidation, and chemical inertness, which may find applications in both optoelectronics in the yet to be explored deep ultraviolet region [82] (100 - 290 nm, see Figure 2), and microelectronics. In addition, the polarity of BN bonds and the high surface area of BN-

related nanostructures provide good adsorption properties of various substances ranging from organic pollutants [83] to hydrogen [84]. As BN is composed of light elements, it promises absorbents with high uptake gravimetric capacity. Its high chemical and thermal stability allow it to be used in harsh environments, and suggests that recycling could be easily achieved. Nanostructured BN is therefore an ideal candidate as an absorbent material [85, 86]. Related devices can find application in high power electronics for high temperature and harsh environments, air pollution detection, water purification, UV and neutron detectors, and flame and environmental monitoring.

Being a boron-dense, large-bandgap semiconductor, BN is also a uniquely useful material for neutron detection, since it can both capture neutrons (^{10}B has an enourmous capture cross-section of ~3840 barns) and detect the capture products [87-90]. Currently fielded detectors utilize highly precious ^{3}He, which limits the quantity of detectors that can be dedicated, e.g., to nuclear nonproliferation. Additionally, medical and diffraction applications requiring CCD neutron detection solutions are not possible with this method. Therefore, efforts have been made to move from gas-based to solid-state solutions. The primary approach has been to coat a semiconductor with a boron-rich solid that converts incoming neutrons into photons and alpha particles, which can then be registered by the semiconductor [91, 92]. The problem with this naïve approach is that thinner boron-rich layers fail to capture neutrons, while thicker boron-rich layers self-absorb the capture products before they reach the semiconductor. The result is a maximum theoretical efficiency of only around 4.5% [93], slightly higher if 3D heterogeneous solutions are applied [94]. BN-based solutions however are theoretically capable of 100% efficiency, since neutron capture and product detection take place in the same material. 80% efficiency has been realized, and further gains depend soley on progress in material quality [88-90].

In spite of its strong potential, BN is the least investigated among the III-Nitrides semiconductors because the growth of high crystalline quality has proved to be challenging, and this is where NSAG stands to contribute. In addition to our achievements in NSAG of BGaN, we've recently achieved planar hexagonal and cubic BN on a number of substrates, including AlN-buffered Si(111). Figure 69 shows Raman and XRD data on these preliminary results.

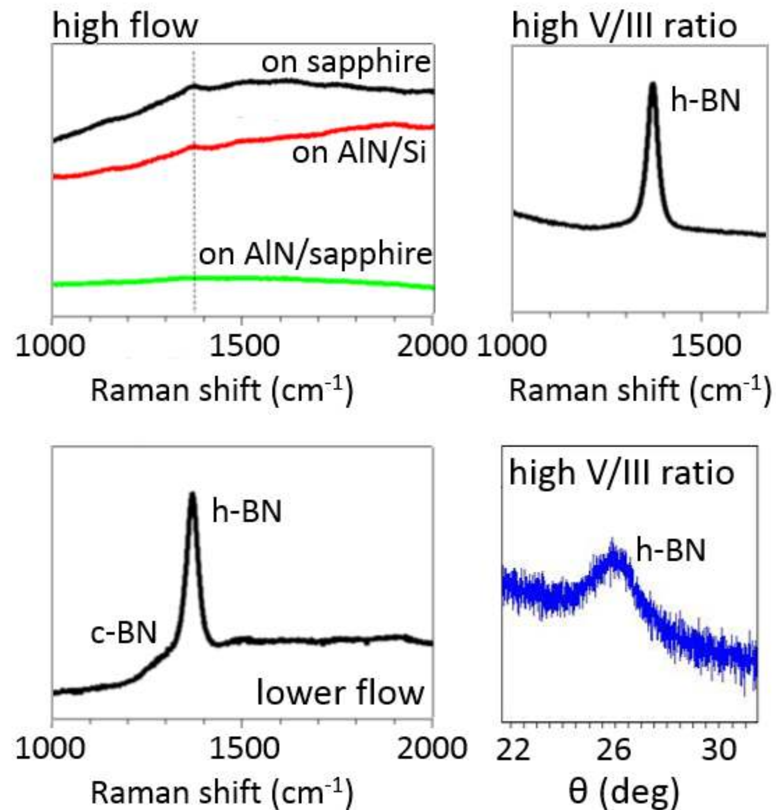

Figure 69. Raman and XRD data of preliminary h- and c-BN growths under a variety of conditions on three different substrates

Figure 70 proposes a BN solid-state neutron detection structure that builds directly on our success achieved with microtemplates (section 4.2.4). By coalescing NSAG BN in exactly the configuration in which we coalesced NSAG GaN, and then placing contacts at the grain boundaries, we create a solid-state neutron detector in which electron-hole pairs created by capture products move through high-quality, dislocation-

free material to reach the contacts. The special placement of the contacts ensures that carriers are never obligated to cross grain boundaries to reach the contacts. Our success using graphene as a back-contact in the previous section could also be directly applied here without much imagination, allowing us to grow thicker BN collection layers without excessively increasing the average distance between electron-hole pair generation and the contacts.

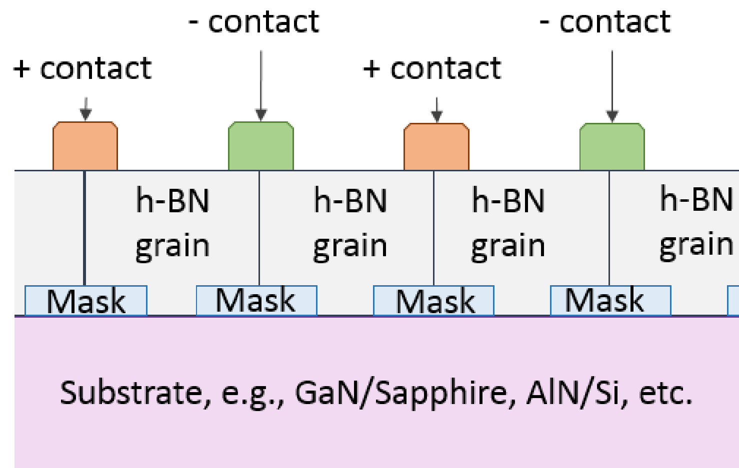

Figure 70. Proposed solid-state neutron detector design based on previous success engineering defect-free BGaN grains. It is essentially our GaN microtemplate (section 4.2.4) with NSAG BN in place of NSAG GaN. The placement of the contacts is critical to ensure carrier paths do not cross grain boundaries. Both conventional and inexpensive substrates will be explored.

5.2.6 Nanoribbon HEMT

A nanoribbon high-electron-mobility transistor (HEMT) is a HEMT wherein the source and drain are connected by nanoribbons (which have been thus far refered to in this document as nanostripes). Using nanoribbons in place of bulk material provides for better heat dissipation geometry and increased gate effectiveness, since the gate wraps around the nanoribbons. Figure 71 illustrates the concept of our proposed device.

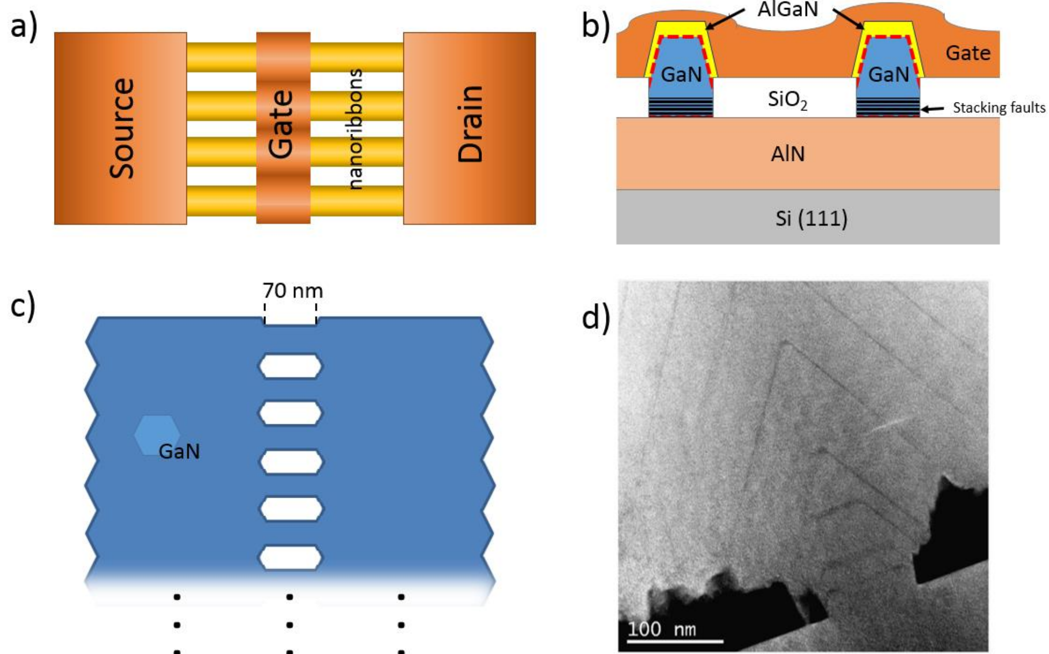

Figure 71. The proposed nanoribbon HEMT device. (a) top view of the proposed device, showing the source and drain contacts connected by nanoribbons that are traversed by a gate contact. The nanoribbons are AlGaN grown on NSAG GaN nanostripes. (b) a cross-section along the gate. The 2DEG channel (red dotted lines) is in the dislocation-free, single-crystal material just below the AlGaN/GaN interface, and the gate wraps around this region, maximizing the coupling between the gate voltage and 2DEG mobility. (c) top view of the shape of NSAG GaN with large contact areas connected by 70 nm-long nanoribbons. A thin AlGaN layer would later be grown on this GaN interface. d) STEM cross-section of AlGaN-demarked GaN nanostripes from section 3.4, proving our capacity to create smooth, faceted AlGaN/GaN interfaces on both triangular and trapezoidal prism-shaped nanoribbons.

The first nanowire HEMT can be credited to Li et al. [95], who self-assembled (and then felled) radial GaN/AlN/AlGaN nanowires. The first useful device of this kind was an array of GaN/InAlN nanoribbons contacted as one HEMT. This device was found to have 46% lower sheet resistance and 20-45% higher current than a planar HEMT simultaneously grown nearby [96]. Additionally, the gate wrapping around the ribbons greatly reduced short-channel effects, as seen earlier in Refs [95, 97]. Unfortunately, the mobility was found to be ***hampered*** by the nanoribbon regime, owing to scattering off the etched surfaces, and the contact resistance was increased by the small access region for the source and drain. The latter problem was addressed to great success in Ref [98]. We

plan to address the former by growing our nanoribbons from the bottom up using NSAG, resulting in smooth termination facets rather than rough etched surfaces.

In addition to solving the surface recombination issue, we plan also to bring this device design to the AlN-buffered Si(111) substrate, vastly reducing cost. However, the nanocolumnar nature of the AlN buffer layer prevents us from achieving arbitrarily long single-crystal nanoribbons. Therefore, we will test multiple aperture lengths to determine the longest single-crystal nanoribbon size possible by our NSAG method. Figure 72a and b show NSAG GaN grown on a mask area whose apertures did not fully develop. We see many single crystals that had space to grow to 300 nm from a single nucleation showing that so long as we have a single nucleation site, we can create large single crystals. The question then becomes how long of an aperture we can use before inviting excessively many multi-nucleation site events. Figure 72c shows a mask pattern to investigate this question. Once we know how long an aperture we can use, the device structure itself will need to be grown through a thick mask to assure that our crystals grow below the mask surface, resulting in an elongated nanoribbon shape.

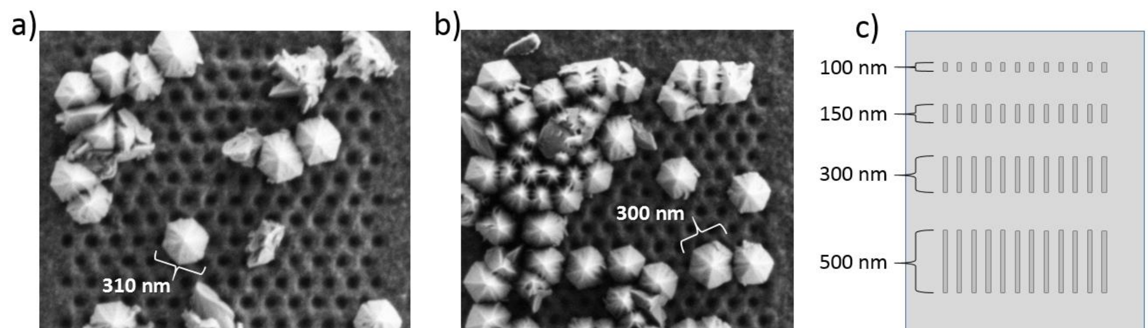

Figure 72. Explanation of the proposed multisize nanoribbon study for AlN/Si(111). a) and b) are SEM images of GaN NSAG on apertured regions where the apertures did not fully develop. They demonstrate that grain-sizes of at least 300 nm are possible for single nucleations. c) is a mask patterned to be used to find the maximum possible single-crystal nanoribbon length. Apertures that are too long will result in multiple nucleation sites (graining) and apertures that are too short will result in a reduced contacting area (contact resistance).

REFERENCES

1. Soltani, A., et al., *High performance TiN gate contact on AlGaN/GaN transistor using a mechanically strain induced P-doping.* Applied Physics Letters, 2014. **104**(23): p. 233506.

2. Yu, L.P., et al., *Study of different type of dislocations in GaN thin films.* Journal of Crystal Growth, 2004. **268**(3–4): p. 484-488.

3. Ruterana, P. and G. Nouet, *Atomic Structure of Extended Defects in Wurtzite GaN Epitaxial Layers.* physica status solidi (b), 2001. **227**(1): p. 177-228.

4. Kato, Y., et al., *Selective growth of wurtzite GaN and AlxGa1−xN on GaN/sapphire substrates by metalorganic vapor phase epitaxy.* Journal of Crystal Growth, 1994. **144**(3–4): p. 133-140.

5. Hiramatsu, K., et al., *Recent progress in selective area growth and epitaxial lateral overgrowth of III-nitrides: effects of reactor pressure in MOVPE growth.* physica status solidi(a), 1999. **176**(1): p. 535-543.

6. Luryi, S. and E. Suhir, *New approach to the high quality epitaxial growth of lattice-mismatched materials.* Applied Physics Letters, 1986. **49**(3): p. 140-142.

7. Sundaram, S., et al., *Nanoscale selective area growth of thick, dense, uniform, In-rich, InGaN nanostructure arrays on GaN/sapphire template.* Journal of Applied Physics, 2014. **116**(16): p. 163105.

8. Mircea, A., A. Ougazzaden, and R. Mellet, *Very uniform epitaxy.* Progress in crystal growth and characterization, 1989. **19**(1): p. 39-49.

9. Sirenko, A.A., et al., *Strain relaxation and surface migration effects in InGaAlAs and InGaAsP selective-area-grown ridge waveguides.* Applied Physics Letters, 2006. **88**(8): p. -.

10. Bonanno, P., et al., *Intrafacet migration effects in InGaN/GaN structures grown on triangular GaN ridges studied by submicron beam x-ray diffraction.* Applied Physics Letters, 2008. **92**(12): p. 123106.

11. Schmidbauer, M., et al., *A novel multi-detection technique for three-dimensional reciprocal-space mapping in grazing-incidence X-ray diffraction.* Journal of Synchrotron Radiation, 2008. **15**(6): p. 549-557.

12. Kukta, R.V. and L.B. Freund, *Minimum energy configuration of epitaxial material clusters on a lattice-mismatched substrate.* Journal of the Mechanics and Physics of Solids, 1997. **45**(11–12): p. 1835-1860.

13. Yago, H., T. Nomura, and K. Ishikawa, *Strain relaxation in GaAs islands on GaP(001).* Applied Surface Science, 1995. **84**(2): p. 119-124.

14. Bonanno, P., et al., *Submicron beam X-ray diffraction of nanoheteroepitaxily grown GaN: Experimental challenges and calibration procedures.* Nuclear Instruments and Methods in Physics Research Section B: Beam Interactions with Materials and Atoms, 2010. **268**(3): p. 320-324.

15. Bragg, W.H. and W.L. Bragg, *The Reflection of X-rays by Crystals*. Vol. 88. 1913. 428-438.

16. Aoki, M., et al., *InGaAs/InGaAsP MQW electroabsorption modulator integrated with a DFB laser fabricated by band-gap energy control selective area MOCVD.* Quantum Electronics, IEEE Journal of, 1993. **29**(6): p. 2088-2096.

17. Gibbon, M., et al., *Selective-area low-pressure MOCVD of GaInAsP and related materials on planar InP substrates.* Semiconductor Science and Technology, 1993. **8**(6): p. 998.

18. Takeuchi, T., H. Amano, and I. Akasaki, *Theoretical study of orientation dependence of piezoelectric effects in wurtzite strained GaInN/GaN heterostructures and quantum wells.* Japanese Journal of Applied Physics, 2000. **39**(2R): p. 413.

19. Feezell, D.F., et al., *Development of Nonpolar and Semipolar InGaN/GaN Visible Light-Emitting Diodes.* MRS Bulletin, 2009. **34**(05): p. 318-323.

20. Shioda, T., et al., *Selective area metal-organic vapor-phase epitaxy of InN, GaN and InGaN covering whole composition range.* Journal of Crystal Growth, 2009. **311**(10): p. 2809-2812.

21. Schuster, M., et al., *Determination of the chemical composition of distorted InGaN/GaN heterostructures from x-ray diffraction data.* Journal of Physics D: Applied Physics, 1999. **32**(10A): p. A56.

22. Goh, W., et al., *Structural and optical properties of nanodots, nanowires, and multi-quantum wells of III-nitride grown by MOVPE nano-selective area growth.* Journal of Crystal Growth, 2011. **315**(1): p. 160-163.

23. Nakamura, S. and G. Fasol, *The Blue Laser Diode: GaN-Based Light Emitting Diode and Lasers*. 1997, Springer, Berlin.

24. Jani, O., et al., *Design and characterization of GaN/ InGaN solar cells.* Applied Physics Letters, 2007. **91**(13): p. 132117.

25. Redaelli, L., et al., *Effect of the quantum well thickness on the performance of InGaN photovoltaic cells.* Applied Physics Letters, 2014. **105**(13): p. 131105.

26. Gmili, Y.E., et al., *Characteristics of the surface microstructures in thick InGaN layers on GaN.* Optical Materials Express, 2013. **3**(8): p. 1111-1118.

27. Bonanno, P., et al., *Nondestructive mapping of chemical composition and structural qualities of group III-nitride nanowires using submicron beam synchrotron-based X-ray diffraction.* Thin Solid Films, 2013.

28. Li, Q. and G.T. Wang, *Spatial Distribution of Defect Luminescence in GaN Nanowires.* Nano Letters, 2010. **10**(5): p. 1554-1558.

29. Rao, M., D. Kim, and S. Mahajan, *Compositional dependence of phase separation in InGaN layers.* Applied physics letters, 2004. **85**: p. 1961.

30. Pereira, S., et al., *Compositional pulling effects in In x Ga 1− x N/G a N layers: A combined depth-resolved cathodoluminescence and Rutherford backscattering/channeling study.* Physical Review B, 2001. **64**(20): p. 205311.

31. Fuhrmann, D., et al., *Optimization scheme for the quantum efficiency of GaInN-based green-light-emitting diodes.* Applied physics letters, 2006. **88**(7): p. 1105.

32. Orsal, G., et al., *Bandgap energy bowing parameter of strained and relaxed InGaN layers.* Optical Materials Express, 2014. **4**(5): p. 1030-1041.

33. El Gmili, Y., et al., *Multilayered InGaN/GaN structure vs. single InGaN layer for solar cell applications: A comparative study.* Acta Materialia, 2013. **61**(17): p. 6587-6596.

34. Sundaram, S., et al., *High quality thick InGaN nanostructures grown by nanoselective area growth for new generation photovoltaic devices.* physica status solidi (a), 2015. **212**(4): p. 740-744.

35. Dong, Y., et al., *Coaxial group III− nitride nanowire photovoltaics.* Nano letters, 2009. **9**(5): p. 2183-2187.

36. Suresh Sundaram, X.L., Youssef El Gmili, Renaud Puybaret, Konstantinos Pantzas, Giles Patriarche, Paul Voss, Jean Paul Salvestrini, and Abdallah Ougazzaden, *MOVPE growth of high quality GaN microtemplates by nanoepitaxial lateral overgrowth.* Proceedings of the 16th European Workshop on MOVPE, Lund, 2015.

37. Dadgar, A., et al., *MOVPE growth of GaN on Si(1 1 1) substrates.* Journal of Crystal Growth, 2003. **248**: p. 556-562.

38. Cao, J., et al., *The influence of the Al pre-deposition on the properties of AlN buffer layer and GaN layer grown on Si (1 1 1) substrate.* Journal of Crystal Growth, 2010. **312**(14): p. 2044-2048.

39. Wei, M., et al., *Effect of AlN buffer thickness on GaN epilayer grown on Si(1 1 1).* Materials Science in Semiconductor Processing, 2011. **14**(2): p. 97-100.

40. Liu, R., et al., *Atomic arrangement at the AlN/Si (111) interface.* Applied Physics Letters, 2003. **83**(5): p. 860-862.

41. Zubia, D., et al., *Nanoheteroepitaxial growth of GaN on Si by organometallic vapor phase epitaxy.* Applied Physics Letters, 2000. **76**(7): p. 858-860.

42. Hersee, S.D., et al., *Nanoheteroepitaxial growth of GaN on Si nanopillar arrays.* Journal of Applied Physics, 2005. **97**(12): p. 124308.

43. Lin, K.-L., et al., *Growth of GaN films on circle array patterned Si (111) substrates.* Journal of Crystal Growth, 2014. **401**: p. 648-651.

44. Gotschke, T., et al., *Influence of the adatom diffusion on selective growth of GaN nanowire regular arrays.* Applied Physics Letters, 2011. **98**(10): p. 103102.

45. Fan, S., et al., *Study on the coalescence of dislocation-free GaN nanowires on Si and SiOx.* Journal of Vacuum Science & Technology B, 2014. **32**(2): p. 02C114.

46. Huang, D., et al., *Defect reduction with quantum dots in GaN grown on sapphire substrates by molecular beam epitaxy.* Applied Physics Letters, 2002. **80**(2): p. 216-218.

47. Ishikawa, H., et al., *Thermal stability of GaN on (111) Si substrate.* Journal of crystal growth, 1998. **189**: p. 178-182.

48. Chen, P., et al., *Growth of high quality GaN layers with AlN buffer on Si(1 1 1) substrates.* Journal of Crystal Growth, 2001. **225**(2–4): p. 150-154.

49. Cuomo, J.J., et al., *Method and apparatus for producing MIIIN columns and MIIIN materials grown thereon*. 2004, Google Patents.

50. Bhuiyan, A.G., et al., *MOVPE growth of InGaN on Si (111) substrates with an intermediate range of In content.* physica status solidi (c), 2012. **9**(3-4): p. 670-672.

51. Gherasoiu, I., et al., *High quality InxGa1–xN thin films with x> 0.2 grown on silicon.* physica status solidi (b), 2010. **247**(7): p. 1747-1749.

52. Yamamoto, A., et al., *A Comparative Study on Metalorganic Vapor Phase Epitaxial InGaN with Intermediate In Compositions Grown on GaN/Sapphire Template and AlN/Si (111) Substrate.* Japanese Journal of Applied Physics, 2013. **52**(8S): p. 08JB19.

53. Yamamoto, A., et al., *Phase separation of thick (~1 μm) InxGa1− xN (x~0.3) grown on AlN/Si (111): Simultaneous emergence of metallic In–Ga and GaN-rich InGaN.* Applied Physics Express, 2014. **7**(3): p. 035502.

54. Sundaram, S., et al., *Nanoselective area growth and characterization of dislocation-free InGaN nanopyramids on AlN buffered Si (111) templates.* Applied Physics Letters, 2015. **107**(11): p. 113105.

55. Ho, I.h. and G. Stringfellow, *Solid phase immiscibility in GaInN.* Applied Physics Letters, 1996. **69**(18): p. 2701-2703.

56. El-Masry, N., et al., *Phase separation in InGaN grown by metalorganic chemical vapor deposition.* Applied physics letters, 1998. **72**(1): p. 40-42.

57. Atsumi, K., et al., *Neutron detection using boron gallium nitride semiconductor material.* APL Materials, 2014. **2**(3): p. 032106.

58. Baghdadli, T., et al., *Electrical and structural characterizations of BGaN thin films grown by metal‐organic vapor‐phase epitaxy.* physica status solidi (c), 2009. **6**(S2): p. S1029-S1032.

59. Ougazzaden, A., et al., *Bandgap bowing in BGaN thin films.* Applied Physics Letters, 2008. **93**(8): p. 83118.

60. Akasaka, T., Y. Kobayashi, and T. Makimoto, *BGaN micro-islands as novel buffers for growth of high-quality GaN on sapphire.* Journal of crystal growth, 2007. **298**: p. 320-324.

61. Gautier, S., et al., *Deep structural analysis of novel BGaN material layers grown by MOVPE.* Journal of Crystal Growth, 2011. **315**(1): p. 288-291.

62. Salvestrini, J., et al. *Tuning of internal gain, dark current and cutoff wavelength of UV photodetectors using quasi-alloy of BGaN-GaN and BGaN-AlN superlattices*. in *SPIE OPTO*. 2012. International Society for Optics and Photonics.

63. Malinauskas, T., et al., *Growth of BGaN epitaxial layers using close‐coupled showerhead MOCVD.* physica status solidi (b), 2015. **252**(5): p. 1138-1141.

64. Giovannetti, G., et al., *Substrate-induced band gap in graphene on hexagonal boron nitride: Ab initio density functional calculations.* Physical Review B, 2007. **76**(7): p. 073103.

65. Dean, C., et al., *Boron nitride substrates for high-quality graphene electronics.* Nature nanotechnology, 2010. **5**(10): p. 722-726.

66. Mayorov, A.S., et al., *Micrometer-scale ballistic transport in encapsulated graphene at room temperature.* Nano letters, 2011. **11**(6): p. 2396-2399.

67. Chung, K., C.-H. Lee, and G.-C. Yi, *Transferable GaN layers grown on ZnO-coated graphene layers for optoelectronic devices.* Science, 2010. **330**(6004): p. 655-657.

68. Kim, J., et al., *Principle of direct van der Waals epitaxy of single-crystalline films on epitaxial graphene.* Nature communications, 2014. **5**.

69. Jo, G., et al., *Large-scale patterned multi-layer graphene films as transparent conducting electrodes for GaN light-emitting diodes.* Nanotechnology, 2010. **21**(17): p. 175201.

70. Jeon, D.-W., et al., *Nanopillar InGaN/GaN light emitting diodes integrated with homogeneous multilayer graphene electrodes.* Journal of Materials Chemistry, 2011. **21**(44): p. 17688-17692.

71. Kim, B.-J., et al., *Large-area transparent conductive few-layer graphene electrode in GaN-based ultra-violet light-emitting diodes.* Applied Physics Letters, 2011. **99**(14): p. 143101.

72. Han, N., et al., *Improved heat dissipation in gallium nitride light-emitting diodes with embedded graphene oxide pattern.* Nature communications, 2013. **4**: p. 1452.

73. Song, J., et al., *Growth, structural and optical properties of ternary InGaN nanorods prepared by selective-area metalorganic chemical vapor deposition.* Nanotechnology, 2014. **25**(22): p. 225602.

74. Kang, J., et al., *Pyramid Array InGaN/GaN Core–Shell Light Emitting Diodes with Homogeneous Multilayer Graphene Electrodes.* Applied Physics Express, 2013. **6**(7): p. 072102.

75. Chang, C.-Y., et al., *Double superstructures in InGaN/GaN nano-pyramid arrays.* Superlattices and Microstructures, 2015. **86**: p. 275-279.

76. Puybaret, R., et al., *Nano selective area growth of GaN by MOVPE on 4H-SiC using epitaxial graphene as a mask: towards integrated III-nitride/graphene/SiC electronics and optoelectronics.* arXiv preprint arXiv:1510.04513, 2015.

77. De Heer, W.A., et al., *Large area and structured epitaxial graphene produced by confinement controlled sublimation of silicon carbide.* Proceedings of the National Academy of Sciences, 2011. **108**(41): p. 16900-16905.

78. Puybaret, R., et al., *Scalable control of graphene growth on 4H-SiC C-face using decomposing silicon nitride masks.* Journal of Physics D: Applied Physics, 2015. **48**(15): p. 152001.

79. Lee, C., et al., *Frictional characteristics of atomically thin sheets.* Science, 2010. **328**(5974): p. 76-80.

80. Zhu, Y., et al., *Field nanoemitters: Ultrathin BN nanosheets protruding from Si3N4 nanowires.* Nano letters, 2006. **6**(12): p. 2982-2986.

81. Jin, C., et al., *Fabrication of a freestanding boron nitride single layer and its defect assignments.* Physical review letters, 2009. **102**(19): p. 195505.

82. Majety, S., et al., *Epitaxial growth and demonstration of hexagonal BN/AlGaN pn junctions for deep ultraviolet photonics.* Applied Physics Letters, 2012. **100**(6): p. 061121.

83. Zhang, X., et al., *Boron nitride nanocarpets: controllable synthesis and their adsorption performance to organic pollutants.* CrystEngComm, 2012. **14**(14): p. 4670-4676.

84. Portehault, D., et al., *High‐surface‐area nanoporous boron carbon nitrides for hydrogen storage.* Advanced Functional Materials, 2010. **20**(11): p. 1827-1833.

85. Vinu, A., et al., *Synthesis of mesoporous BN and BCN exhibiting large surface areas via templating methods.* Chemistry of materials, 2005. **17**(24): p. 5887-5890.

86. Dibandjo, P., et al., *Synthesis of boron nitride with ordered mesostructure.* Advanced Materials, 2005. **17**(5): p. 571-574.

87. Doty, F.P., *Boron nitride solid state neutron detector*. 2004, Google Patents.

88. Li, J., et al., *Hexagonal boron nitride epitaxial layers as neutron detector materials.* Nuclear Instruments and Methods in Physics Research Section A: Accelerators, Spectrometers, Detectors and Associated Equipment, 2011. **654**(1): p. 417-420.

89. Doan, T., et al., *Hexagonal boron nitride thin film thermal neutron detectors with high energy resolution of the reaction products.* Nuclear Instruments and Methods in Physics Research Section A: Accelerators, Spectrometers, Detectors and Associated Equipment, 2015. **783**: p. 121-127.

90. Doan, T.C., et al., *Fabrication and characterization of solid-state thermal neutron detectors based on hexagonal boron nitride epilayers.* Nuclear Instruments and Methods in Physics Research Section A: Accelerators, Spectrometers, Detectors and Associated Equipment, 2014. **748**: p. 84-90.

91. Höglund, C., et al., *B4C thin films for neutron detection.* Journal of Applied Physics, 2012. **111**(10): p. 104908.

92. Lousa, A., et al., *Effect of ion bombardment on the properties of B 4 C thin films deposited by RF sputtering.* Thin Solid Films, 1999. **355**: p. 210-213.

93. McGregor, D.S., et al., *Design considerations for thin film coated semiconductor thermal neutron detectors—I: basics regarding alpha particle emitting neutron reactive films.* Nuclear Instruments and Methods in Physics Research Section A: Accelerators, Spectrometers, Detectors and Associated Equipment, 2003. **500**(1): p. 272-308.

94. Nikolić, R.J., et al. *Fabrication of Pillar-structured thermal neutron detectors*. in *Nuclear Science Symposium Conference Record, 2007. NSS'07. IEEE*. 2007. IEEE.

95. Li, Y., et al., *Dopant-Free GaN/AlN/AlGaN Radial Nanowire Heterostructures as High Electron Mobility Transistors.* Nano Letters, 2006. **7**(6): p. 1468-1473.

96. Azize, M., et al., *High-electron-mobility transistors based on InAlN/GaN nanoribbons.* Electron Device Letters, IEEE, 2011. **32**(12): p. 1680-1682.

97. Lu, W., P. Xie, and C.M. Lieber, *Nanowire transistor performance limits and applications.* Electron Devices, IEEE Transactions on, 2008. **55**(11): p. 2859-2876.

98. Lee, D.S., et al., *Nanowire Channel InAlN/GaN HEMTs With High Linearity of and.* Electron Device Letters, IEEE, 2013. **34**(8): p. 969-971.